UNIVERSITY OF BIRMINGHAM

BAUSCHINGER EFFECT IN MACRO AND MICRO SIZED HIGH STRENGTH LOW ALLOY PIPELINE STEELS

THIAGO SOARES PEREIRA

A thesis submitted to the University of Birmingham

for the degree of

DOCTOR OF PHILOSOPHY

School of Metallurgy and Materials

University of Birmingham

August 2015

ABSTRACT

An experimental investigation on the Bauschinger effect of an X70, X80 and X100 high strength low alloy pipeline steels is presented. The microstructure of the as-received alloys was characterized in terms of the different phases present, grain size, occurring precipitation and dislocation structure. A variety of microstructures was present across the different alloys, ranging from a refined granular ferrite with small amounts of perlite to a bainitic structure containing martensite/austenite islands, retained austenite and small cementite constituents along with a small amount of (Ti,Nb) carbides and Nb carbides. Similarly, the dislocation structures varied from homogeneously distributed across the ferrite grains to clusters/walls of dislocations.

Mechanical tests were carried out to analyse the Bauschinger effect on the studied alloys on macro and micro sized samples up to 1% and 2% plastic strain. A micro-device for Bauschinger test was designed and manufactured using micro-electro-mechanical-system (MEMS) technology and was incorporated onto a FIB/SEM in order to prepare the micro sized samples and perform the micro Bauschinger tests.

The Bauschinger stress parameter showed that the Bauschinger effect becomes more obvious in samples with higher yield strength and also with increasing pre-strain. In addition, the Bauschinger effect remained similar on the samples of different sizes in the current study. The results indicate that the cause of the early yielding during reverse loading of these alloys is dominated by the dislocation-dislocation interaction.

ACKNOWLEDGMENTS

Firstly, I would like to thank Dr. Yu Lung Chiu and Professor Ian Jones for their immense support during the time of this research, as well as for the invaluable knowledge shared. Without their guidance and encouragement, this project would not be possible so, for that, I thank you.

I would also like to thank the University of Birmingham and the School of Metallurgy and Materials for the provision of all the necessary tools, laboratories, equipments and the facilities available to us. Additionally, I would like to thank the School of Mechanical Engineering for providing their support with an important part of this project.

Thank you to the Roberto Rocca Fellowship Programme for providing the encouragement and financial support for this project.

Thank you to my colleagues in the microscopy research group, you all have a special place in my heart, for the time we spent together, working hard and supporting each other. Finishing this project would be much harder without the presence of each and every one of you.

Also, thank you to my good friends back at home, even though we spent all this time apart, I would like you to know you all have helped me get here, and I thank you for that.

Very special thanks to my family, my parents, my brother and sister. You have been an indispensable part of my life and I would not be here today without your great support and encouragement. Thanks to my second family, my wife´s parents, who have also provided great support.

Finally, the biggest thank you possible to my wife, who has shared this experience with me, gone through the highs and lows with me, and person whose presence made this much more special.

TABLE OF CONTENTS

1. INTRODUCTION 1

2. HIGH STRENGTH LOW ALLOY STEELS 5

2.1 The role of Ti, Nb and V in HSLA pipeline steels 5

2.2 Thermomechanical processing of microalloyed steels 10

2.3 Deformation mechanisms 15

2.3.1 Slip bands 15

2.3.2 The Burgers vector 17

2.4 Strengthening mechanisms 17

2.4.1 Grain size strengthening 17

2.4.2 Solid solution strengthening 20

2.4.3 Work hardening 21

2.4.4 Second phase strengthening 21

2.4.5 Precipitate strengthening 23

3 THE UOE PIPE MAKING PROCESS AND THE BAUSCHINGER EFFECT 25

3.1 The UOE process 25

3.2 The Bauschinger effect 30

4 MICRO BAUSCHINGER TESTS 38

4.1 Sample size and the Bauschinger effect 38

4.2 Microelectromechanical systems (MEMS) 40

4.3 Straining MEMS device idea 42

4.4 Straining MEMS device development 45

5 MATERIALS AND EXPERIMENTAL TECHNIQUES 58

5.1 Materials 58

5.2 Thermodynamic modelling 59

5.3 Scanning electron microscopy (SEM) 59

5.4 Transmission electron microscopy (TEM) 60

5.5 Focused Ion-Beam (FIB) 63

5.6 Mechanical tests 63

5.7 Micro Bauschinger tests 64

6 RESULTS 67

6.1 X70 alloy 67

6.1.1 Thermodynamic simulation 67

6.1.2 Microstructure of X70 as-received 68

6.1.3 Compression tests 77

6.1.4 Macro Bauschinger tests 80

6.1.5 In-situ Bauschinger tests 84

6.2 X80 alloy 88

6.2.1 Thermodynamic simulation 88

6.2.2 Microstructure of X80 as-received 89

6.2.3 Compression tests 94

6.2.4 Macro Bauschinger tests 96

6.2.5 In-situ Bauschinger tests 98

6.3 X100 alloy 102

6.3.1 Thermodynamic simulation 102

6.3.2 Microstructure of X100 as-received 103

6.3.3 Compression tests 106

6.3.4 Macro Bauschinger tests 108

6.3.5 In-situ tests 111

7 DISCUSSION 114

7.1 Summary of results 114

7.2 As-received microstructure 120

7.3 Mechanical properties 125

7.4 Bauschinger tests 127

8 CONCLUSION AND FUTURE WORK 138

8.1 Conclusions 138

8.2 Proposed future work 140

LIST OF REFERENCES 141

1. INTRODUCTION

High strength low alloys (HSLA) steels are the chosen material for pipeline applications used in the transportation of oil and gas, due to their good mechanical properties combination, relative corrosion resistance, improved weldability and low production costs.

The pursuit of lower operational costs and increase of the transportation efficiency has pushed the demand for higher working pressures leading to increasing the strength requirements of the alloys and therefore pushing the development of higher strength grades [1]. Figure 1.01 illustrates the increase in the working pressure for gas transportation in the past decades.

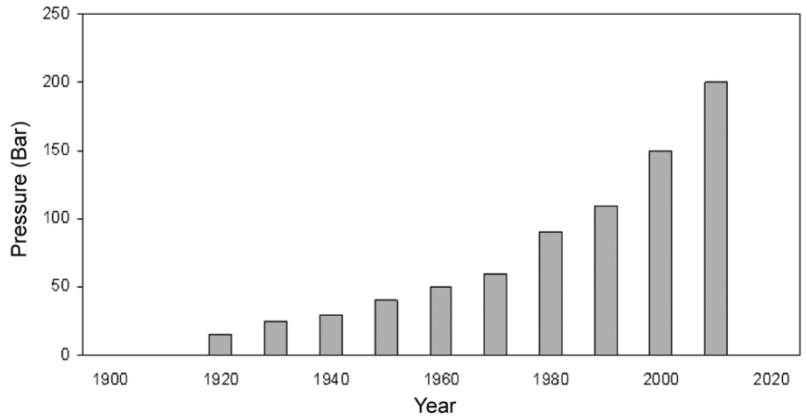

Figure 1.01 – Graph showing the increase in the working pressure for gas transportation over the years. [2]

Early alloy developments have generated yield strengths of around 290 to 350 MPa for the X42 and X52 alloys and further progressively improved to the X120 alloy currently been developed with 830 MPa yield strength, as shown in figure 1.02.

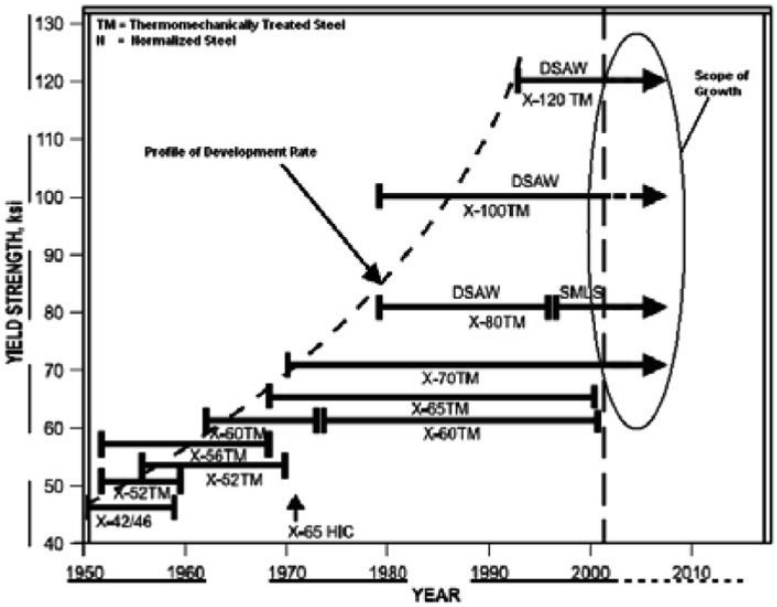

Figure 1.02 – Strength grade development of high strength low alloys. [3]

The UOE process is used for making the large diameter welded pipes for oil and gas transportation. This process consists of different steps of cold deformation which cause the material to go through cycles of compression and tension. Moreover, it has been reported that work softening can occur during the cyclic plastic deformation, where the material may present an early yielding when strained in the opposite direction, following a strain in the forward direction – the phenomenon called Bauschinger effect.

It is important, therefore, to understand the causes of the Bauschinger effect with the long term aim to decrease or even avoid the work softening of the HSLA steels that may occur during the UOE process.

The present research project is aimed at understanding the Bauschinger effect on three HSLA steels X70, X80 and X100 alloys and focuses on the analysis of the microstructures and their effect on the Bauschinger effect; characterising the

microstructure of the alloys in terms of grain size, present second phases, precipitates, dislocation density and structures as well as thermodynamic modelling; analysing the mechanical properties of the alloys, based on the compression and Bauschinger tests; additionally, developing a microeletromechanical device in order to analyse the operating Bauschinger mechanism in micro scaled samples.

The scope of the research and its results are laid out as follows:

Chapter 2 consists of a review of the high strength low alloys steels, the influence of the chemical composition present, the applied thermomechanical processing, and the strengthening and deformation mechanisms within these alloys.

Chapter 3 presents an overview of the UOE pipe making process, the different steps during the process, the induced strain caused by it as well as its relation to the Bauschinger effect. In addition, the theory of the Bauschinger effect and the parameters used to quantify the effect is explained.

The effect of sample size on the Bauschinger effect is presented in Chapter 4, along with the development of a micro mechanical testing device using microelectromechanical systems (MEMS) technology.

Chapter 5 introduces the different HSLA steels studied as well as the experimental procedure used during this research project.

The results obtained in this study are shown in Chapter 6.

Discussion of the results is presented in Chapter 7.

Finally, Chapter 8 presents the concluding remarks drawn from this research along with the suggestion for future work.

2. HIGH STRENGTH LOW ALLOY STEELS

2.1 The role of Ti, Nb and V in HSLA pipeline steels

It is well known that, amongst the alloying elements, carbon content is the most cost effective to modify the mechanical properties of steel via its effects on the balance of the soft ferrite and the stronger constituents: Pearlite, Bainite and Martensite, on the final steel product in order to achieve a higher yield strength, for instance. This strengthening mechanism, however, results in a loss of ductility and toughness [4, 5], which means that seeking the right balance of the mechanical properties of a plain carbon steel alloy requires compromises.

Another important factor in choosing the right amount of carbon in pipeline steels is the weldability. The local heating and subsequent cooling associated with the welding can introduce residual stresses and cause a large microstructure change in the Heat Affected Zones (HAZ) of higher carbon steels, which can also increase stress corrosion cracking (SCC) [6, 7] of the material.

For these reasons, modern pipeline steels have been traditionally developed to have a low carbon content. To counteract the loss of strength compared with the usual steel microstructures, their strengthening is based on grain refinement and precipitate strengthening issuing from small additions of titanium, niobium and vanadium, combined with a subsequent thermomechanically controlled rolling process. Compared to unalloyed structural steels, high strength low alloys steels present a

better balance of yield strength, ductility and toughness, giving them a wide range of applications in the automobiles industry, in structures such as bridges and cranes and, among others, the oil and gas extraction industry [8].

To understand the effects of titanium, niobium and vanadium on the microstructure, it is necessary to understand their solubility, precipitation and their retardation of austenitic recrystallization.

At different temperatures, alloying elements have different solubilities in the material, as shown in figure 2.01, where it can be noticed that TiN is the most stable compound and VC the most soluble in Fe. This difference in solubility can be exploited during rolling, using the precipitation at different stages and temperatures in the process to achieve the desired microstructure and, therefore, mechanical properties of the material.

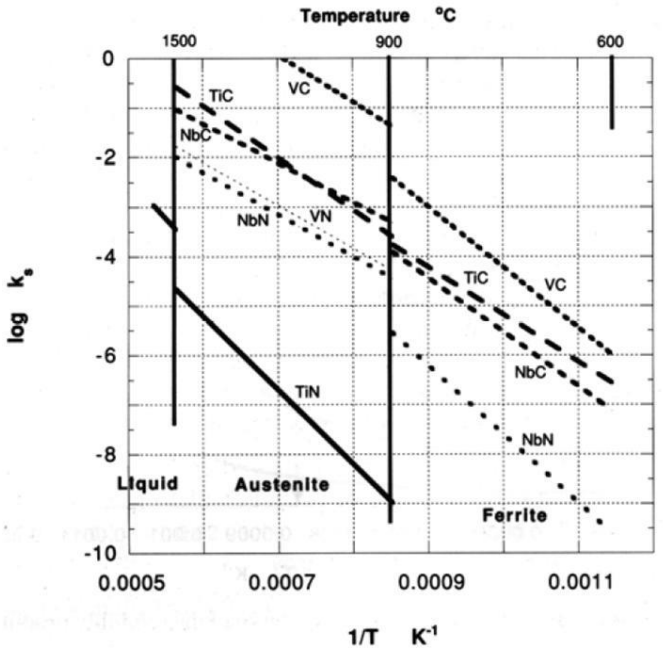

Figure 2.01 – Solubility of Ti, V and Niobium in Fe according to temperature. ks is the solubility product and its temperature dependence is given by log ks = A-B/T, where A and B are constants for a given system [9].

As the temperature falls, the undissolved or recently formed carbides and nitrides which precipitate at higher temperature will contribute to refinement of the initial austenite structure (γ phase) by pinning the austenitic grain boundaries and inhibiting grain growth [10], which will play a major part in obtaining a fine grain size in the ferrite with a related strengthening effect. However, due to the high temperatures, these precipitates may suffer rapid coarsening, resulting in a low contribution to precipitate strengthening. In the austenite/ferrite transition, these precipitates formed above the eutectoid temperature can influence the transformation kinetics and the morphology of the ferritic product.

Titanium rich particles in HSLA steels are reported to be as large as 3-5 μm in diameter and can be detrimental to the toughness of the steel [11, 12]. They can precipitate in spherical or cubic shapes and it has been reported that Ti (C, N) which are formed in higher temperature can also deplete the matrix of niobium and vanadium carbides and nitrides due to the formation of coarse Ti-Nb (C, N) complexes, causing a reduction in the amount of small strengthening precipitates and resulting in a loss of yield strength [13].

On the other hand, precipitates with higher solubility will stay in solution to lower temperatures and will then precipitate in the ferrite. Therefore, these precipitates are smaller and, instead of pinning austenitic grain boundaries, they will contribute to precipitate strengthening in the ferrite, pinning dislocations. Precipitate strengthening can also be enhanced by thermomechanical processing, as the increased number of dislocations act as nucleation sites for particles to precipitate [9].

Niobium rich particles are in general 20 to 100 nm in diameter and, although they can be formed at austenitic temperatures, they mostly precipitate in the ferrite aiding precipitate strengthening [9].

Vanadium rich particles are even smaller than Nb (C, N), often ranging from 2 to 30 nm in diameter. Particles of this size are optimum for precipitate strengthening and can increase the yield strength of a steel under certain conditions [14]. They also present a characteristic orientation relationship with the matrix called Baker–Nutting [15], as follows:

$$(001)_{Vc} \quad || \quad (001)_{\alpha Fe}$$

$$[010]_{Vc} \quad || \quad [110]_{\alpha Fe}$$

In some HSLA steels, a very important type of precipitation takes place during the γ-α transformation, which results in sheets of finely distributed particles, as shown in figure 2.02. Its mechanism of formation is suggested to be related to the ledge growth of ferrite, where new layers of ferrite sweep over the previous layer, providing nucleation sites at the ferrite/austenite interface until the next layer of ferrite is transformed [14 - 17]. This effect is optimized by the large drop in solubility of the alloying elements between austenite and ferrite, and evidence of interphase precipitation involving all three elements, vanadium, niobium and titanium [15-23], has been presented.

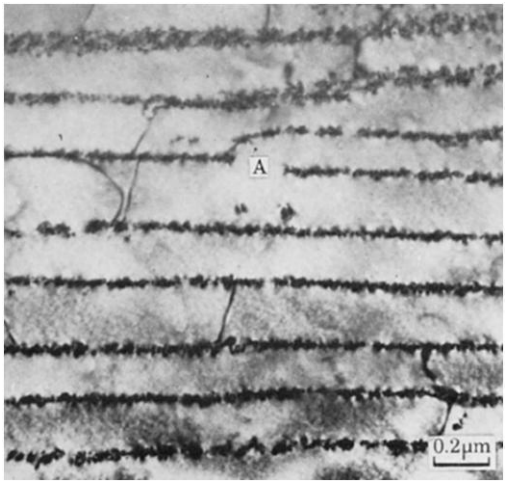

Figure 2.02 – TEM micrograph of a steel sample showing parallel sheets of particles. [19]

In this type of interphase precipitation, the spacing between the rows of precipitates and the particle size both increase with a decrease in the rate of transformation, as the ledges of ferrite take longer to grow, resulting in larger ledges and allowing more time for the diffusion of the alloying elements to occur. In general, precipitates formed via this mechanism are 3 to 10 nm in diameter, while the spacing between particles is 5 to 30 nm, thus resulting in a large strength improvement. Research on the effects of cooling rate and temperature of transformation show that an increase of the yield strength of 100% is achievable [9].

Addition of Nb, Ti and V can also retard austenite recrystallization [24, 25, 26], although the effects of niobium and titanium are much greater than that of vanadium. Figure 2.03 shows the effect of Nb and Ti on the softening ratio of specimens held at different temperatures. The softening effect is due to the recrystallization of the austenitic grains.

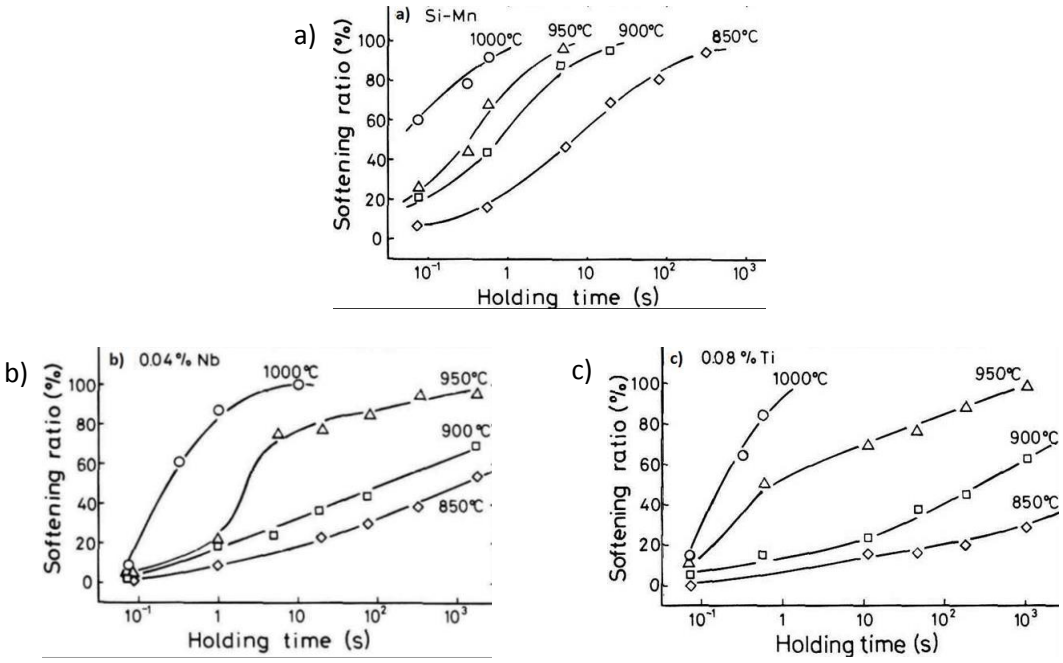

Figure 2.03 – Effect of Nb and Ti on the retardation of austenitic recrystallization: a) Silicon-manganese steel; b) 0.04% Nb steel; c) 0.08% Ti steel [9].

Also, addition of elements such as manganese, molybdenum, copper and nickel can improve the strength of the material via the pinning of dislocations by different sizes of elements in solid solution in the matrix lattice. These elements also contribute to the formation of different phases such as pearlite, bainite and martensite, which are much stronger than ferrite. The strengthening in the latter case depends on the volume fraction of the phases present [9].

2.2 Thermomechanical processing of microalloyed steels

The development of HSLA steels is very much tied up with the development of appropriate steel processing techniques. The strengthening of steel alloys by addition

of Ti, Nb and V can only achieve its full potential by making use of a carefully planned thermomechanical scheme. Generally, in the case of large diameter pipeline steels, rolled plates are used; more specifically Thermomechanically Controlled Rolling (TMCR) is applied.

TMCR generally consists of a steel alloy being heated above the austenite-ferrite transformation temperature, rolled at different temperatures during cooling and cooled at specific rates in order to achieve a desired final product. Figure 2.04 illustrates various processing schedules that may be used during TMCR.

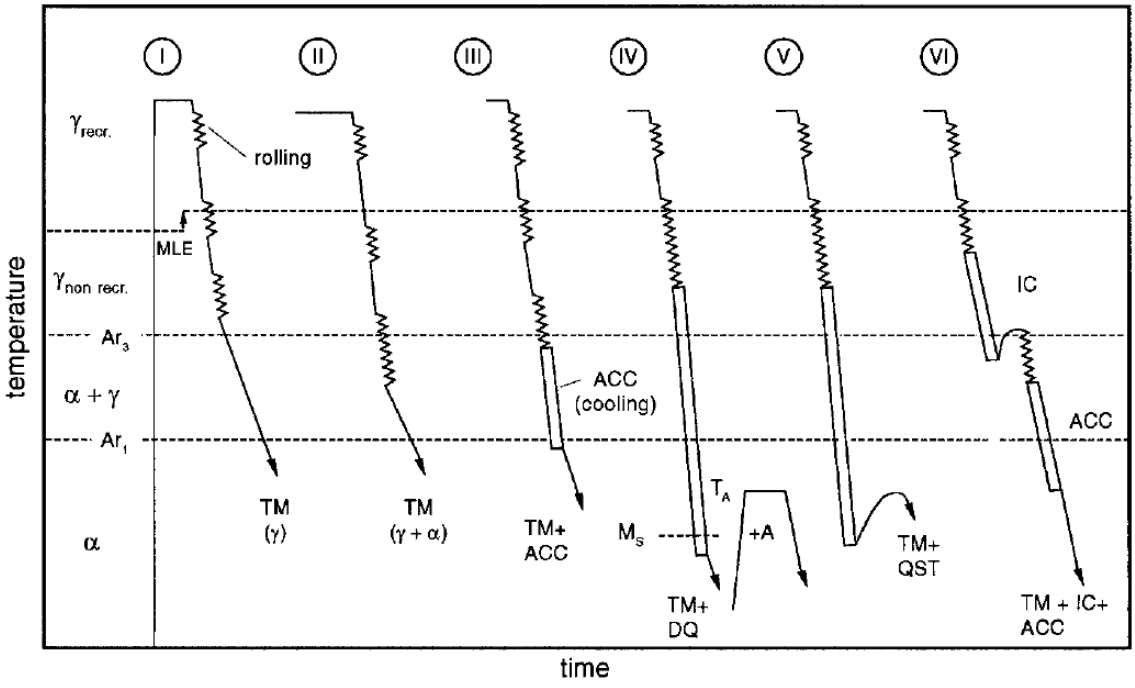

Figure 2.04 – Temperature – time diagrams for different thermomechanically controlled rolling schedules. TM – thermomechanical treatment, ACC – accelerated cooling, DQ – direct quenching, QST – quenching and self-tempering, IC – intermediate cooling. [27]

During the thermomechanically controlled rolling, various parameters such as the initial temperature, rolling temperature, strain and strain rate, as well as the finishing rolling temperature and cooling rate may influence the microstructure of the processed alloy and, therefore, its mechanical properties [28, 29].

The initial temperature of the TMCR will determine the amount and type of precipitates present before rolling, as well as the alloying elements that will be in solid solution, as mentioned in Section 2.1. It is also important to control the amount of time this temperature is held, as coarsening of the austenitic grains and the precipitates will damage the strength of the material.

Rolling can be carried out at different temperatures and there are typically two or three rolling processes during a TMCR route. Rolling at austenitic temperatures will decrease the austenite grain size, resulting in a finer ferritic microstructure after γ-α transformation. As mentioned in Section 2.1, alloying elements will influence the recrystallization kinetics of the austenitic grains, maintaining the material in an unrecrystallized or partially recrystallized state and providing mechanical refinement of the structure. Decreasing the rolling temperature into the ferrite region will further refine the structure formed, forming textured subgrains and resulting in improved mechanical properties. Figure 2.05 illustrates the change in grain size with rolling temperature during the TMCR.

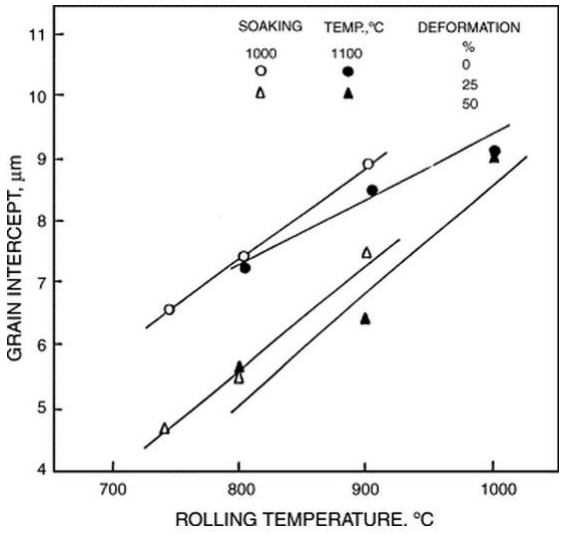

Figure 2.05 – The influence of the rolling temperature on grain size. [30]

The strain and the strain rate during rolling may influence the precipitate strengthening of the alloy. The higher dislocation density at high strain levels will provide more nucleation sites inducing more alloying precipitation. On the other hand, this may also deplete the alloy of its alloying elements, reducing the amount available for subsequent precipitation.

Increasing the cooling rate during TMCR may modify the structure of the final product by decreasing the ferritic grain size or influencing the transformation of the remaining austenitic structure, resulting in an increase in the amount of pearlitie or bainitie. A higher cooling rate therefore generally results in an increase in the yield strength of the material. However, due to the addition of the stronger pearlite or bainite, there is a reduction in toughness and ductility of the material, as shown in figures 2.06 and 2.07. In addition, if a very low finish rolling temperature is applied, the cooling rate

effects may become unavailable, as the remaining temperature range down to room temperature is too small.

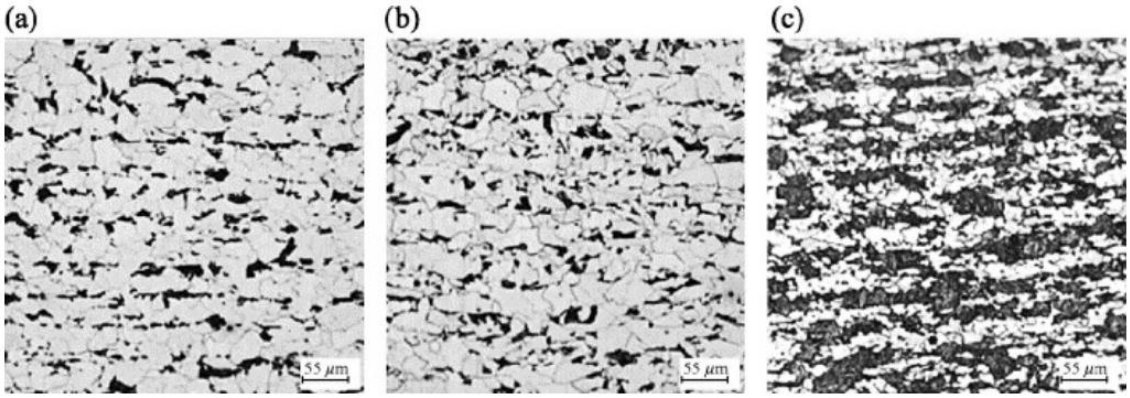

Figure 2.06 – Optical micrographs showing the effect of different cooling rates on the microstructure of a steel. a) 5 °C/s, b) 10 °C/s and c) 20 °C/s. [29]

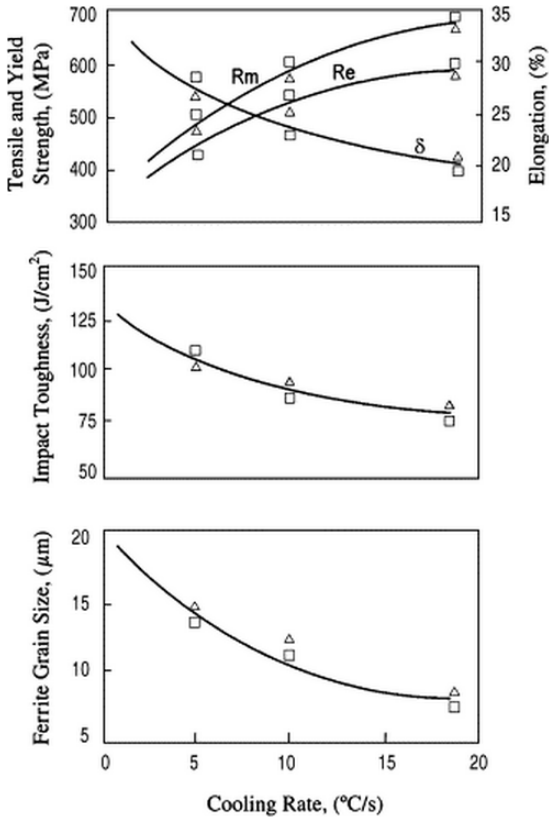

Figure 2.07 - Diagram showing the effects of cooling rate on the mechanical properties of a steel plate after TMCR. [29]

It is noticeable from Sections 2.1 and 2.2 that the relationship between chemical composition and the processing of the alloy can result in a vast effect on the microstructure and, therefore, the mechanical properties of the material. The lower carbon content required by pipeline applications has resulted in the pursuit of a different strengthening mechanism within the steel alloys. Combining small additions of specific alloying elements with tailored thermomechanical processing has been the key to HSLA development.

2.3 Deformation mechanisms

2.3.1 Slip bands

Plastic deformation in many crystals is accomplished by translational slip, where part of a crystal slides across a neighbouring part, creating a line of intersection of a slip surface with the outer surface of a crystal, called a slip band. Figure 2.08 shows the relationship between the slip plane, slip direction and the tension direction for a cylindrical crystal.

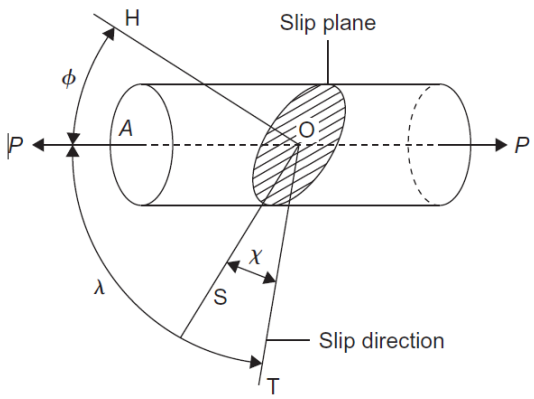

Figure 2.08 – Diagram showing the slip plane, slip direction and the axis of tension of a cylindrical crystal. [31]

The directions and planes of slip depend on the crystal structure of the material. For a particular crystal structure, the slip plane is the one with the most dense atomic packing and the slip direction in the plane is the one that is most closely packed with atoms.

In a FCC crystal structure, the {111} planes are closely packed, as demonstrated in figure 2.09. Slip occurs along the <110> directions. In a BCC crystal structure, the most closely packed planes are the {110} family in the <111> directions, as shown in figure 2.10. The [111] direction, however, is also shared between the {211} and the {321} family of planes [32].

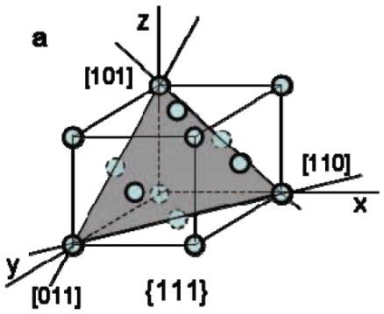

Figure 2.09 – The FCC crystal structure illustrating the {111} family of slip planes and the <110> slip directions. [33]

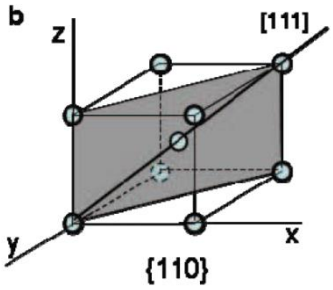

Figure 2.10 – The BCC crystal structure illustrating the {110} family of slip planes and the <111> directions. [33]

2.3.2 The Burgers vector

The vector which describes the direction and distance of movement of relative atoms is called the Burgers vector. It determines the nature of a dislocation. Its magnitude is equal to the interatomic separation in its direction and thus it is convenient to specify a Burgers vector in terms of unit cell edge length (a) along with its crystallographic direction indices [32], as follows:

$$\boldsymbol{b}(BCC) = \frac{a}{2} < 111 >$$

2.4 Strengthening mechanisms

Plastic deformation depends on the ability of dislocations to move. Therefore, enhancement of the mechanical properties can be achieved by reducing the mobility of the dislocations. The main strengthening mechanisms in steel are grain size reduction, solid-solution, strain hardening, second phase and precipitate strengthening.

2.4.1 Grain size strengthening

The dependence of the yield strength on grain size is expressed by the Hall-Petch equation [9]:

$$\sigma_y = \sigma_i + k_y d^{\frac{-1}{2}}$$

where σ_y is the yield stress, σ_i is the friction stress, k_y is the strengthening coefficient and d is the grain size.

Figure 2.11 illustrates effect of the grain size on the yield strength of a mild steel.

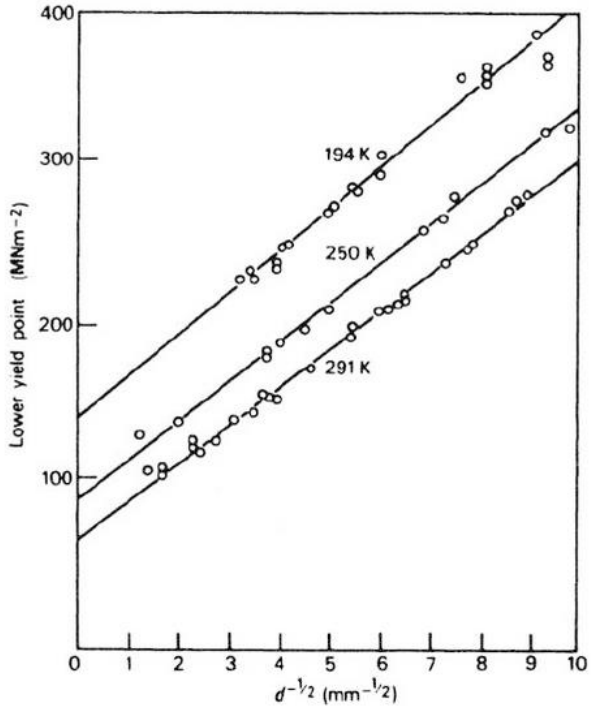

Figure 2.11 – The dependence of the stress of a mild steel on the grain size. [34]

Grain boundaries are the interface between two neighbouring grains which have different crystallographic orientations. They act as a barrier to dislocations during plastic deformation because of the discontinuity of the slip plane in which a dislocation was moving, preventing it from moving further. A pile-up of dislocations will then occur, as illustrated in figure 2.12, increasing the stress at the head of the pile-up until it reaches a critical value, when it will induce slip in the neighbouring grain.

The maximum shear stress [32] is given by

$$\tau_{max} = (\tau - \tau_i)\left(\frac{d}{4r}\right)^{\frac{1}{2}}$$

where τ is a shear stress applied to a polycrystal, τ_i is the friction shear stress, d is the grain size and r is the distance from the head of the slip band to a dislocation source in the neighbouring grain. $(\tau - \tau_i)$ represents the grain boundary resistance and the stress concentration at the source of dislocations in the neighbouring grain is proportional to $\left(\frac{d}{4r}\right)^{\frac{1}{2}}$.

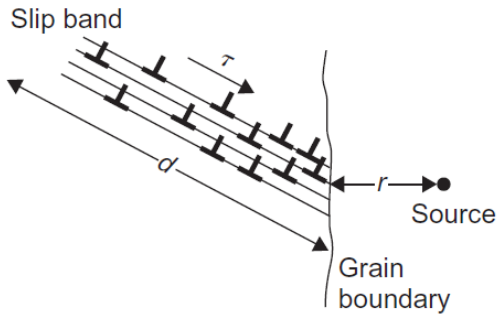

Figure 2.12 – Diagram illustrating dislocation pile-up at a grain boundary. [32]

Larger grains will allow longer pile-ups and, therefore, higher stresses at the head of the pile-up so the deformation can propagate easier to the next grain [9].

Of all strengthening mechanisms, grain size reduction is the only one that increases the strength and toughness of the material at the same time.

2.4.2 Solid solution strengthening

Alloying elements that go into solid solution have a different size from the matrix average and therefore cause lattice distortion, creating a stress field around the atom, which interacts with dislocations, preventing them from moving. An atom that is smaller than the atom from the matrix will cause tensile strain on the crystal, while a bigger atom will cause compressive strain [35]. However, because the solubility of some atoms is low at low temperatures, strengthening through solid solution is limited and usually combined with other mechanisms [9].

Figure 2.13 shows the increase in yield stress from elements in solid solution, where significant improvements are noticeable. However, addition of such elements can have an unfavourable effect on the strengthening if not in solid solution, caused by the TMCR process.

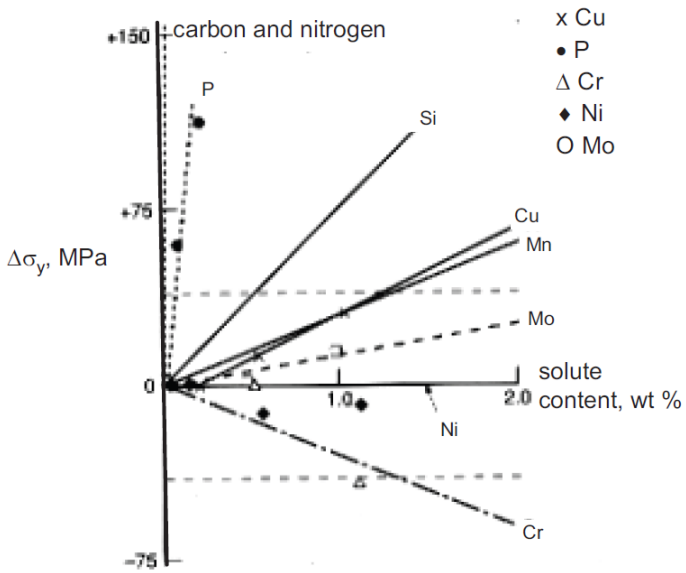

Figure 2.13 – The effect of various solute contents on the yield strength of Fe. [9]

2.4.3 Work hardening

As dislocation density increases with deformation, the frequency of dislocation-dislocation interactions also increases, creating obstacles to their movement. Which means that, during plastic deformation, the number of dislocations is increasing and, therefore, the number of mobile dislocations is decreasing. The result is an increase in the stress necessary to continue the deformation [9].

The strengthening dependence on dislocation (σ_d) density is often calculated using the Taylor equation as follows [36].

$$\sigma_d = A_T G b \sqrt{\rho}$$

where A_T is a constant, G is the shear modulus, b is the Burgers vector and ρ is the dislocation density.

2.4.4 Second phase strengthening

Different phases within the matrix can influence the strength of the material. Iron-carbon alloys may contain different phases, depending on their chemical composition, strain and heat treatment. Ferrite is the most common phase, soft and ductile and usually considered as the matrix. Second phases can be pearlite, bainite, spheroidite and martensite, and they are all harder and more brittle than ferrite [9]. The strengthening effect will depend on the volume fraction of the phase present in the

material, as will the loss in toughness. In addition to the higher strength of the phase, boundaries between phases also contribute to the strengthening of the material, resulting in dislocation pile ups.

Increasing carbon content in plain C-Mn steel will lead to an increase in its strength due to the resultant increase in the amount of pearlite [37], as illustrated in figure 2.14. As a harder phase than ferrite, the increase in pearlite results in increasing the flow stress of the steel during plastic deformation, as shown in figure 2.15. However, elastic deformation is not affected as much, and so is the yield strength [38], as illustrated in figure 2.16. Similarly, an increase in Mn content increases the amount of pearlite present in the steel due to its effect in reducing the eutectoid composition. As a result, it also increases the strength of the material due to the increase in pearlite as well as its contribution to the solid solution strengthening.

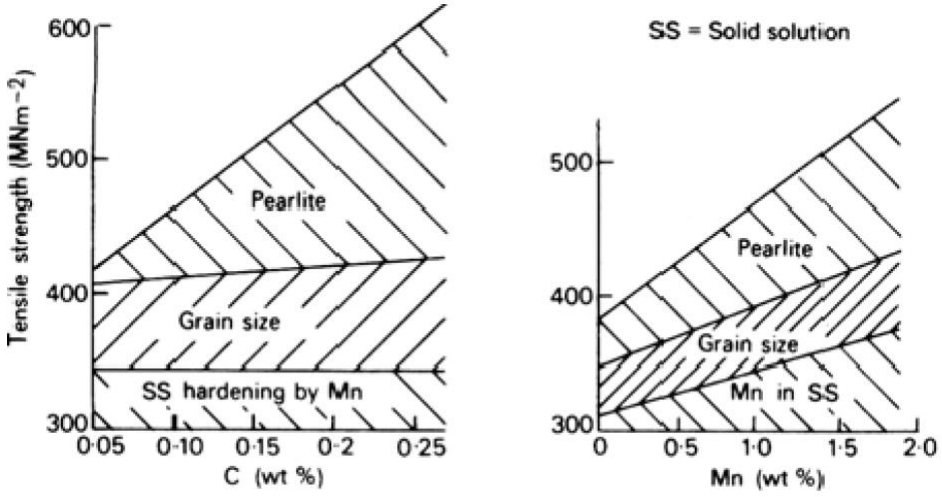

Figure 2.14 – Diagram comparing C and Mn content on the strengthening of a steel. [37]

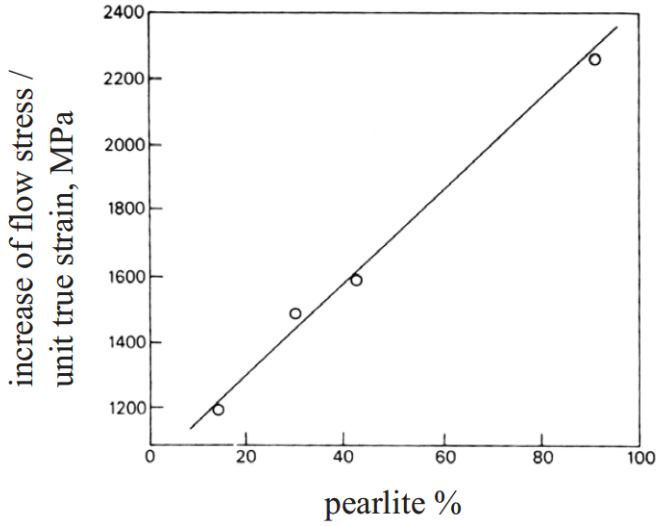

Figure 2.15 – Effect of the amount of pearlite on the work hardening of a steel alloy. [38]

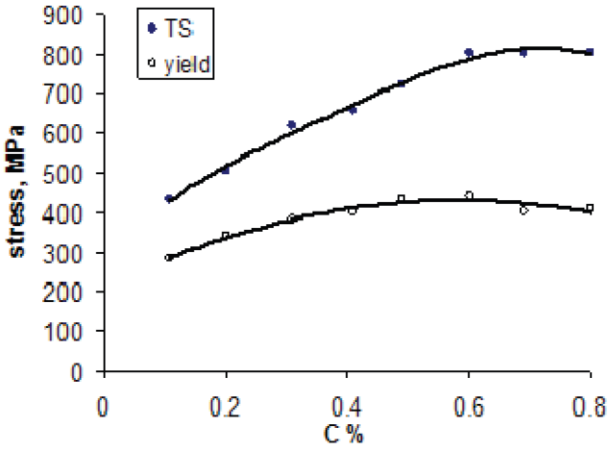

Figure 2.16 – Effect of the amount of carbon on the strengthening of a steel alloy. [38]

2.4.5 Precipitate strengthening

Strengthening by precipitation is possible due to the interaction of mobile dislocations with fine and homogeneously distributed precipitates. Therefore, it depends on the Burgers vector of the dislocation interacting with precipitates and the size and volume fraction of these precipitates, and is described by the Orowan equation for a regular array of particles [9]:

$$\Delta\tau_y = \frac{Gb}{L}$$

where G is the shear modulus, b is the Burgers vector and L is related to the volume fraction and size of the particles.

If a random array of particles is assumed, the Ashby-Orowan relationship is used:

$$\Delta\sigma_{y} = \frac{10.8\sqrt{f}}{X}\ln\left(\frac{X}{6.125x10^{-4}}\right)$$

Figure 2.17 shows the yield strength increase predicted by the Orowan and Ashby-Orowan equations as compared to experiment results.

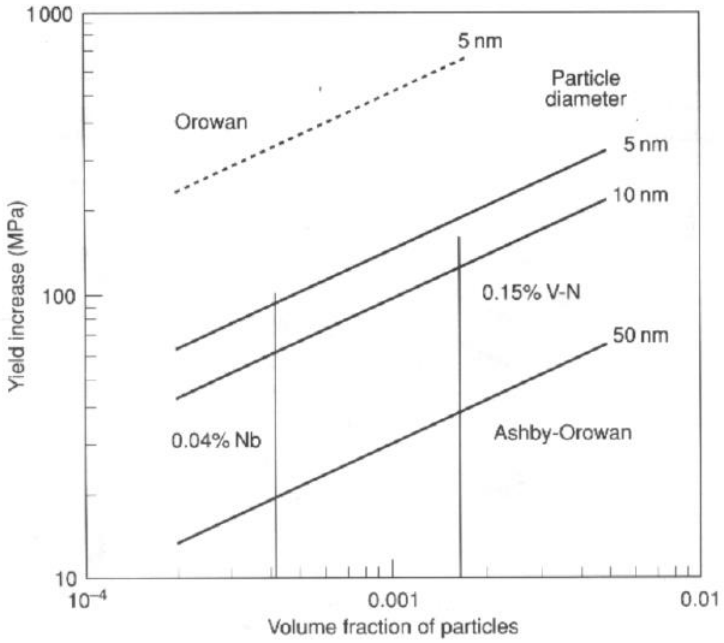

Figure 2.17 – Diagram showing observed precipitate strengthening and the Orowan and Ashby-Orowan equation predictions. [9]

3 THE UOE PIPE MAKING PROCESS AND THE BAUSCHINGER EFFECT

3.1 The UOE process

Large diameter welded pipes are used for oil and gas transportation. The method used for making these pipes is called the UOE process and consists of different steps of cold deformation, as follows. The process starts with a flat plate of dimensions similar to the dimensions of the desired pipe where the length, width and thickness of the plate correspond to the length, diameter and thickness of the pipe respectively. The first step is to add four small metal pieces, welded at each of the edges of the plate, which will aid the welding process. The edges of the plate are then crimpled to ensure a parallel contact between them before the welding, as shown in figure 3.01 a).

The next step is the U-pressing of the plate, in which the flat plate is deformed into a U shape by supporting the longitudinal edges of the plate with side rollers and pressing its centre, similar to a three-point bending test. The side rollers are then moved inwards to finish the U shape. This step is illustrated in figure 3.01 b).

The O-pressing is the next step of the process, where the U shaped plate is compressed between two semi-circular dies, forcing the plate into a circular shape, as shown in figure 3.01 c). Further compression is then applied after the O shape is achieved in order to avoid the spring back effect after unloading.

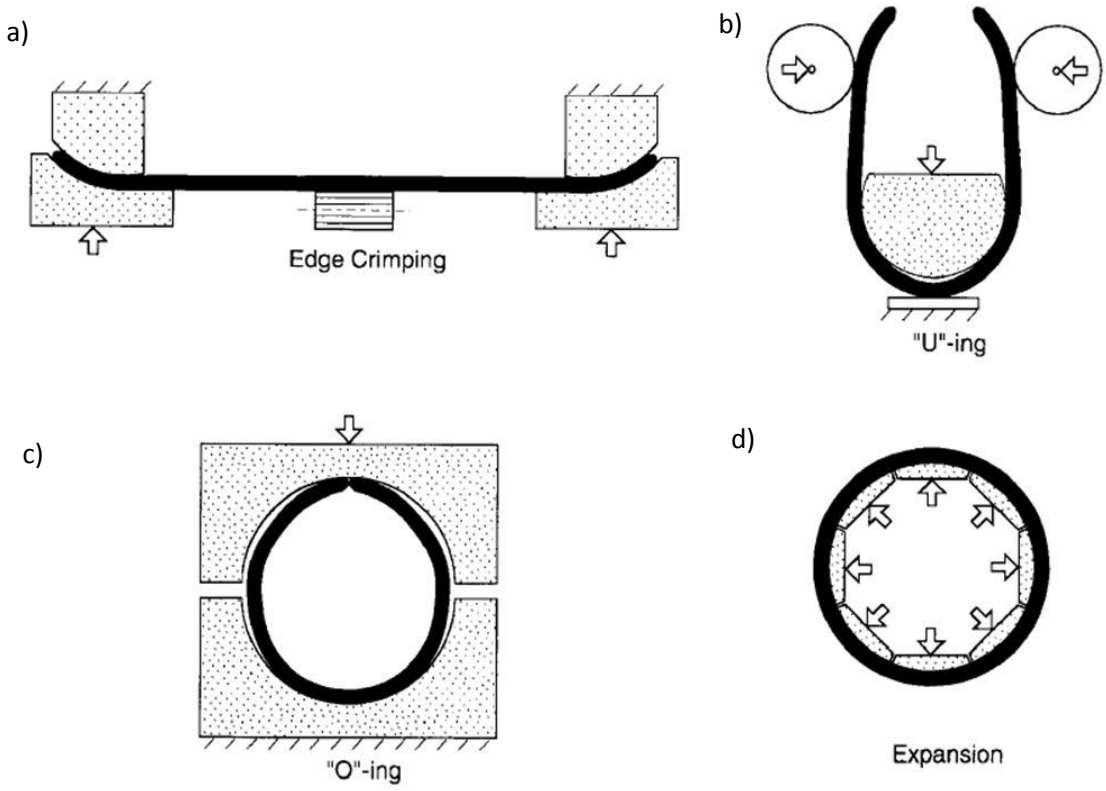

Figure 3.01 – The steps of cold deformation during the UOE process: a) crimping of the edges, b) the U-pressing, c) the O-pressing and d) expansion [39].

The pipe can then be welded internally and externally, with the welding arc starting at the small metal plates added previously, ensuring the continuity of the weld throughout its length, allowing the welding arc to become stable and homogeneous at these small plates, before passing through the pipe itself. Those tabs can then be removed from the pipe after the welding process is finished.

Following O-pressing and welding, the pipe diameter will be slightly smaller than the desired diameter of the final product and may present a slight oval shape due to the deformation steps of the process. Therefore, a last step of expansion is used to ensure

the correct diameter and roundness of the pipe at the end of the process. For this purpose, as shown in figure 3.01 d), a hydraulic mandrel is inserted in the pipe and expansion takes place, typically of 0.8 - 1.3% of its diameter after the O – pressing [2].

Each of these steps of the UOE process introduces plastic deformation to the material and the strain distribution can be explained as follows: considering bending of a flat plate, during the U – pressing, the inner side of the pipe wall will strain under compression, whereas the outer side of the pipe wall will strain under tension, however, the amount of strain is equal on both sides, with a neutral layer in the middle of the plate, as shown in figure 3.02.

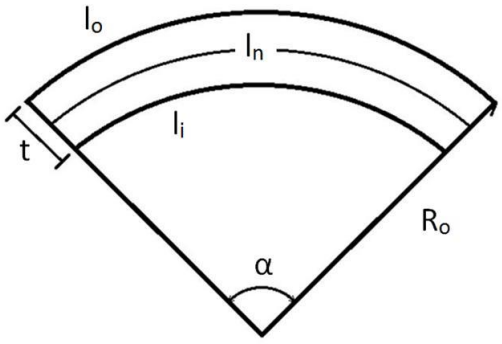

Figure 3.02 – Schematic diagram of the plate after bending, where t is the thickness of the plate, l_n is the initial length, lo is the length of the outer wall, l_i is the inner wall, R_o is the outer diameter of the pipe and α is the angle of bending.

Thus, the tension strain on the outer wall of the pipe after bending can be calculated as follows:

$$\varepsilon_o = \frac{l_o - l_n}{l_n} = \frac{\alpha R_o - \alpha\left(R_o - \frac{t}{2}\right)}{\alpha\left(R_o - \frac{t}{2}\right)} = \frac{t}{2\left(R_o - \frac{t}{2}\right)}$$

Likewise, the compression strain on the inner wall will be of the same magnitude:

$$\varepsilon_o = -\frac{t}{2\left(R_o - \frac{t}{2}\right)}$$

In the following steps of plastic deformation during the UOE process, unlike the U – pressing where bending of a flat plate occurs, straining is generated by compression or tension of the whole pipe wall, due to the compression or expansion in the diameter, as shown in figure 3.03.

Figure 3.03 – Schematic diagram of the radius change for a) compression and b) expansion.

Thus, the compression strain ε_c and expansion strain ε_e can be calculated as follows:

$$\varepsilon_c = \frac{2\pi r - 2\pi R}{2\pi R} = \frac{r - R}{R}$$

$$\varepsilon_e = \frac{2\pi R - 2\pi r}{2\pi r} = \frac{R - r}{r}$$

The pipe wall, therefore, after the UOE process, presents cycles of strain in the opposite direction (tension and compression), depending on the position of the cross section being considered. This is better explained in figure 3.04, showing the different paths of strain in different areas of the pipe wall after the process. It can be noticed that, at the top part of the pipe, the outer wall has gone through two compressive strains and one tension, and the inner wall has gone through tension, compression and tension. On the other hand, at the bottom part of the pipe, the outer wall has gone through two complete cycles of strain, compression, tension, compression and tension, whilst the inner wall has gone through tension, compression, compression and tension.

When the material is strained in the opposite direction after an initial deformation in the forward direction, it may present an asymmetry in the magnitude of the forward and reverse stress needed for plastic deformation to initiate. This phenomenon is called the Bauschinger effect.

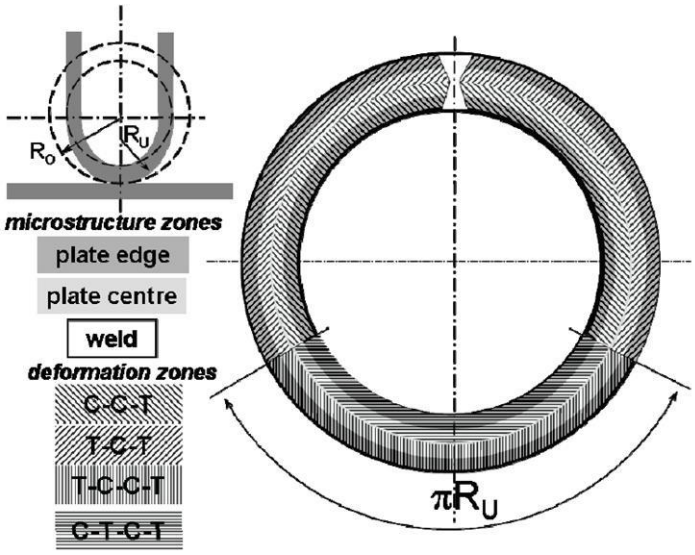

Figure 3.04 – Strain path in different areas of the pipe wall after the UOE process. Ru and Ro are the radius of the pipe after “U” and “O” pressing, respectively. C and T zones stand for strain in compression and tension, respectively. [33]

3.2 The Bauschinger effect

The Bauschinger effect consists of a decrease in the yield strength of the material when a reverse load is applied, following a pre-load in the opposite direction. For instance, when a sample is strained to its plastic region in tension, it will present one value for yield strength. After unloading the tensile force, if a compression load is applied, straining the material to its plastic region once again, the value for yield strength in compression will be lower than the previous yield strength in tension. An example of the Bauschinger effect is shown in figure 3.05.

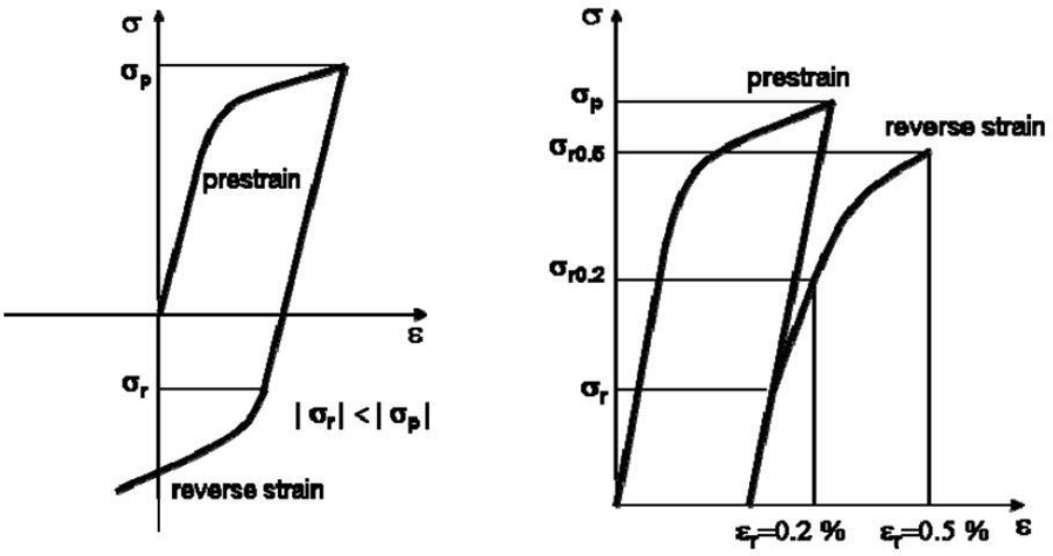

Figure 3.05 – a) Stress-strain curve illustrating the Bauschinger test; b) Reverse strain curve plotted with prestrain curve.

It can be noticed that, after applying a load in the reverse direction, the yield strength drops, when compared to the yield strength during forward deformation. Therefore, because the UOE process can cause work softening due to the cycles of tension/compression, it is very important to understand the exact causes and consequences of the Bauschinger effect, as it can cause a catastrophic failure during the subsequent application of the pipes, which may have to work under high pressure and temperature or an aggressive environment.

The parameters used to quantify the Bauschinger effect in terms of stress are as follows:

$$\beta\sigma p = \frac{\sigma_p - \sigma_r}{\sigma_p}$$

$$\beta\sigma_{0.2} = \frac{\sigma_p - \sigma_{r0.2}}{\sigma_p}$$

$$\beta\sigma_{0.5} = \frac{\sigma_p - \sigma_{r0.5}}{\sigma_p}$$

where σ_p is the value for stress at maximum forward strain, σ_r is the yield strength in reverse deformation, $\sigma_{r0.2}$ is the value for stress at 0.2% reverse strain and $\sigma_{r0.5}$, the value for stress at 0.5% reverse strain, as shown in figure 05 b). The stress parameter $\beta\sigma p$ is a direct evaluation of the strength lost from forward to reverse deformation, whereas the parameters $\beta\sigma_{0.2}$ and $\beta\sigma_{0.5}$ offer an insight into the rate of strength recovery. In addition, a value of permanent softening ($\Delta\sigma_s$) can be quantified by taking the difference between what *would* be the value of stress in forward deformation ($\sigma_p + \Delta\sigma_s$) at the strain ($\varepsilon_r$) at which the value of the reverse stress reaches the same value as the forward stress σ_p, as shown in figure 3.06.

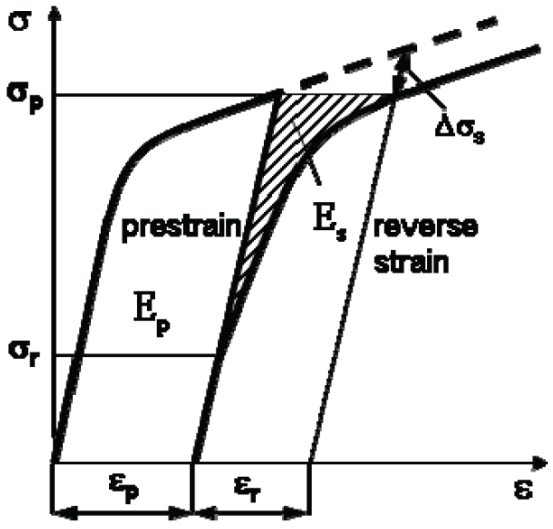

Figure 3.06 – Stress-strain curve illustrating the permanent softening ($\Delta\sigma_s$) and the values used to calculate the Bauschinger strain and energy parameters.

The Bauschinger effect can also be quantified in terms of strain (βε) and energy (β_E) parameters. These parameters evaluate the amount of strain or energy necessary to achieve equal values of strength in forward and reverse deformation, as follows:

$$\beta\varepsilon = \frac{\varepsilon_r}{\varepsilon_p}$$

$$\beta_E = \frac{E_s}{E_p}$$

where ε_r and ε_p are the strain in reverse and forward direction respectively, where the value of maximum forward stress (σ_p) is achieved, E_s is the amount of energy saved in the reverse direction and E_p is the amount of energy required in the forward deformation, as illustrated in figure 3.06.

A theory that can explain the Bauschinger effect was given by Orowan, which states that dislocation movement during forward plastic deformation results in interactions between mobile dislocations and particles, grain boundaries and other dislocations. These interactions prevent dislocations from moving, creating a force in the opposite direction to the movement. During unloading, these dislocations will be locked in this high energy state. Applying a reverse load will release the dislocations, causing them to move in the opposite direction but, because they were locked in a higher energy state, the energy required to start the movement is lower than the energy under forward load. Consequently, the yield strength during reverse loading will be lower than the yield strength during forward loading. Figure 3.07 illustrates schematically the interaction between mobile dislocations and obstacles, generating a back stress.

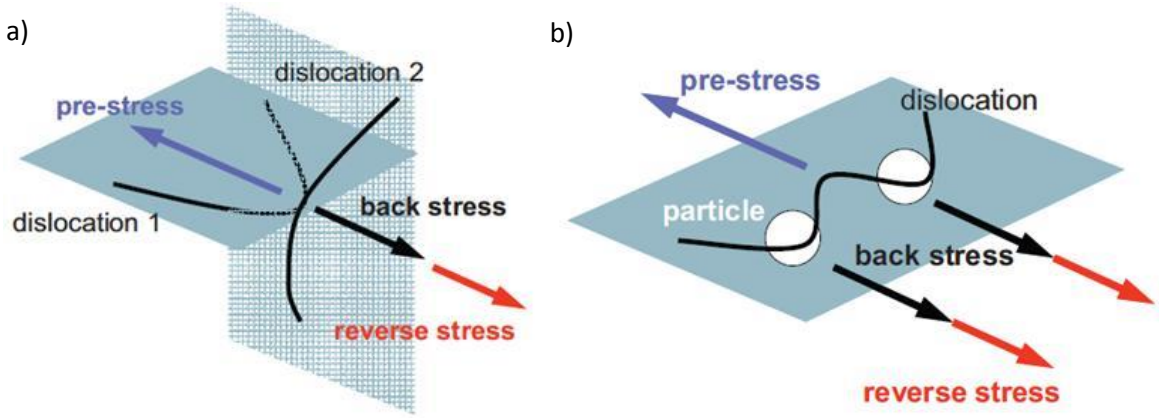

Figure 3.07 – Interaction and back stress between: a) dislocation-dislocation; b) dislocation-particle.

Orowan´s explanation was further expanded by Brown, who concluded that the back stress generated by the interaction between mobile dislocations and obstacles would cause the early yielding during reverse loading, but it would not cause permanent softening. The reason for that is that these interactions generate zero mean stress in the matrix, as they cause isotropic frictional resistance to flow, equally impeding the movement of dislocations in the forward and backward directions. Brown, therefore, proposed that a second mechanism for the Bauschinger effect is necessary to generate permanent softening.

This second mechanism that causes permanent softening consists of the interaction between the dislocations and the Orowan loops stored around particles, formed during the forward plastic deformation. In this case, during reverse deformation, the dislocation moving back towards the particle will not interact with the particle due to the Orowan loop created previously, not generating the strengthening effect

experienced during forward deformation. This mechanism is illustrated in figure 3.08, which shows a single dislocation after forward deformation in a), moving from left to right and generating Orowan loops (highlighted with arrows) around the particles, whereas in b) the same single dislocation moves from right to left during reverse deformation, bypassing the particles due to the Orowan loops.

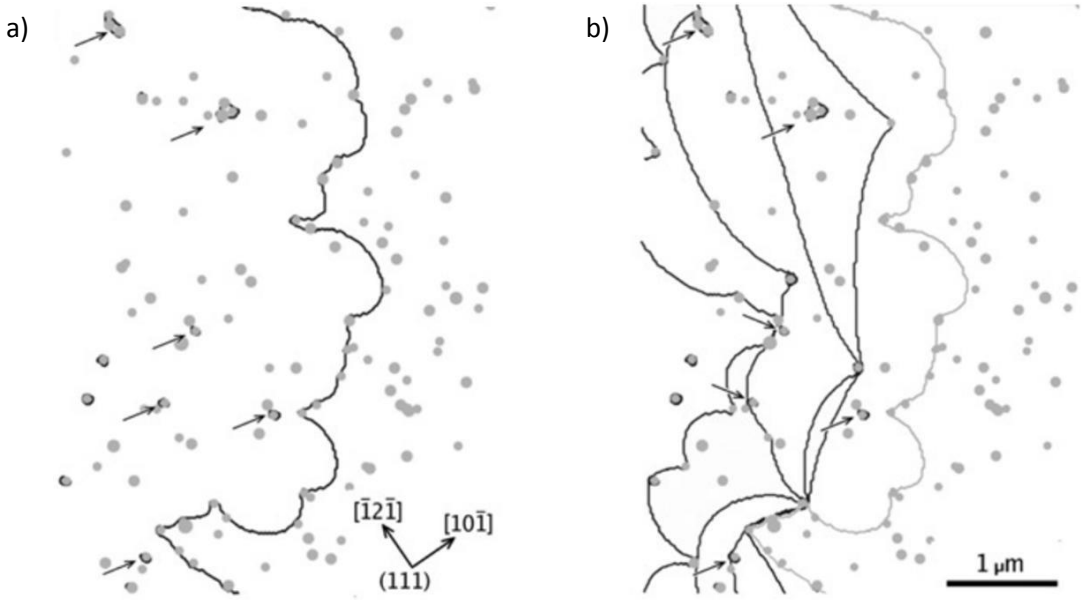

Figure 3.08 – Interaction between dislocation and particles during: a) forward deformation and b) reverse deformation [40].

Academic research on the Bauschinger effect has been carried out on a variety of materials due to its importance in the deformation and manufacturing processes. However, the majority of previous work has been concentrated on one strengthening

mechanism (i.e. grain size; pre-strain; amount of second phase; etc.), ignoring or only lightly discussing other aspects. It is certainly difficult to make a complete analysis of all the Bauschinger effect causes from one single experiment and material system, as there are often more than one variables involved in a single experiment.

Studies of the effect of grain size on the Bauschinger effect have shown that there is no relationship between Bauschinger effect and grain size in the range of 72 to 15 μm [41] or that, depending on the dislocation source density and grain crystallography, there is a transitioning grain size above which Bauschinger effect is independent of the grain size and below which Bauschinger effect increases with decreasing grain size [42, 43]. This indicates that the stress induced by a grain boundary blocking the movement of dislocations does create back-stress, thus, resulting in Bauschinger effect. However, there could be a limited distance the dislocation can travel before reaching a grain boundary, otherwise it will interact with a different obstacle.

Bauschinger effect is also found to increase with higher initial yield strength and the increase of plastic deformation (pre-strain/dislocation density) [33, 44, 45, 46]. This increase in the Bauschinger effect has been related to the increased strength generated by the presence of second phase constituents and the higher dislocation density/multiplication. As dislocation density increases, a greater number of dislocation – obstacle interactions take place, therefore, greater back-stress is generated, increasing the Bauschinger effect.

Similarly, increasing the volume fraction of precipitates has been found to increase the Bauschinger effect [33, 46]. Dislocation – particle interactions also generate back-

stress, therefore increasing the amount of particles results in increasing the Bauschinger effect. Dislocations have also been found to mask precipitates after their interaction, which makes the particle invisible to a dislocation moving in the opposite direction [40], reducing its strengthening effect upon reverse loading.

4 MICRO BAUSCHINGER TESTS

4.1 Sample size and the Bauschinger effect

One field that has not been deeply studied is the effect of the size of the sample on the Bauschinger effect. In the literature there has been some interest in the Bauschinger effect in thin films, usually made by chemical deposition of Cu, Al or Au [47, 48]. In addition, passivation of the surfaces of the thin films with a second layer, usually Si_3N_4, was also studied in order to compare the results of the freestanding and passivated films [47, 49].

Results from these experiments showed that the passivated films, after forward strain, presented a strong film thickness effect and, due to the generation of a back stress near the interface between the film and the passivation layer, presented Bauschinger effect as well. On the other hand, freestanding films, those with no presence of a passivation layer, presented little to no Bauschinger effect at all. It is supposed that, as these films do not present an interface between layers, dislocations move to the surface of the specimen, where back stress cannot be generated and, therefore, there is no Bauschinger effect, as illustrated in Figure 4.01.

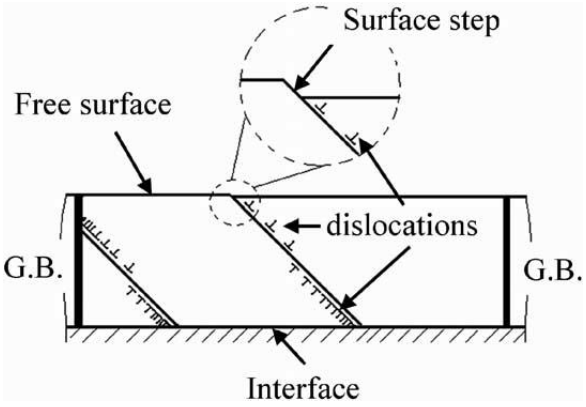

Figure 4.01 – Schematic diagram showing the dislocation behaviour in a thin film with one free surface (top) and one passivated surface (bottom) [47].

The effect of microstructural heterogeneity has also been reported to influence the Bauschinger effect [50]. Randomly oriented grains and a wide distribution of grain sizes has shown a large Bauschinger effect during unloading, whereas little Bauschinger effect was present in a microstructurally homogeneous film with comparable mean grain size.

These studies compared the effect of the interface between the thin film and the passivation layer to the effect of grain boundaries in a bulk material. In the bulk material, during plastic deformation, back stress is generated by dislocations being blocked by and piled up at grain boundaries, resulting in a Bauschinger effect. Making the analogy, if there were no grain boundaries, there would be no Bauschinger effect. This assumption, however, does not take into account the effect of the interaction between mobile dislocations and other dislocations, precipitates and the solid solution effect.

In addition, the deposition techniques used for these studies cause the loss of the initial microstructure of the material, consequently making a direct comparison with the as-received material difficult.

It is important, therefore, to understand more deeply the effects on the Bauschinger effect of the size of HSLA samples, so that an analysis of each of the causes of the Bauschinger effect can be made.

4.2 Microelectromechanical systems (MEMS)

Broadly speaking, MEMS consist of micro mechanical sensors, actuators and microelectronic circuits which can be integrated into one system. Pressure sensors, accelerometers and gyroscopes are some of the wide variety of applications of these devices.

The development of such devices has arisen from the development of semiconductor technologies and the vast improvement in manufacture of electronic devices and the pursuit for miniaturization of such devices. Very high precision processes of lithography, physical and chemical deposition, as well as wet and dry etching, have been responsible for the development of very complex, small high precision systems.

One example of these complex structures which has been used as an in-situ TEM straining device is shown in figure 4.02. This MEMS is applied in a novel way to analyse the chiral indices of single-walled carbon nanotubes (SWNTs) [51]. It consists of an electrically heated thermomechanical actuator connected to one tip of the stage while

the other tip is fixed, allowing the sample to be strained by the movement of the actuator, controlled by passing an electric current through it, causing the actuator to expand (and then to contract). This device allows for TEM inspection through a notch etched during the MEMS manufacture.

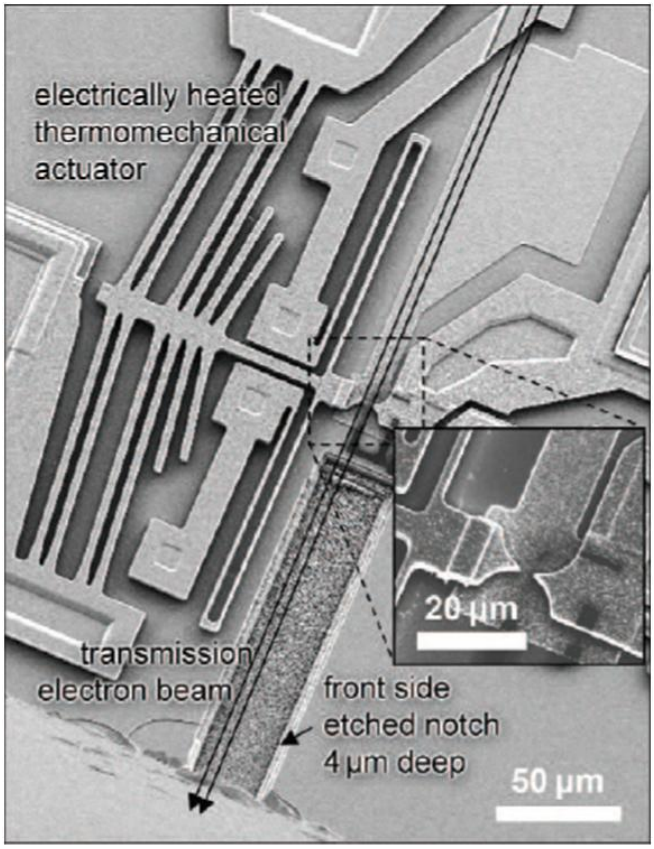

Figure 4.02 – A MEMS device with an electrically heated thermomechanical actuator used in-situ in the TEM in order to analyse the chiral indices of carbon nanotubes. [51]

4.3 Straining MEMS device idea

For the purpose of carrying out Bauschinger tests in micro sized samples, the development of a new straining stage is required. As seen previously, MEMS have been successfully applied in mechanical testing and, specifically, Bauschinger testing of thin films. However, the samples used in these studies were produced by depositing the material on a straining stage, which causes the loss of the initial microstructure. Thus, the new straining stage must be able to support a “free standing” sample which must then be gripped to the stage, so that the initial microstructure is left intact for the purpose of comparing the macro and micro sized samples.

Figure 4.03 shows one MEMS device, developed by Haque and Saif, used for straining a thin film which, due to its capabilities and relatively simple structure, has been chosen as the starting place for the development of a micro Bauschinger test stage.

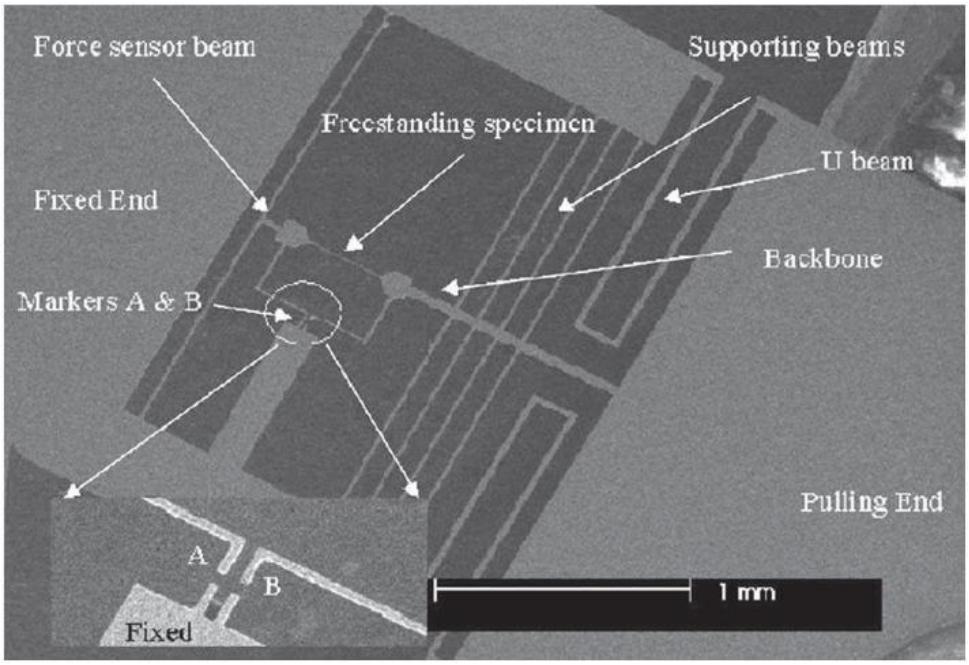

Figure 4.03 – An SEM image showing the detailed structure of a MEMS device used as a straining stage. [52]

The structure of this MEMS consists of a force sensor beam which is connected to the specimen and the fixed side (left) of the device. This force sensor beam acts as a spring during the mechanical test, deflecting as the force is applied. As the spring constant is known from the beam´s dimensions, the force can be calculated.

The other side of the sample is connected to a column (backbone) which is directly connected to the moving side of the device (right). This column is also connected by supporting beams connected to the fixed side of the device. These supporting beams retain the movement of the backbone as linear and centred on the direction of the specimen, avoiding bending of the specimen during the mechanical tests. A finite element analysis has shown that a misalignment of the device of 18 degrees can be

reduced to 1.33×10^{-5} degrees to the sample [53], as illustrated in figure 4.04. In addition, the fixed side of the device is connected to the moving side of the device by a couple of U beams, which provide structural support between both sides but also allows movement to be transferred between them.

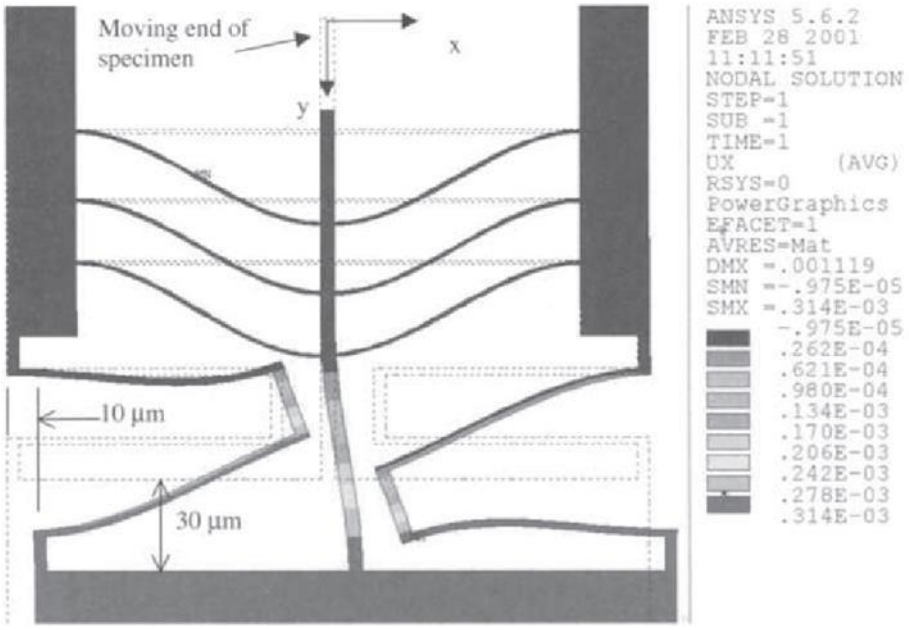

Figure 4.04 – Results of a finite element analysis of the behaviour of a MEMS misaligned by 18 degrees when a force is applied. [53]

This type of MEMS does not include an integrated actuator and therefore an external force is required. Haque and Saif used a piezo-actuator mounted on a fixed column, with one end of the MEMS glued to the actuator and the other side glued to the column, as seen in figure 4.05 below.

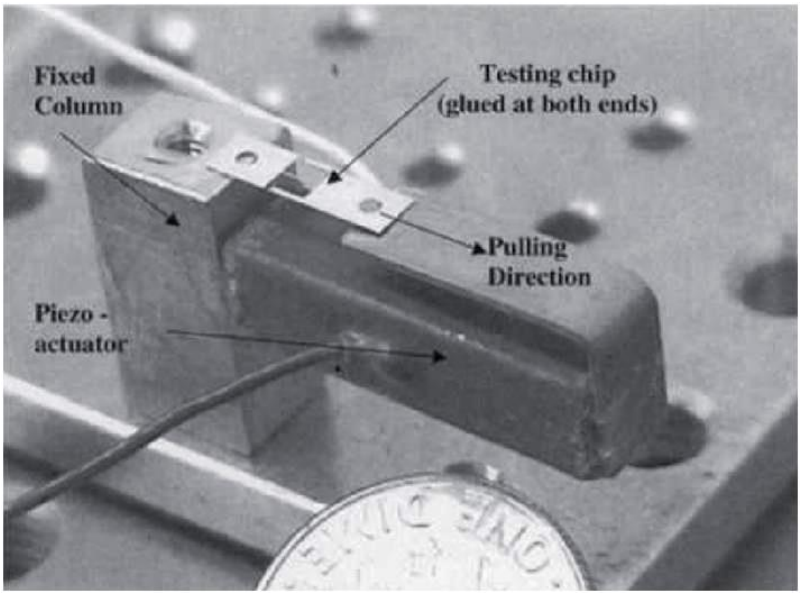

Figure 4.05 – Test setup showing the position of the MEMS and the piezo-actuator. [53]

4.4 Straining MEMS device development

Taking the successful MEMS design from the works of Haque and Saif [52] as foundation, a modified version was required to be developed in order to be used with the HSLA steels of the current project. In addition, the MEMS development had the support of expertise and equipment from the Mechanical Engineering Department of the University of Birmingham. As a result, their advice has had a direct impact on the material and process used for the MEMS manufacture.

The first step in this development was to determine the dimensions of the device, its internal structures i.e. the force sensor beam, supporting beams and the U-beams. The equations used to calculate the internal structure dimensions were as follows:

$$F = k.x$$

which is Hooke´s law, F is the force applied, x is the displacement and k is the spring constant.

$$F = \frac{192EIx}{L^3}$$

which is the force at the centre of a beam with two fixed supports, where F is the force applied, E is the Young´s Modulus of the material, I is the moment of inertia of the beam, x is the displacement and L is the length of the beam.

$$I = \frac{tw^3}{12}$$

which is the moment of inertia of a beam with a rectangular cross-section, where t is the thickness of the beam and w is the width of the beam (dimension in the plane of bending).

The material selected for the device was a 500 µm thick polished silicon wafer of 100 mm in diameter. Silicon wafers are manufactured with a specific crystal orientation and, in the case used in this project, the direction normal to the surface of the wafer is [100] and the direction parallel to the wafer´s notch is [110], as illustrated in figure 4.06.

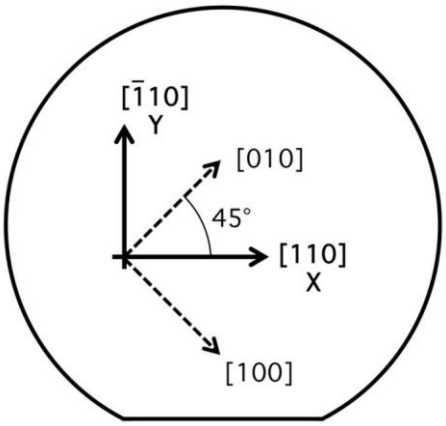

Figure 4.06 – Schematics of the silicon wafer showing its crystal orientation.

With these parameters established, the external dimension of the device was designed as a rectangle 10x5 mm and 0.5 mm thick, with five different sets of internal structure dimensions in order to accommodate a wide range of specimen sizes, from 0.5 μm² to be tested in-situ in the TEM up to 50 μm² to be tested in-situ in the SEM. In addition, using different sets of devices was desirable in order to account for any problems during manufacture process, increasing the chances of success. Figure 4.07 shows the 5 different sets, from column A (50 μm²) to E (0.5 μm²), spread as 52 MEMS straining stages on one silicon wafer.

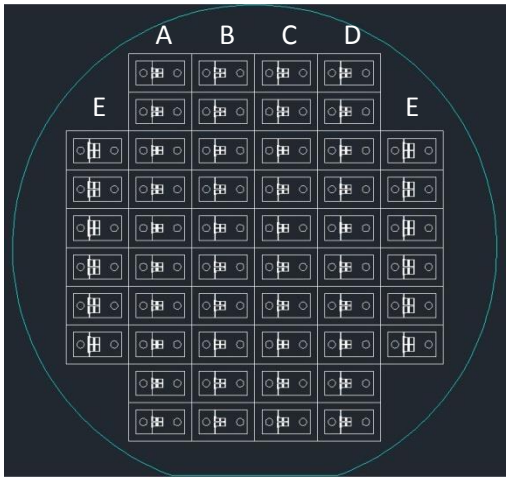

Figure 4.07 – Position of the MEMS straining devices on the silicon wafer.

The manufacturing phase of the project was made inside a clean room, using a MESC Multiplex ICP system applying a Deep Reactive Ion Etching (DRIE) Bosch process. This process consists of applying a pattern onto the surface of the silicon wafer using a lithography technique followed by plasma etching of the substrate around the pattern.

The lithography technique starts with applying a single 8 µm thick layer of photoresist ROHM HAAS SPR220 onto a clean silicon wafer surface, placed on a spinner. The speed of the spinner was initially 500 RPM for 15 seconds to spread the photoresist homogeneously across the surface of the wafer, followed by 30 seconds at 3000 RPM in order to achieve the desired thickness of the photoresist, finally finishing at 500 RPM for 5 seconds. Following its application, the photoresist is set by heating the wafer using a hot plate set at 95°C for 90 seconds.

The silicon wafer was then placed under a lithography mask to be selectively exposed by a source of light. The mask used was a Chrome Soda Lime Super High Resolution

5x5x0.090 inches supplied by JD Photo-tools. An MF 26-A developer is then used to dissolve the exposed photoresist by gently stirring the silicon wafer in a petri dish covered with the developer. This should remove the photoresist exposed, leaving a pattern of the MEMS device on the surface of the silicon wafer. The wafer was then cleaned using distilled water and blown dry using compressed hydrogen. At this stage, the wafer is ready to be etched and is loaded into the MESC Multiplex ICP.

The DRIE Bosch process is characterised by alternating pulses of plasma etching, which remove exposed material, followed by a passivation layer, protecting the recently etched surface. This then repeats, etching the bottom of the pattern and protecting the walls. Due to this passivation layer, this process presents the advantage of creating larger etch depths.

Modifications to the standard process had to be made due to overheating of the wafer, causing damage to the fine beam structures of the MEMS device. The addition of cooling cycles in between etching cycles improved slightly the results, but only the set of devices designed with the larger internal structures retained their integrity with only small over-etch marks on the edges, whilst the ones with smaller internal structures were damaged, inhibiting their use, as shown in figure 4.08.

a)

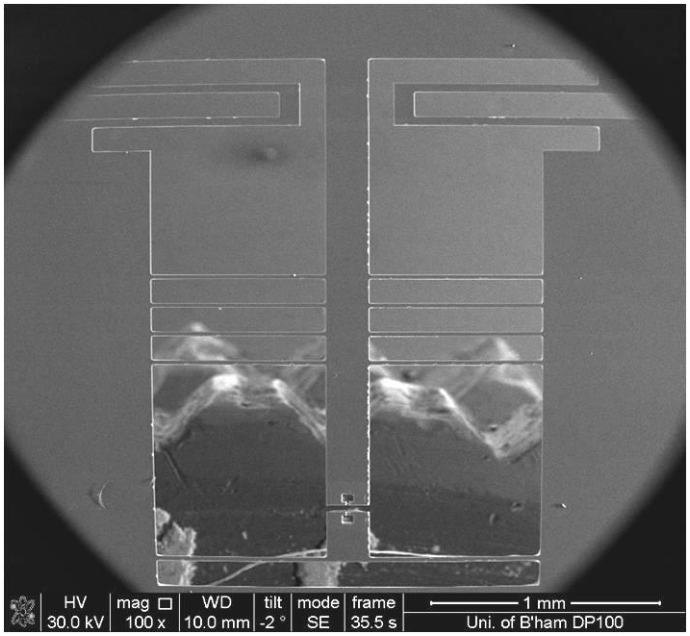

b)

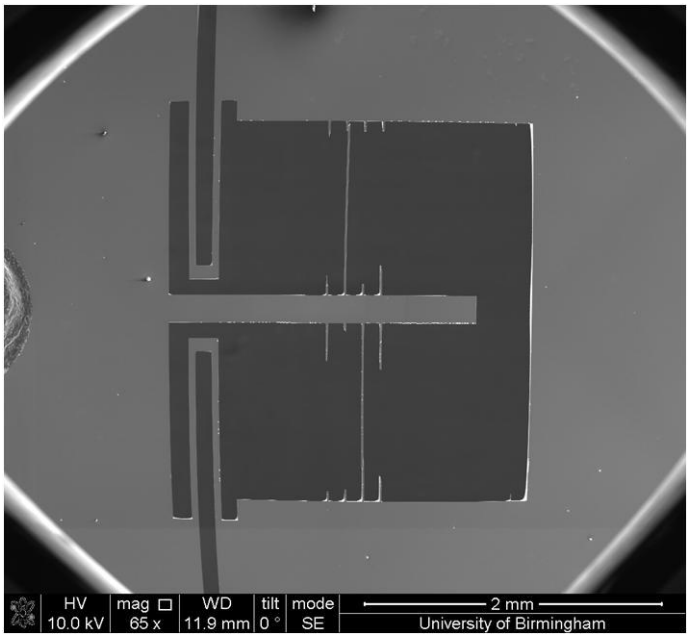

Figure 4.08 – SEM image showing a) the MEMS straining stage with the largest internal structures and b) one with a smaller damaged internal structure.

The most successful process was found to be as follows: oxygen plasma clean for 150 seconds in order to remove all organic contaminants. The plasma etching cycle was

made using sulphur hexafluoride (SF_6) gas for 11 seconds, followed by a plasma passivation cycle with octafluorocyclobutane (C_4F_8) gas for 4 seconds and a cooling cycle for 15 seconds. This 30 second cycle was repeated 480 times, lasting 4 hours.

Along with the MEMS straining stage development, an external actuator was required as one was not integrated to the straining stage. For this purpose, two Piezo Motor Driven Linear Stage AG-LS25V6 supplied by Newport Corporation were used, mounted on top of each other with 90° rotation to provide X and Y direction movement. A platform on top of this combination was used to mount one side of the MEMS straining stage, and a fixed second platform, both with a 1 mm pin near the edges which connected to 1.5 mm slots on the MEMS stage in order to transfer movement. Silver paint was used first to fix the MEMS stage to the platforms, but the solid grip meant that the fragile interior structures of the device would break as a result of very small vibrations. Thus a modification to pin and slots was required to avoid breaking the straining stage.

Because FIB was going to be used to mill the straining specimens, this equipment required an adjustable height system in order to maintain the necessary 10 mm working distance for the microscope. This was achieved using an extra pair of nuts on the bolts which attach the equipment to the stage of the microscope and the height was adjusted with the aid of a precision calliper. The actuator system and the MEMS straining device on the platforms, mounted on the stage of the microscope, can be seen in figure 4.09 below.

a)

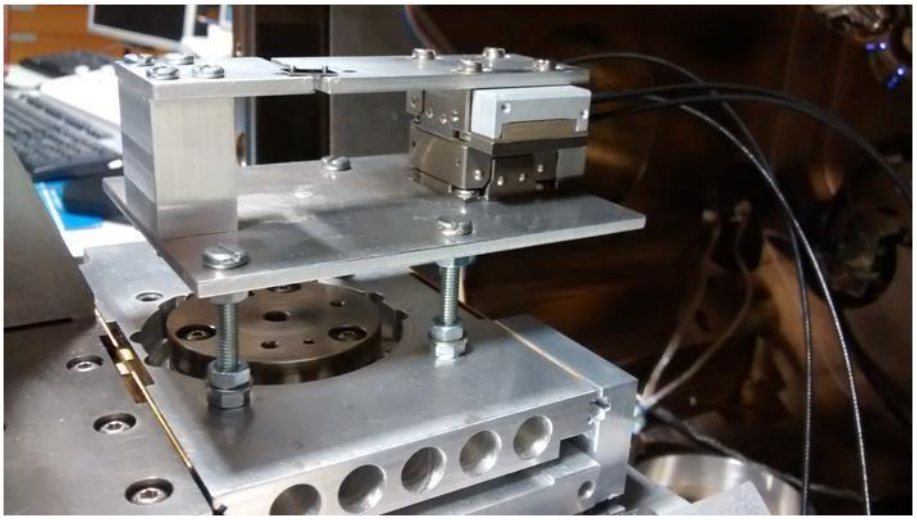

b)

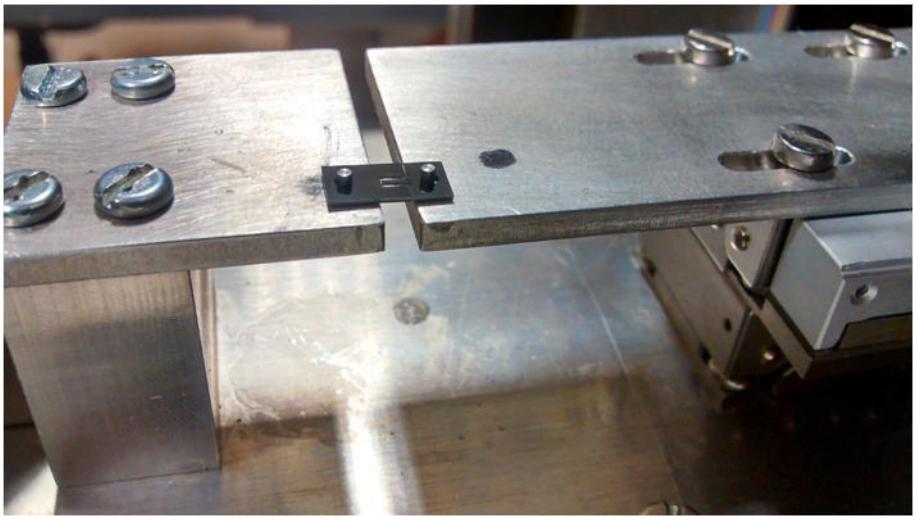

Figure 4.09 – Pictures showing a) the actuator system mounted on the stage of a FIB microscope and b) the MEMS straining device mounted on the pins on the platforms of the actuator system.

After the conclusion of the etching process of the MEMS straining stage, along with the actuator system, the next step was to develop grips where the specimen would sit during the Bauschinger tests. This stage was developed using Focused Ion Beam

microscopy. For this purpose, a dog bone shaped trench was milled from the centre beam and the force beam, as shown in figure 4.10.

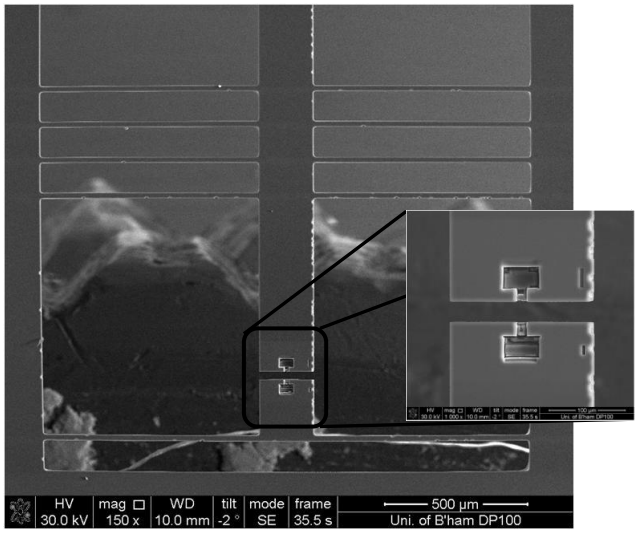

Figure 4.10 – SEM image showing grips milled on the centre column.

Similarly, the specimen was produced using the same technique, milling a dog bone shape from the as-received material. However, in order to make the specimen, different approaches had to be tried. Milling of the bulk material was not possible due to the angles required to lift the sample, whilst milling from a corner of the bulk material turned out to be extremely time consuming, due to the large depths required. Finally, success was achieved using a 3 mm wide and 50 µm thick disc, prepared similarly to a TEM sample. In this way, it was not necessary to mill large portions of material. The 3 mm discs were mounted on a 45° stage to improve access to different angles when tilting the specimen during the milling process. Figure 4.11 shows the 3 mm discs positioned for milling.

a) b)

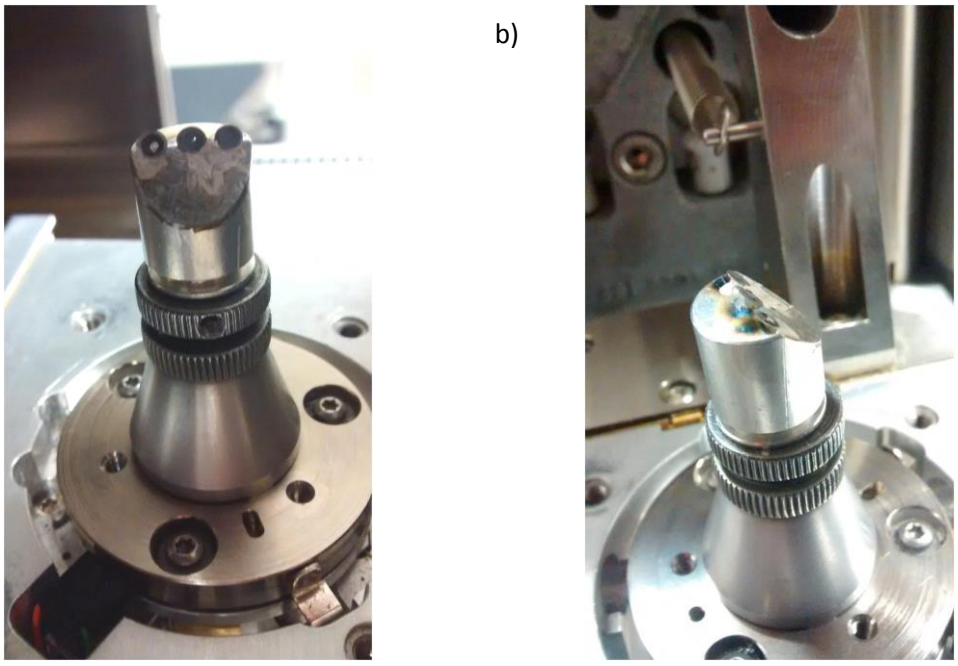

Figure 4.12 – Pictures showing the positioning of the 3 mm discs for milling the samples for the Bauschinger tests from a) the front and b) the side.

Figure 4.13 shows the sequence of the FIB milling process on the specimen, starting with thinning the edges and making them parallel, followed by thinning the gauge length to the desired thickness. After tilting the stage, milling of the dog bone shape takes place, leaving one edge connected, until a final thinning of the gauge length is achieved. The stage is tilted one last time and the omniprobe is attached to the sample via a tungsten deposition. The specimen is then detached from the 3 mm disc with milling of the remaining edge and lifted with the omniprobe; finally, the last step is to mount the specimen on the MEMS straining device and then detaching from the omniprobe.

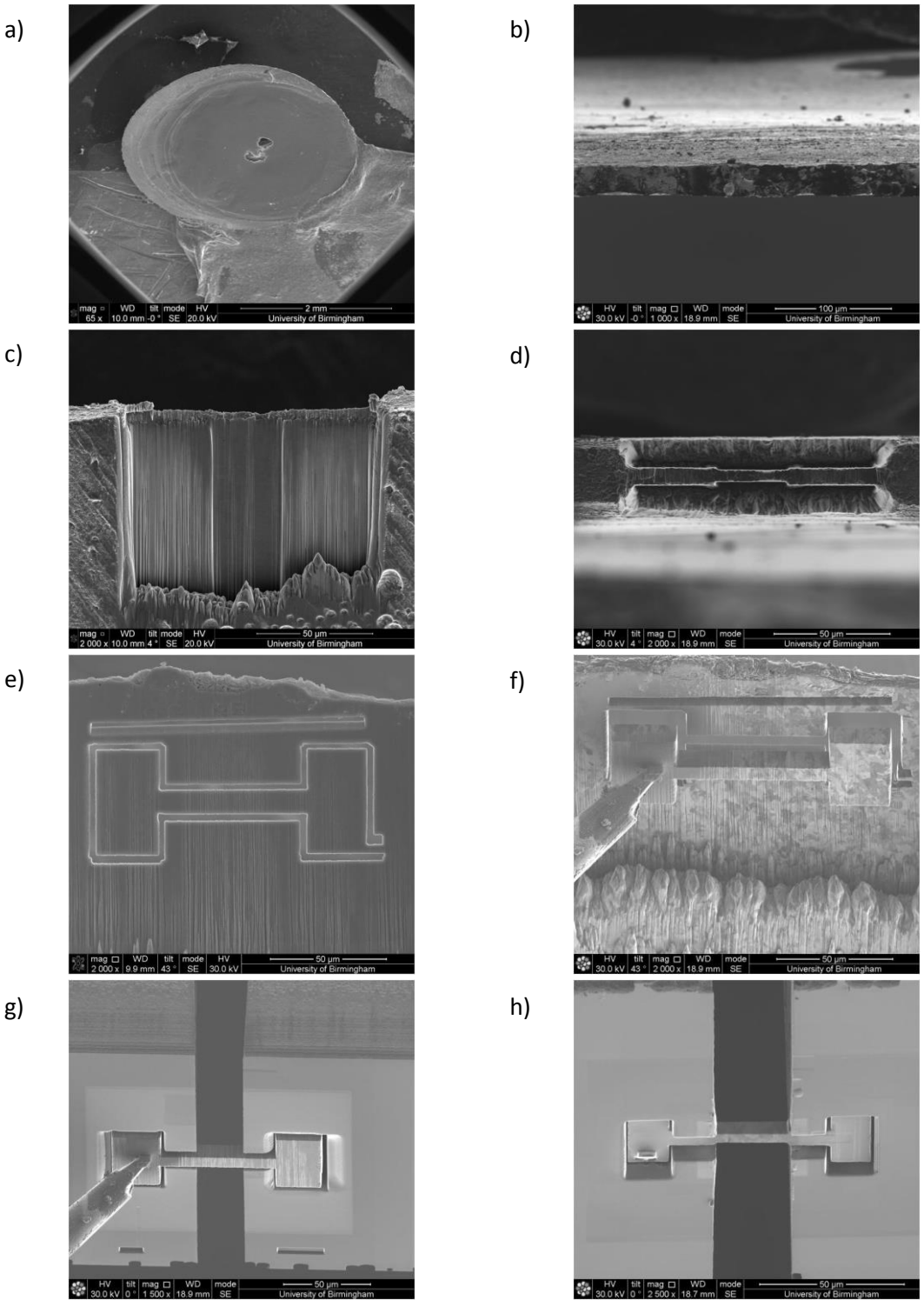

Figure 4.13 – Sequence of SEM micrographs showing the milling of the Bauschinger test specimen a) the initial 3 mm disc, b) positioning the edge of the sample, c) and d) thinning the edge and making a parallel surface, e) milling the dog bone shape, f) lifting the specimen from the disc, g) mounting the specimen on the MEMS straining device and, h) detaching it and sitting in the grips.

After detaching the specimen from the omniprobe, little work is needed other than the final thinning and polishing of the gauge length, otherwise the material milled is readily redeposited on the nearby area, which, in excess, may cause damage to the MEMS device or influence the straining of the specimen.

In order to guarantee the quality and effectiveness of the Bauschinger test results, every effort must be spent on the pursuit of a perfect match between the contacting walls of the MEMS device and the specimen. This is especially difficult due to the fact that the FIB milling process does not produce perfect 90° corners/edges. As the milling digs deeper, rather than having a straight line parallel to the bottom, the wall grows outwards. In an attempt to counterbalance that, extra tilting of the microscope stage is needed, usually between 2° to 5°, during the preparation of both specimen and the grips on the MEMS straining device. If this is not taken into consideration, buckling of the sample during the Bauschinger test will most certainly occur, as exemplified by figure 4.14.

Lastly, the stress-strain data were taken from the measurements of the deflection of the force beam and the change in the gauge length after every step. Both measurements were taken using the length measurement feature on the microscope´s software. Even though this feature is good enough for measuring the linear change in the deflection of the force sensor, however its resolution is far too low to permit accurate readings of the strain changes of the specimen. For this reason, a photo was taken of the specimen after every step of the Bauschinger test and was analysed

afterwards using the ZEISS software AxioVision and, in doing so, the resolution of the strain reading is only limited by the resolution of the image available to the software.

a)

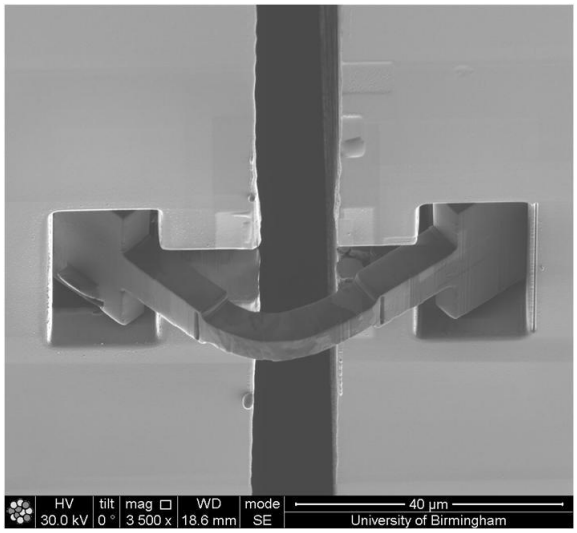

b)

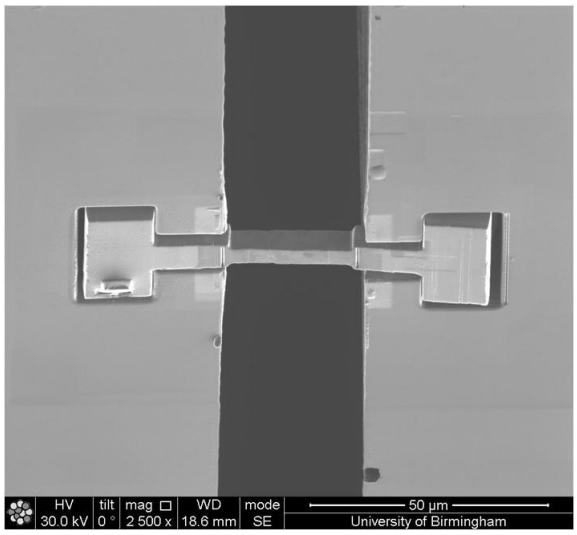

Figure 4.14 – SEM micrographs of the Bauschinger effect showing the buckling of the specimen under a) compression and b) tension.

5 MATERIALS AND EXPERIMENTAL TECHNIQUES

5.1 Materials

Samples were supplied under three different API (American Petroleum Industry) classifications, X70, X80 and X100. The chemical compositions of the three samples are shown in the table 5.01.

Table 5.01 – Chemical compositions for X70, X80 and X100 alloys (wt %).

Element	**X70**	**X80**	**X100**
Carbon	0.042	0.059	0.067
Silicon	0.23	0.10	0.10
Manganese	1.53	1.87	1.88
Phosphorus	0.0088	0.0058	0.0058
Sulphur	0.0025	0.0021	0.0022
Chromium	0.021	0.032	0.032
Molybdenum	0.14	0.27	0.27
Nickel	0.19	0.55	0.54
Niobium	0.062	0.032	0.033
Vanadium	0.0039	0.0055	0.0055
Titanium	0.0140	0.0083	0.0086
Copper	0.16	0.31	0.30
Boron	0.0002	0.0002	0.0002
Aluminium	0.030	0.040	0.041

5.2 Thermodynamic modelling

Database 7 of the Thermo-Calc software was used to predict the amount of secondary phases and precipitates expected in the three alloys during cooling from 1600 to 600 °C. The chemical compositions used to conduct the modelling were taken from Table 5.01.

5.3 Scanning electron microscopy (SEM)

Samples for SEM analysis were mounted in Bakelite, ground using silicon papers up to 1200 mesh and polished using a polishing cloth with 1 µm diamond compound until a mirror-like surface was achieved. In order to reveal the microstructure, a solution of 3% nitric acid in ethanol (nital) was used to etch the surface of the samples to be analyzed for 8 to 10 seconds, cleaned with ethanol and cotton wool and blow dried.

The SEM used was a JEOL 7000 equipped with a field emission gun operated at 20 kV and an OXFORD Instruments energy dispersive X-ray detector with INCA software. The images taken were used to measure the grain size, the volume fraction of the large precipitates (20 nm and larger) as well as the amount of second phase of the alloys.

Grain size measurements were made using the linear intercept method, in which random straight lines are drawn and the result is related to the length of each line and the number of times the line intercepts a grain boundary. The volume fraction of precipitates and the amount of second phase were calculated with the aid of ImageJ software. Around 500 images were used for each alloy.

5.4 Transmission electron microscopy (TEM)

A JEOL 2100 HT and a FEI TECNAI F20 were used for the TEM analysis in this project. Samples were prepared using an electrical discharge machine (EDM) to cut 300 µm thick slices which were ground down to 150 µm from both sides. EDM was again used to cut out 3 mm discs from the slices which were then ground down to a thickness between 30 to 50 µm. A Struers Tenupol 3 twin jet electropolisher was used at 30 V to polish the TEM 3 mm discs with a solution containing 5% perchloric acid and 95% acetic acid cooled to -10°C using liquid nitrogen. After electropolishing, the TEM specimens were cleaned in a sequence of three glass beakers containing ethanol.

TEM was used for the study of the dislocation structure in the as-received material, which was compared to the compressed samples as well as the macro Bauschinger tested samples. The analysis of dislocations by TEM used several two beam conditions and the g.b=0 criterion for invisibility. Dislocations whose Burgers vector is perpendicular to the g vector will be invisible. For instance, in BCC materials, as is the case for ferrite, the Burgers vectors are from the <111> family. Thus a Burgers vector $b = \frac{a}{2} < 111 >$ will be out of contrast with g vectors = $0\bar{1}1$ and $10\bar{1}$.

The dislocation density (ρ) was calculated as follows:

$$\rho = \frac{L}{V^3}$$

where L is the total length of the dislocation lines and V is the volume of the material.

In order to calculate the volume of the material, the thickness of the TEM thin foil needs to be measured. For this purpose, the convergent beam electron diffraction (CBED) technique was used and applied to the relationship between the extinction distance "ξ_g" and thickness "t" given by:

$$\left(\frac{s_i}{n_i}\right)^2 + \left(\frac{1}{n_i}\right)^2 \left(\frac{1}{\xi_g}\right)^2 = \frac{1}{t^2}$$

where s_i is the spacing deviation parameter and n_i is an integer assigned to the CBED fringes counting outwards from the centre line. s_i can be determined from the spacing of the CBED fringes by:

$$s_i = \frac{\lambda}{d^2}\left(\frac{\Delta\theta_i}{2\theta_d}\right)$$

where d is the plane spacing of the operating reflection, λ is the wavelength of the incident electrons, $\Delta\theta_i$ is the distance from the centre line and $2\theta_d$ is the distance between the transmitted spot and the diffracted spot. A CBED pattern is shown in figure 5.01.

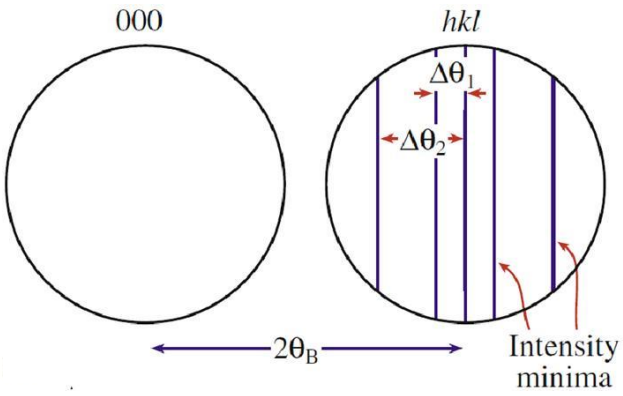

Figure 5.01 – Illustration of the convergent beam electron diffraction showing the transmitted and diffracted discs and the vertical fringes on the diffracted disc.

The TEM foil thickness "t" is then given by the interception of the line with the $\left(\frac{s_i}{n_i}\right)^2$ axis when plotting a $\left(\frac{s_i}{n_i}\right)^2$ against $\left(\frac{1}{n_i}\right)^2$ graph, if the integer "n" results in a straight line, as illustrated in figure 5.02.

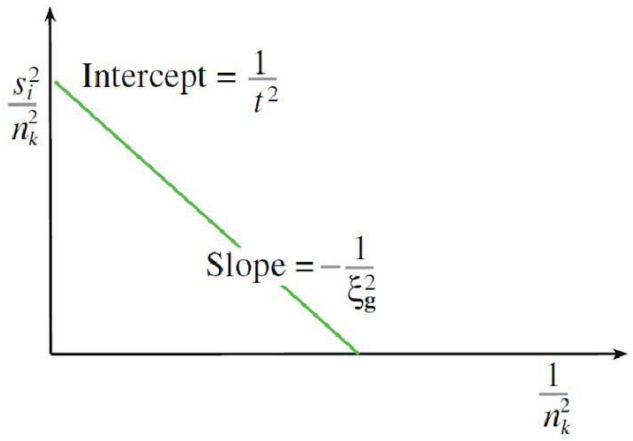

Figure 5.02 – An illustration of the $\left(\frac{s_i}{n_i}\right)^2$ against $\left(\frac{1}{n_i}\right)^2$ graph, from which the foil thickness can be found.

5.5 Focused Ion-Beam (FIB)

A Quanta 3D FEG focused ion-beam microscope was used to manufacture the micro sized sample for the Bauschinger tests, as well as the micro grip on the MEMS straining device.

Equipped with dual beams, this microscope has, in addition to the same capabilities as a normal SEM, with secondary and backscattered electron imaging, XRD for chemical composition and EBSD crystallography analysis, a focused ion-beam which can be used for milling and depositing material and an omniprobe to lift small specimens. The angle between the electron beam and the ion beam is 52°, whereas the stage allows 360° of rotation and 70° of tilting, resulting in great freedom of movement. Probe currents ranging from 10 pA to 65 nA can be used for ion-beam imaging and high volume milling.

5.6 Mechanical tests

An ESH Servo-hydraulic twin column ramp universal testing machine with a 200 kN load cell was used to perform the mechanical tests on macro samples

Samples for compression were produced using a precision table top cut-off Struers Accutom-5 machine. All samples had a square prism shape with a cross section of area of 15 mm^2 and 8 mm gauge length. Compression was carried out up to 1 % and 2 % plastic strain for each alloy at a strain rate of $1.6x10^{-4} s^{-1}$ and at room temperature.

Bauschinger test samples were machined into a 4.5 mm diameter and 13 mm gauge length, as illustrated in figure 5.03. The strain was measured by a Kyowa KFG series strain gauge fixed to the gauge length with CC-36 Kyowa Loctite Cement. These tests were also carried out up to 1 % compression + 1 % tension and 2 % compression + 2 % tension plastic strain for each alloy at a strain rate of $1.6x10^{-4}$ s^{-1} and at room temperature. The data output from the strain gauges was computed using an AC/DC converter and processed using Labview (v9.1) software.

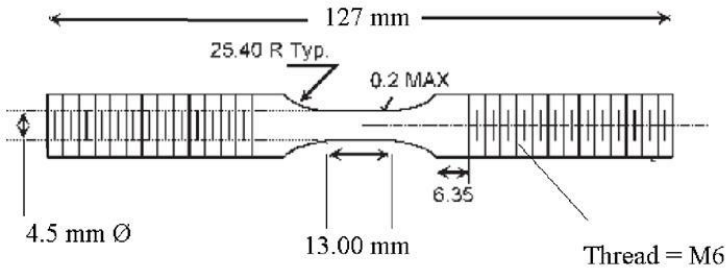

Figure 5.03 – An illustration of the dimensions of the Bauschinger test samples.

5.7 Micro Bauschinger tests

As mentioned in Section 4.4, part of the purpose of this project was to develop a device for small scale in-situ mechanical testing. Samples for the system created were produced from thin discs prepared similarly to the TEM specimens as previously described in Section 5.3.

From the edge of 50 µm thick 3 mm TEM discs, FIB milling at 50 nA was performed to thin the walls of the disc, creating a 15 µm thick plate. Then the current was lowered to 30 nA to create a smoother surface. This plate is then tilted 90° so that a dog bone shaped sample could be milled using a current of 7 nA. At this point the specimen is separated from the disc and transferred to the MEMS straining device using the omniprobe. The gauge length was then thinned down to its desired dimensions and a

final polishing of the gauge length surface was done using a current of 3 nA, removing any defects or scratches from the surface, as shown in figure 5.04. Three cross sections of areas of 15, 30 and 50 µm² were chosen for each alloy, with a gauge length of 20 µm. Using this MEMS straining device, the plastic strain was limited to 1% compression and 1% tension.

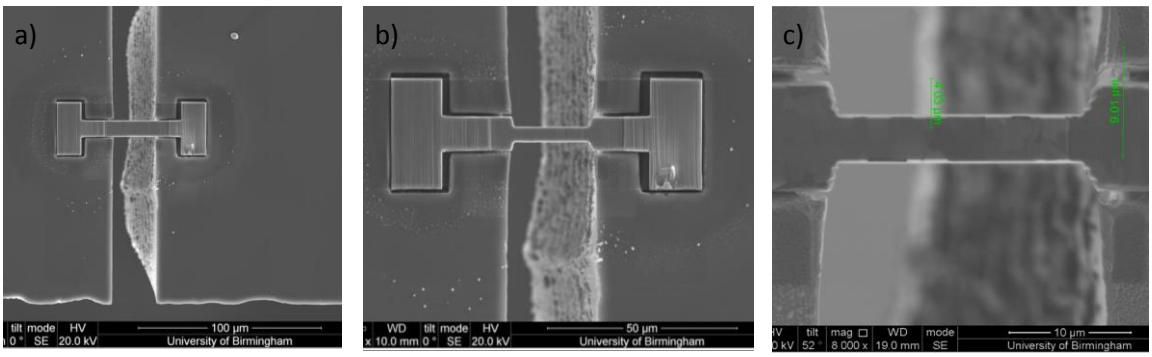

Figure 5.04 – a) Sample sitting on the grips of the MEMS straining device, b) gauge length milled to the desired dimensions and c) gauge length polished and ready for testing.

During the micro Bauschinger test, the force sensor deflection and the displacement of the sample were measured using the length measurement feature on the microscope. However, a picture of 2048 x 1886 pixels resolution was taken from the gauge length after every straining and analysed after the test using ZEISS Axiovision. Using this technique, the strain was measured with a resolution of 1.215×10^{-2} µm.

The force was calculated from the force sensor beam dimensions, as mentioned in chapter 4.4. For other applications, a calibration of the force may be required, but since the Bauschinger stress parameters are relative, calibration is unnecessary here.

6 RESULTS

6.1 X70 alloy

6.1.1 Thermodynamic simulation

The Ar_3 ($\gamma \rightarrow \alpha + \gamma$) and Ar_1 ($\alpha + \gamma \rightarrow \alpha$) temperatures as well as the volume fraction of precipitates, austenite and cementite expected to be present in the X70 alloy were determined using Thermo-Calc. The phase evolution according to the temperature diagram is shown in figure 6.01, where the BCC phases (δ and α) and FCC phase (γ) are represented by the red and green lines respectively. From this graph, Ar_3 and Ar_1 are determined as 849°C and 666°C.

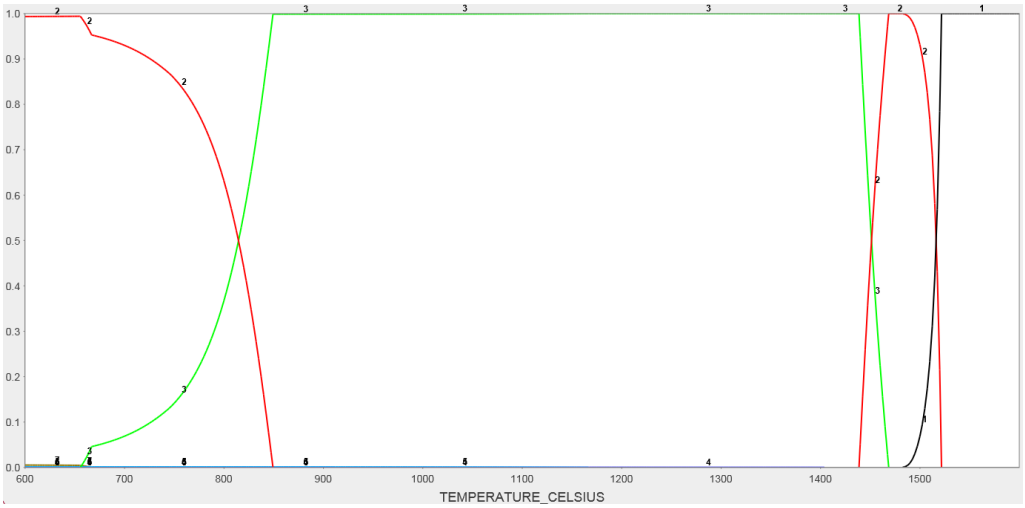

Figure 6.01 – Thermo-Calc prediction graph of phase evolution according to temperature of the X70 alloy. The BBC α and δ phases are in red on the left and right, respectively, of the above graph. The FCC γ phase is in green.

Additionally, at 600°C, Thermo-Calc has shown that there is no austenite present, the volume fraction of cementite is 0.39% and the combined volume fraction of precipitates is negligibly low at 0.0010

6.1.2 Microstructure of X70 as-received

Typical micrographs of the X70 as-received alloy are shown in figures 6.02 and 6.03. The material presents a very fine grain structure, consisting mostly of polygonal grains of ferrite. Distinctive areas of coarse ferrite grains can also be observed, as highlighted in figure 6.03. The mean grain size of the X70 as-received alloy, determined using the linear intercept technique, is 2.8 μm.

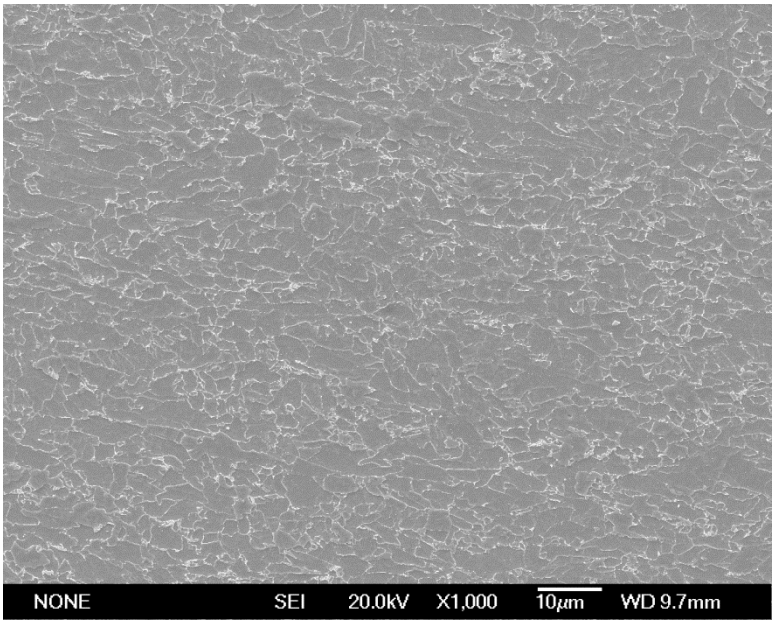

Figure 6.02 – SEM micrograph of the X70 as-received alloy.

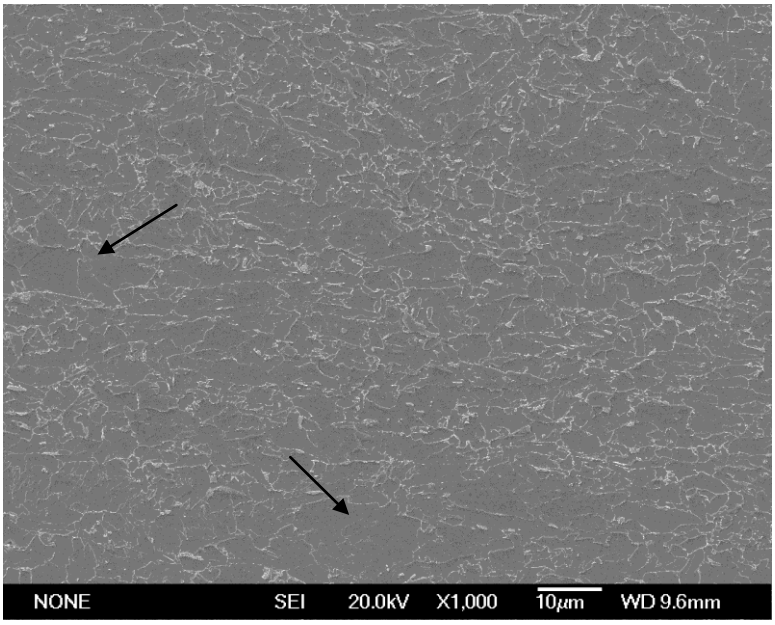

Figure 6.03 – SEM micrograph of the X70 as-received alloy. Areas of coarse ferrite grains are highlighted.

A pearlitic microstructure can also be observed, as shown in figures 6.04 and 6.05. However, it is found much less frequently. The area fraction of pearlite measured in the as-received X70 is 3.1%. Figure 6.05 shows a high magnification image of the pearlite, characterised by te alternating layers of ferrite (dark) and cementite (bright).

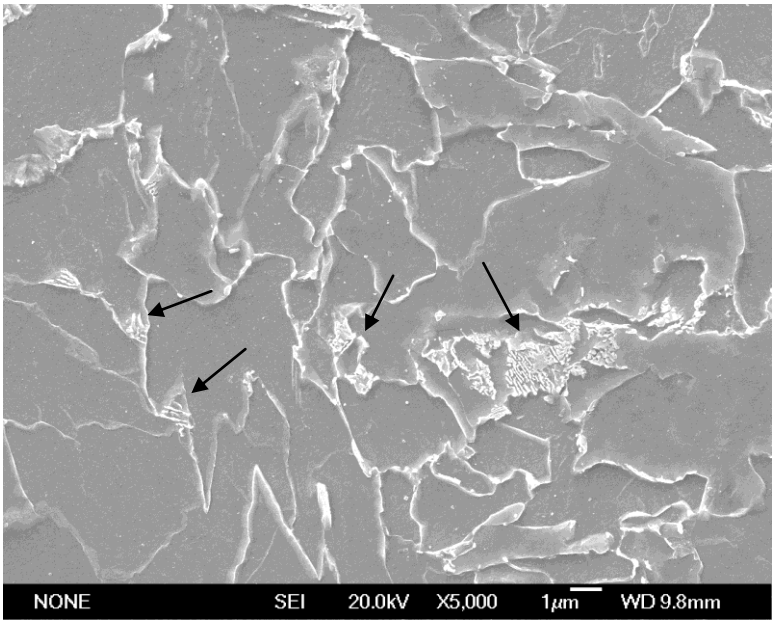

Figure 6.04 – SEM micrograph of the X70 as-received alloy showing small zones of pearlite within the ferritic microstructure.

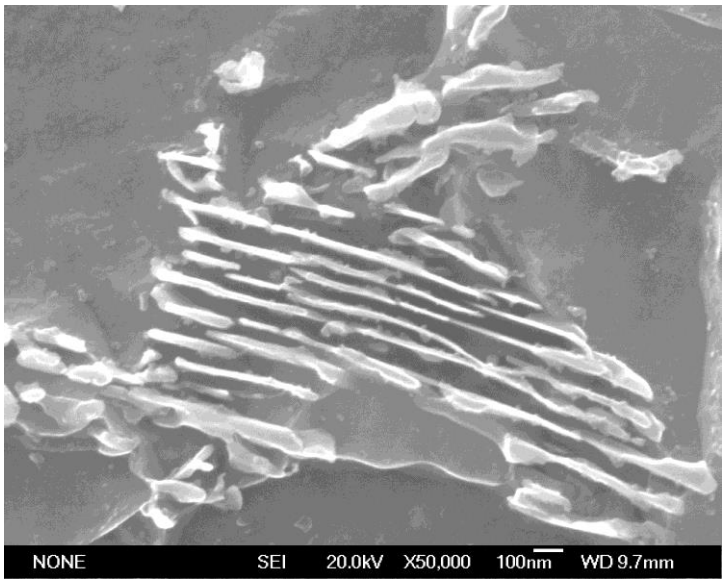

Figure 6.05 – SEM micrograph of the pearlite in the X70 as-received alloy.

Precipitates were identified by their shape and chemical composition. The two distinct precipitates found using SEM were (Nb,Ti) rich particles and Nb rich particles respectively, both predominantly located within the ferrite grains.

The (Nb,Ti) rich particles were square shaped, with size ranging from 50 to 170 nm, as shown in figure 6.06 a). The average width of the (Nb,Ti) rich particles was 79 nm with a volume fraction of 0.000273. An EDX spectrum of a (Nb,Ti) rich particle is shown in figure 6.06 b), along with an EDX spectrum of the ferritic matrix in c).

a)

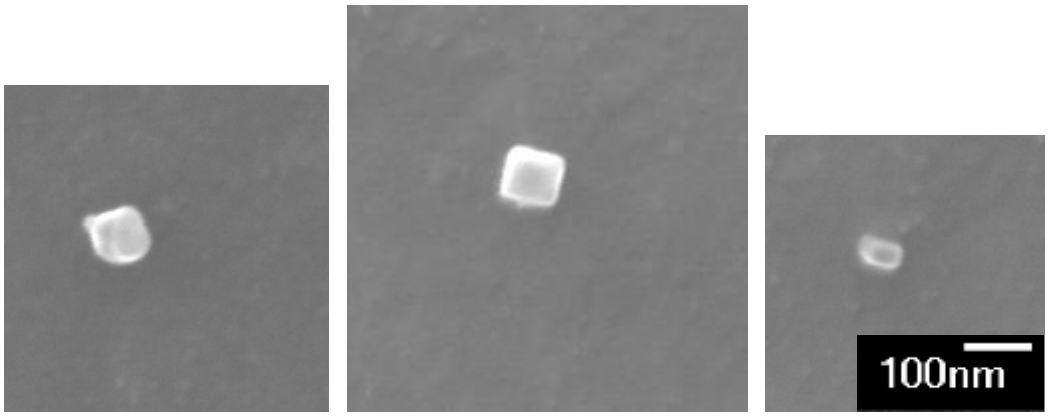

b)

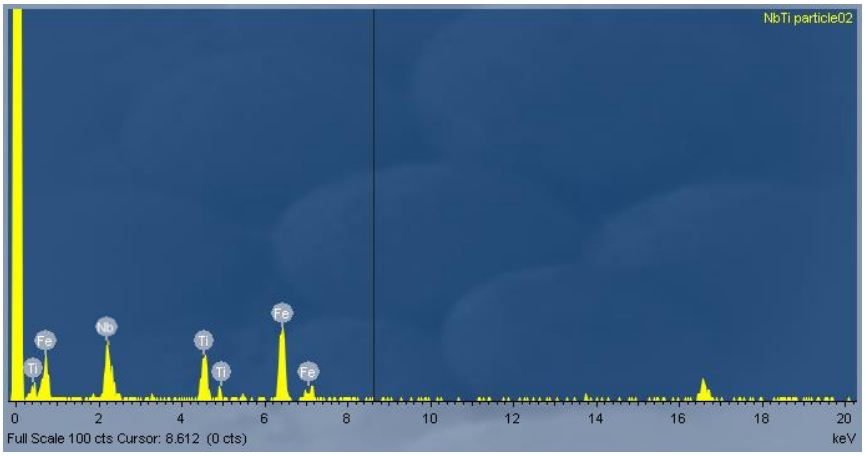

c)

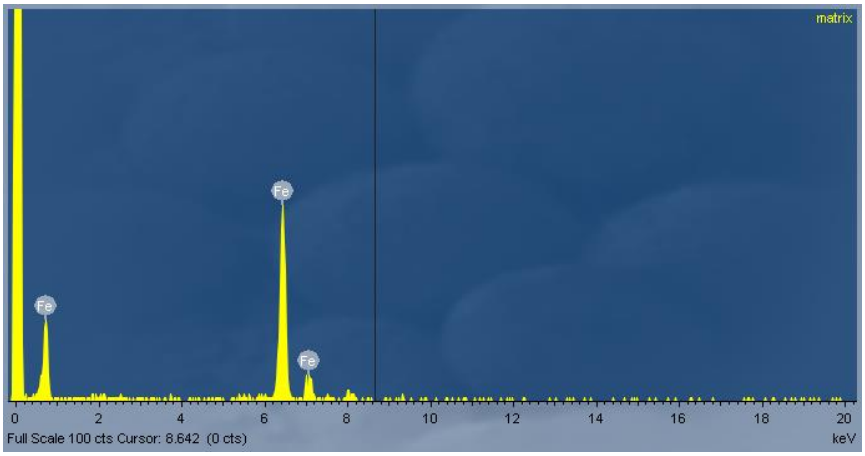

Figure 6.06 – a) SEM micrographs showing the typical shape and size of the (Nb,Ti) rich precipitates present in the X70 as-received alloy; b) EDX spectrum of a (Nb,Ti) rich precipitate; and c) EDX spectrum of the ferritic matrix.

The second type of precipitate found in the X70 as-received alloy was Nb rich. Compared to the (Nb,Ti) rich particles, these precipitates have a spherical morphology, are smaller and are present at higher density, albeit with a smaller volume fraction. The width of the Nb rich particles ranges from 20 to 55 nm with an average of 36nm, whereas their volume fraction is 0.000162%.

Figure 6.07 a) shows typical Nb rich particles found in the X70 as-received alloy along with an EDX spectrum in b).

a)

b)

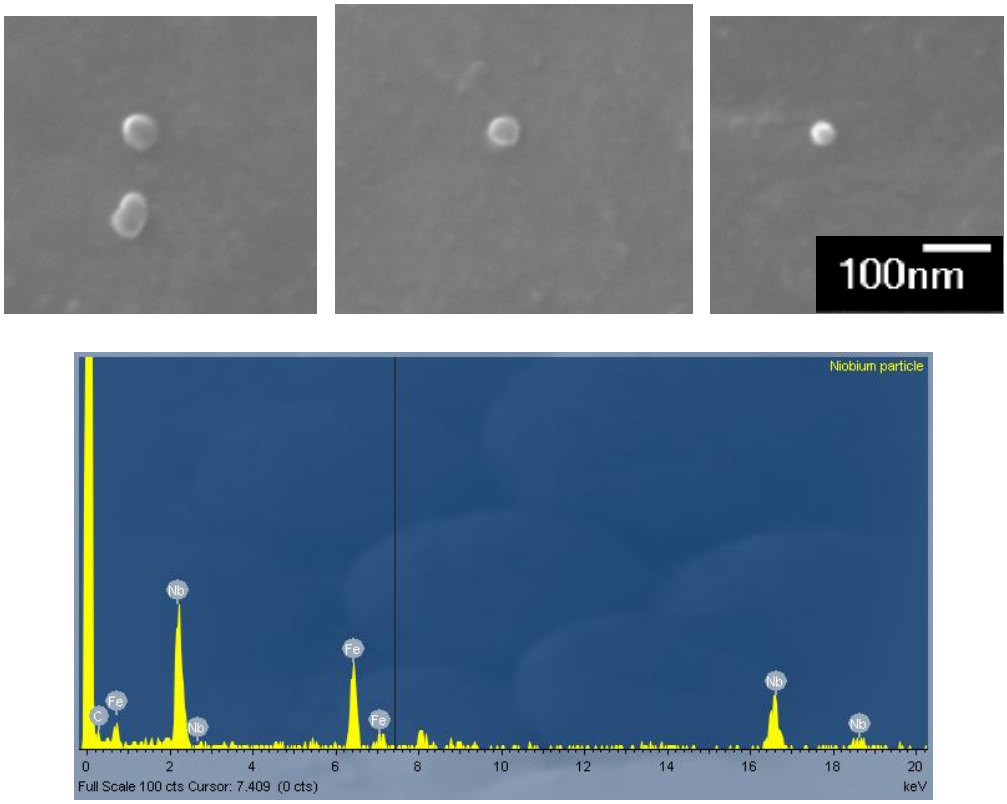

Figure 6.07 – a) SEM micrograph showing the typical morphology and size of the Nb rich particles; b) EDX spectrum of a Nb rich precipitate.

Precipitates containing vanadium were not found using the SEM. Particles of this type are typically very small, with sizes ranging from 2 to 10 nm and are therefore difficult to detect by SEM. However, TEM analysis was not able to detect the presence of V rich particles either.

A typical dislocation microstructure for the X70 as-received alloy under two beam condition is shown in the montage of micrographs of a whole grain in figure 6.08 and figure 6.09. The dislocations are homogeneously dispersed with little evidence of

dislocation-particle interaction. Furthermore, the dislocation microstructure and density are homogeneous under different two beam conditions. Thus all types of dislocations are homogeneously distributed. The average dislocation density of the X70 as-received alloy is 7.872×10^{13} m^{-2}.

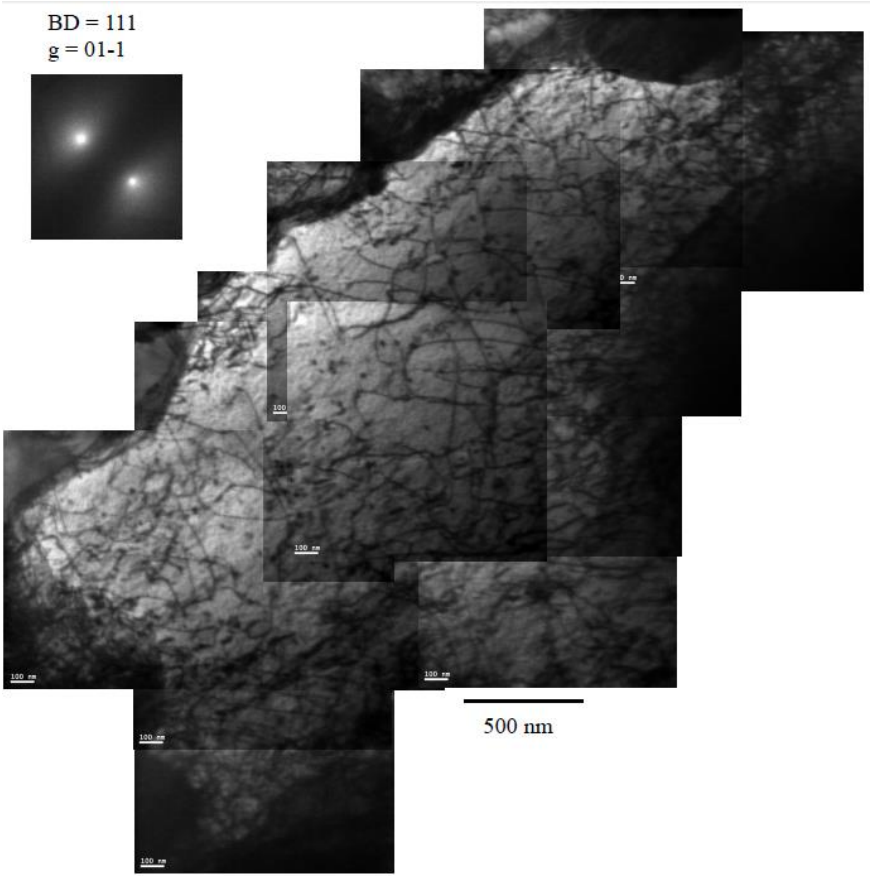

Figure 6.08 – Bright field TEM micrograph of the X70 as-received alloy.

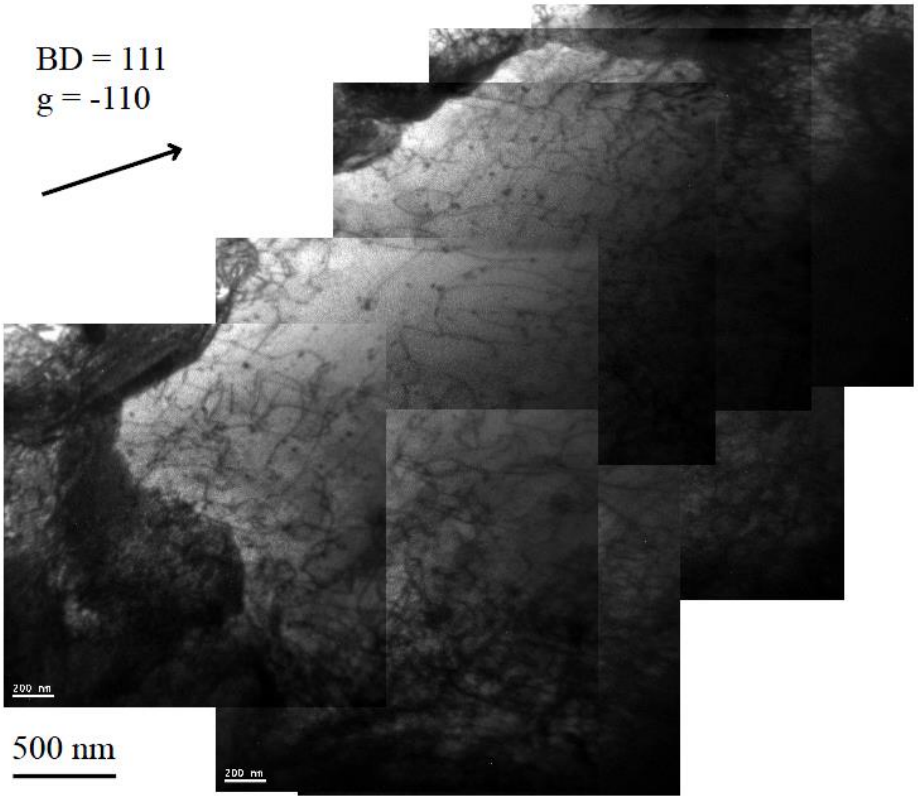

Figure 6.09 – Bright field TEM micrograph of the same grain of the X70 as-received alloy as in figure6.09, under a different two beam condition.

In addition, there are small areas where tangles or clusters are starting to occur, as highlighted by the white box in figure 6.10.

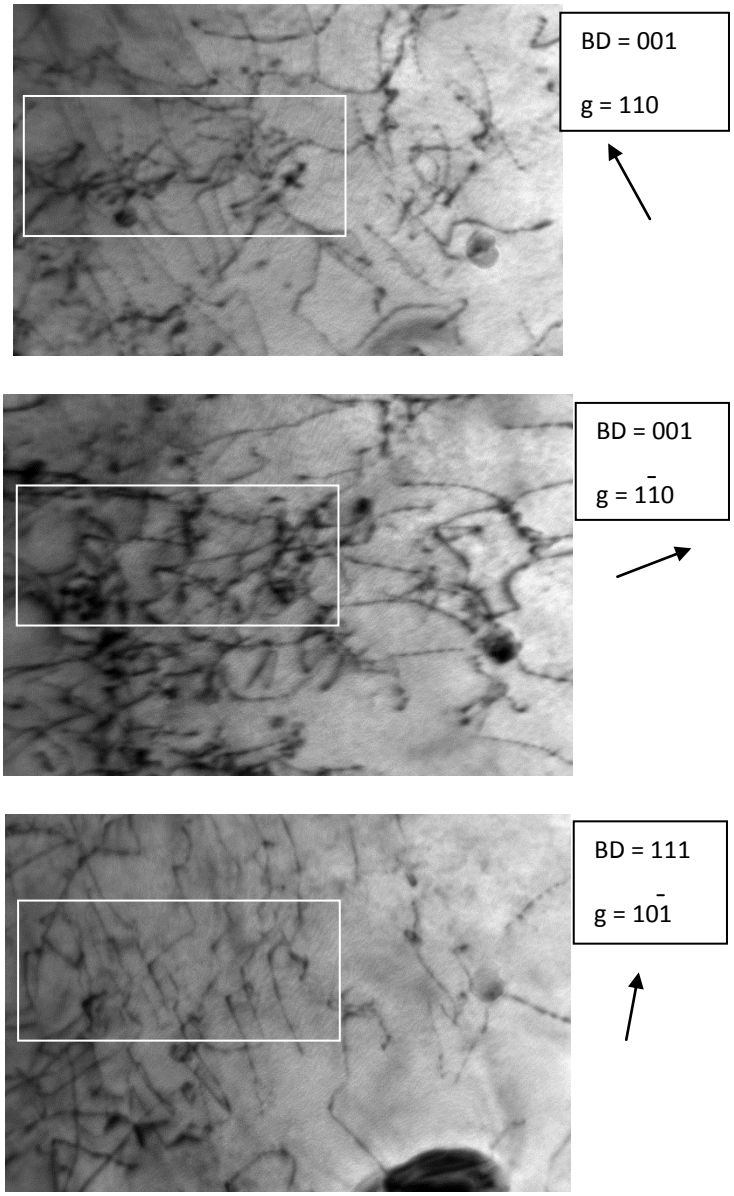

Figure 6.10 – Bright field TEM micrographs of a cluster of dislocations under different two beam conditions.

6.1.3 Compression tests

Compression tests were carried out on the X70 as-received alloy in order to reproduce the first step of the Bauschinger test. The samples were tested up to 1 and 2% plastic strain, so that a direct comparison of the effect of pre-strain on the Bauschinger parameters could be made. Figure 6.11 shows the 2% (plastic deformation) compression curve of the X70 alloy.

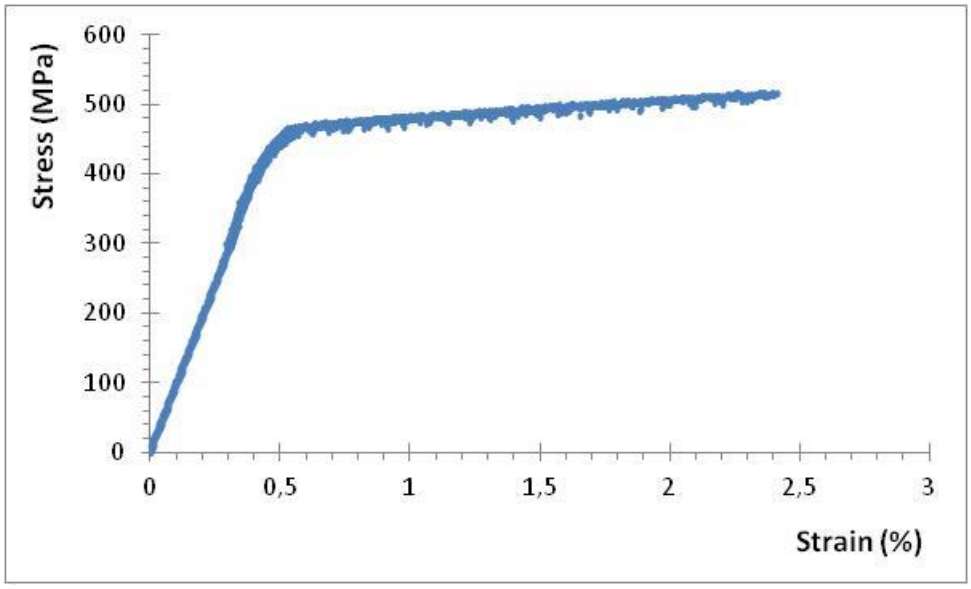

Figure 6.11 – Stress-strain curve of the compression test on the X70 alloy after 2% plastic strain.

The TEM analysis of the compressed samples showed an increase in dislocation-dislocation interactions and an increase in the dislocation density to 2.186 x10^{14} m^{-2}.

In addition, the initial dislocation clusters present in the as-received material have further expanded and developed into dislocation walls, as well as starting to form dislocation cells. The dislocation structure after compression is no longer homogeneously dispersed, as there is a higher dislocation concentration within the walls and lower density within the dislocation cells.

However, this dislocation structure and density remain homogeneous across the different types of dislocations. Figures 6.12, 6.13 and 6.14 show a montage of bright-field micrographs of a grain of the X70 alloys after 2% compression under three different two beam conditions.

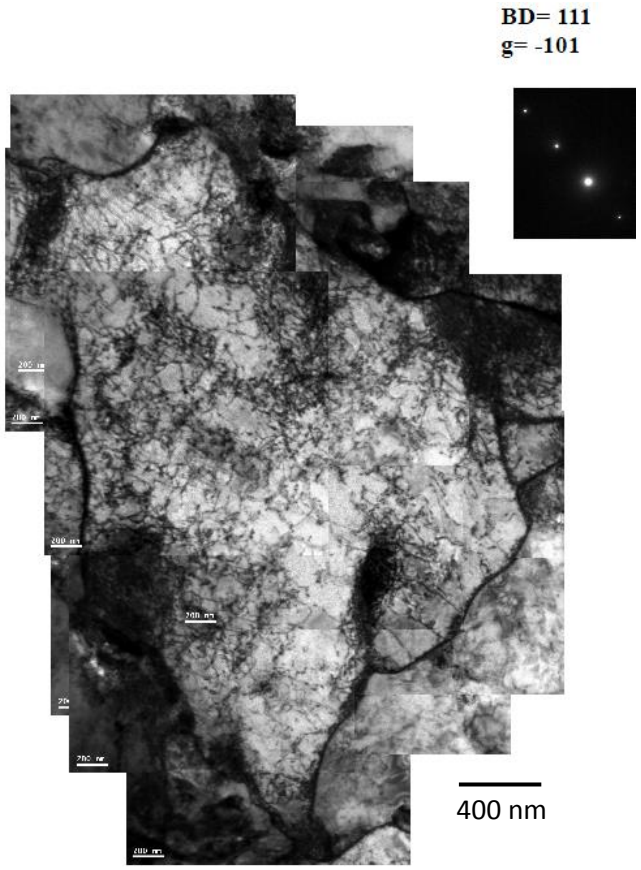

Figure 6.12 – Bright-field TEM micrographs montage showing the dislocation structure of the X70 alloy after 2 % compression under two-beam condition.

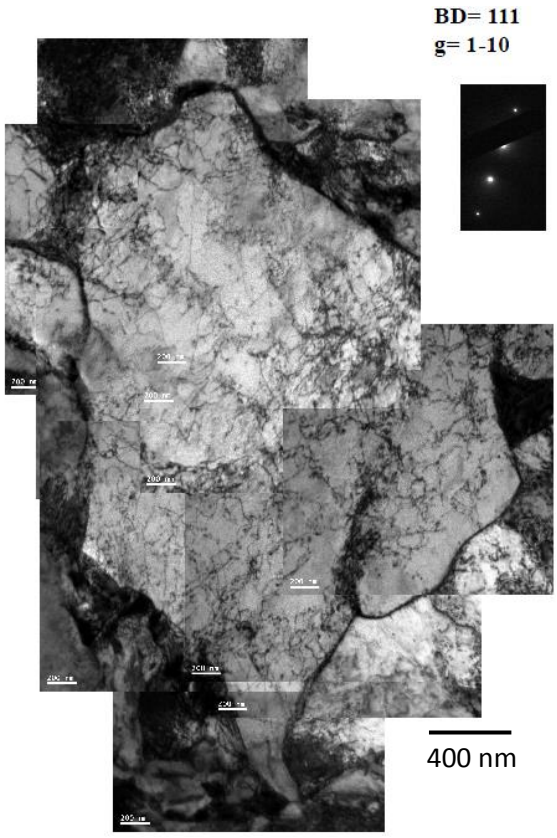

Figure 6.13 – Bright-field TEM micrographs montage showing the dislocation structure of the X70 alloy after 2 % compression under two-beam condition.

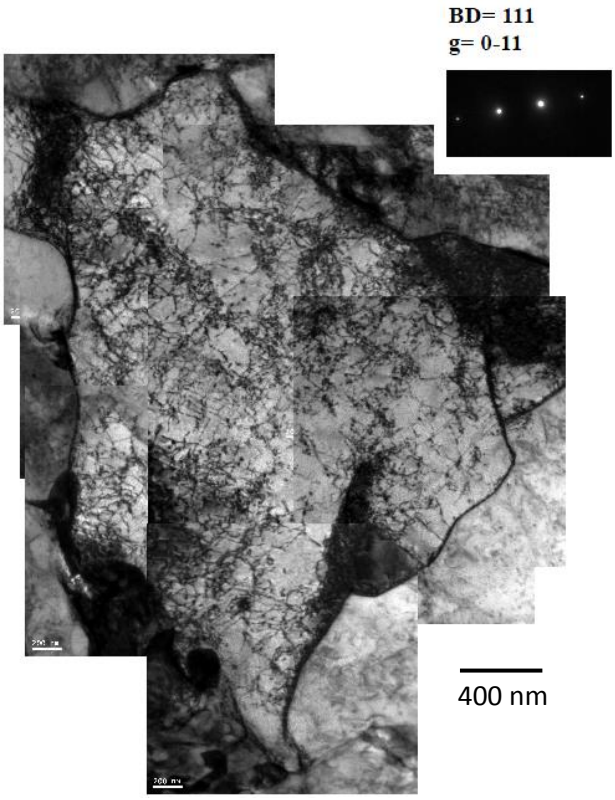

Figure 6.14 – Bright-field TEM micrograph montage showing the dislocation structure of the X70 alloy after 2 % compression under two-beam condition.

6.1.4 Macro Bauschinger tests

The stress-strain curves of the Bauschinger tests carried out on samples of 3.5 mm in diameter and 13 mm gauge length are shown in figure 6.15 and figure 6.16 shows the positions of the values used to calculate the Bauschinger parameters in the Bauschinger curve.

a)

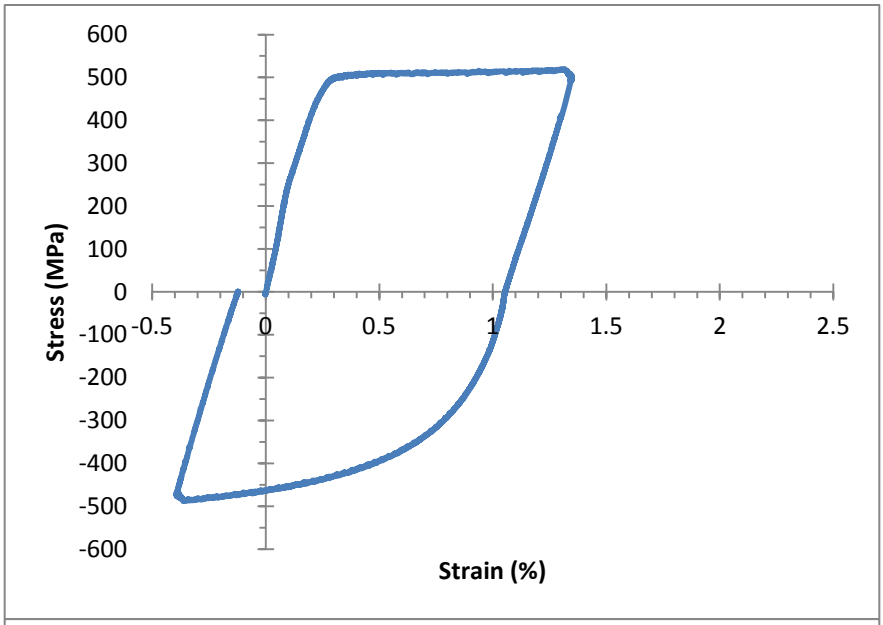

b)

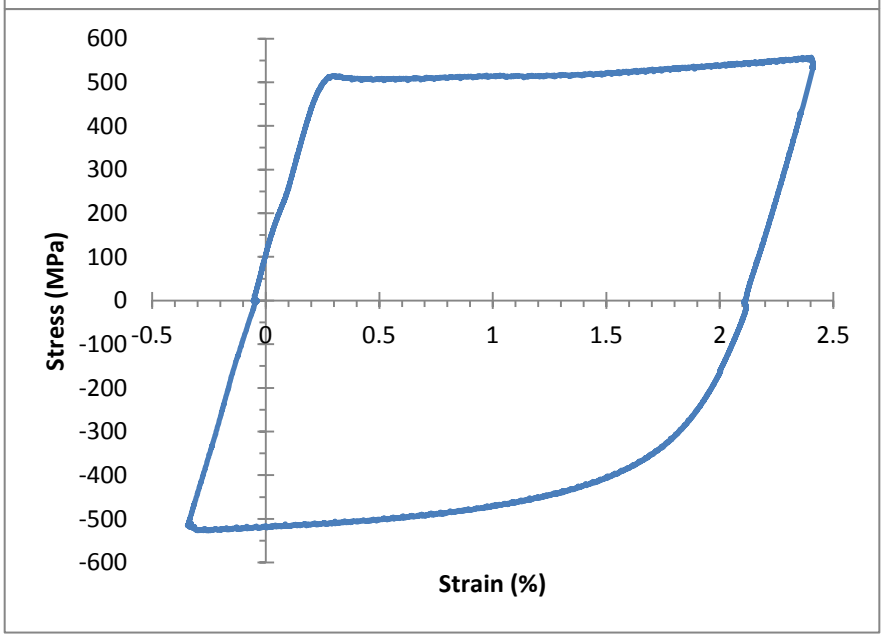

Figure 6.15 – The stress-strain Bauschinger curve up to a) 1% and b) 2% plastic deformation.

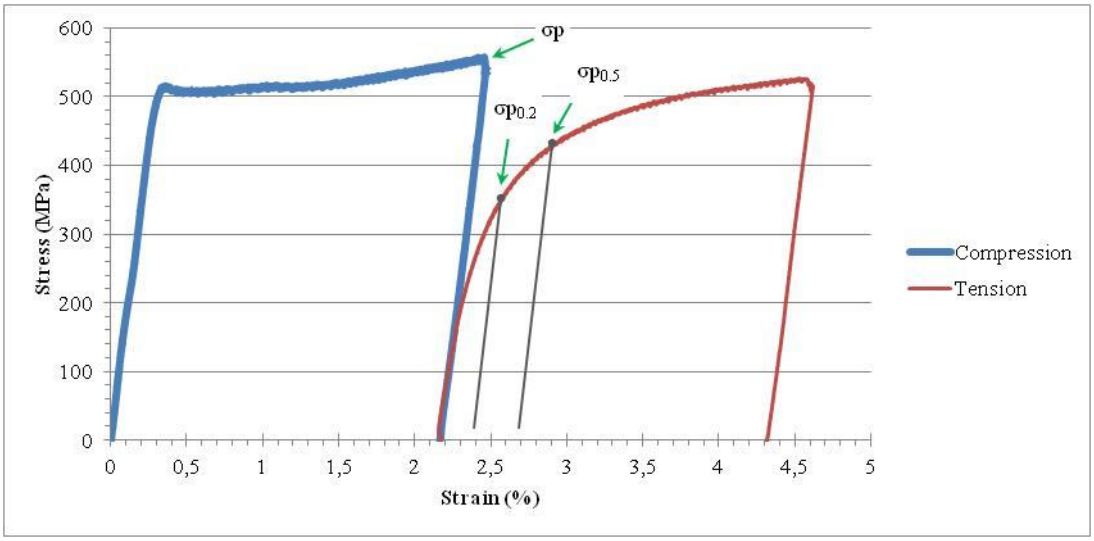

Figure 6.16 – Bauschinger curve up to 2% strain showing the positions of the values used to calculate the Bauschinger parameters.

For the 1% Bauschinger test, the value of maximum stress (σ_p) in compression was 520 MPa and 557.5 MPa for the 2% Bauschinger test. For both 1 and 2% Bauschinger tests, the values of stress at 0.2 ($\sigma_{r0.2}$) and 0.5% ($\sigma_{r0.5}$) tension strain were 350 and 425 MPa. With these values, the Bauschinger parameters $\beta\sigma_{0.2}$ and $\beta\sigma_{0.5}$ were 0.33 and 0.18 for the 1% Bauschinger test and 0.37 and 0.24 for the 2% Bauschinger test. A summary of these results is shown in table 6.1.

Table 6.1 – Bauschinger parameters for the X70 alloy after 1 and 2% tests.

Plastic strain	σ_p (MPa)	$\sigma_{r0.2}$ (MPa)	**$\beta\sigma_{0.2}$**	$\sigma_{r0.5}$ (MPa)	**$\beta\sigma_{0.5}$**
1%	520	350	**0.33**	425	**0.18**
2%	557	350	**0.37**	425	**0.24**

The dislocation analysis of the X70 alloy after the 2% Bauschinger test revealed a fully developed dislocation cell structure where most of the cells presented a dislocation-free core. The dislocation density after the Bauschinger test has remained similar to after compression at 2.019 $x10^{14}$ m^{-2}. Figures 6.17, 6.18 and 6.19 show a montage of bright-field micrographs of the X70 alloy after 2% Bauschinger test under different two beam conditions.

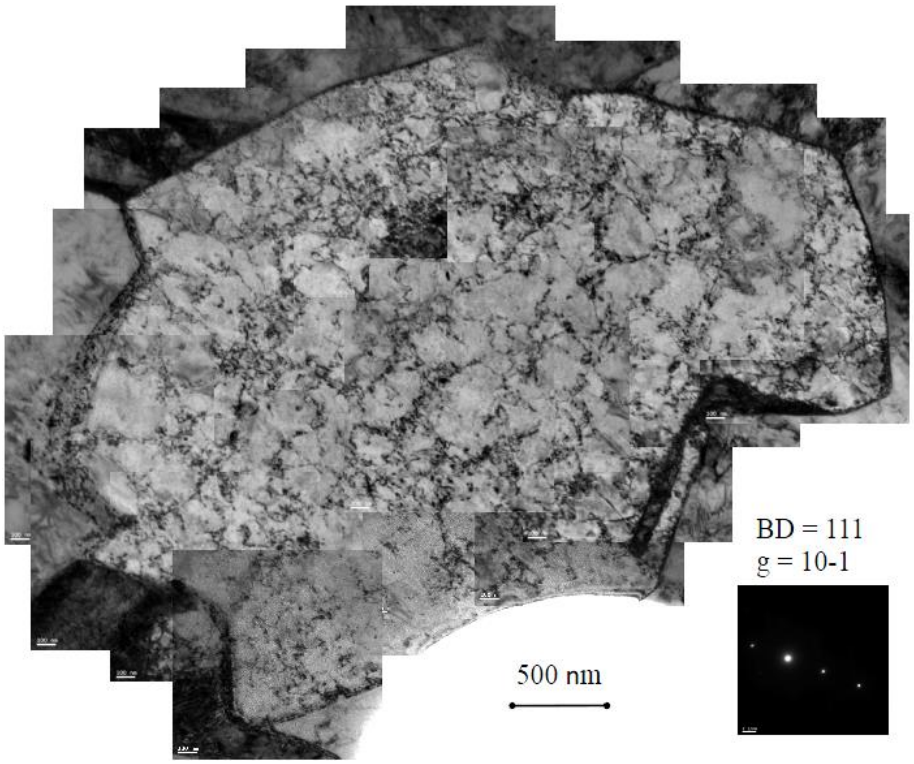

Figure 6.17 – Bright-field TEM micrographs montage showing the dislocation structure of the X70 alloy after 2 % Bauschinger test under different two beam conditions.

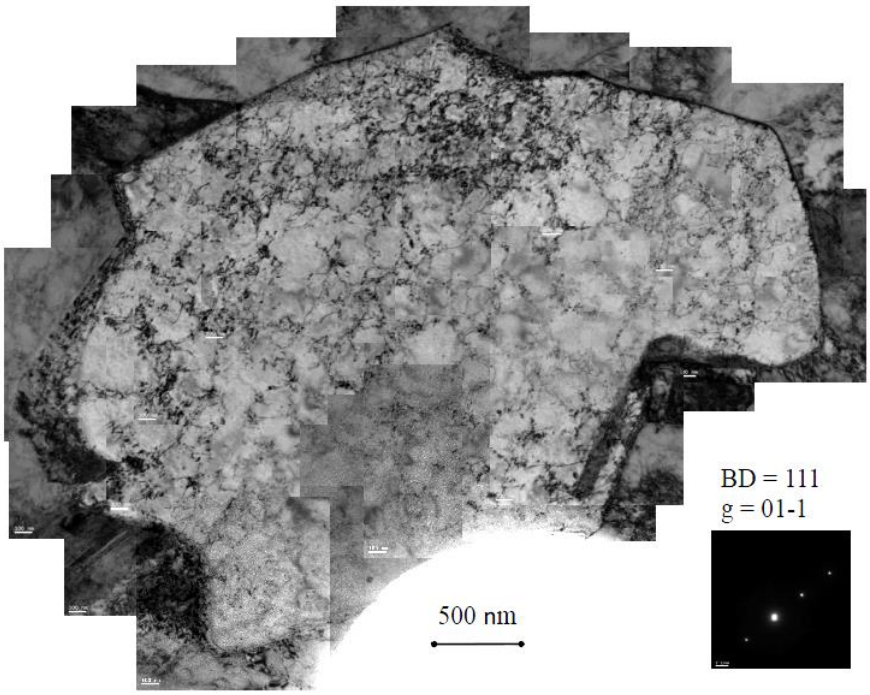

Figure 6.18 – Bright-field TEM micrographs montage showing the dislocation structure of the X70 alloy after 2 % Bauschinger test under different two beam conditions.

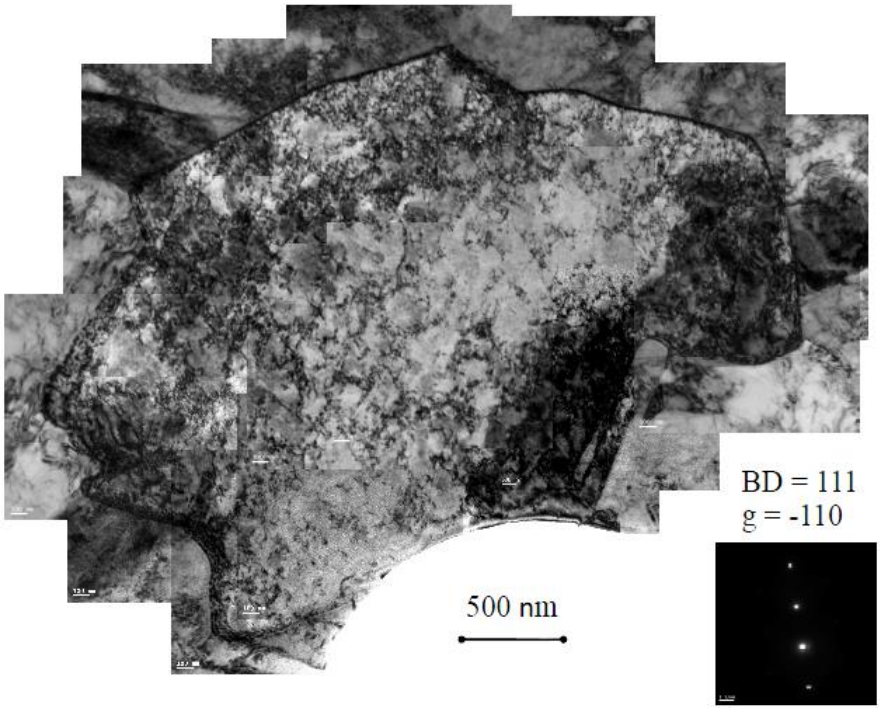

Figure 6.19 – Bright-field TEM micrographs montage showing the dislocation structure of the X70 alloy after 2 % Bauschinger test under different two beam conditions.

6.1.5 In-situ Bauschinger tests

The Bauschinger test was also carried out on micro sized samples. The cross-section area of the X70 alloy test samples were 52.57, 30.86 and 16.12 µm² and they were tested up to 1% pre-strain (compression) followed by 1% reverse strain (tension).

Preliminary compression tests carried out during the development of the microelectromechanical straining system used in this project has shown good repeatability and uniformity in its results for samples of similar dimensions and microstructure.

These results are shown in figure 6.20, with improvements made to the testing schedule from test 1 to test 4. Testing schedule used in test 4 was then applied to all the micro Bauschinger tests presented in this research.

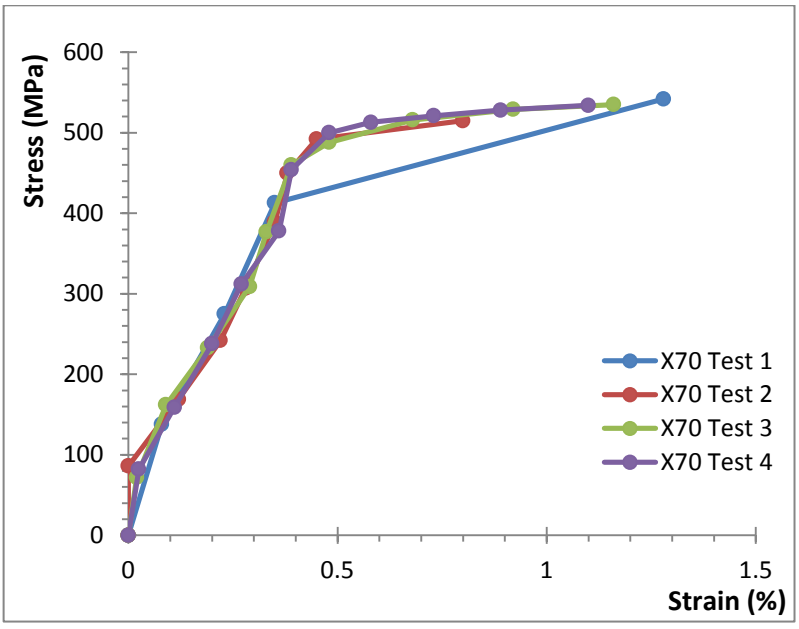

Figure 6.20 – Compression tests during the development of the microelectromechanical device and testing schedules.

For the 52.57 µm² sample, the maximum stress value (σp) in compression was 541 MPa, the stress value at 0.2% strain in tension was 365 MPa and at 0.5% strain in tension was 448 MPa. Thus the Bauschinger parameters βσ0.2 and βσ0.5 were 0.32 and 0.17 respectively. The curve of the Bauschinger test for this sample is shown in figure 6.21.

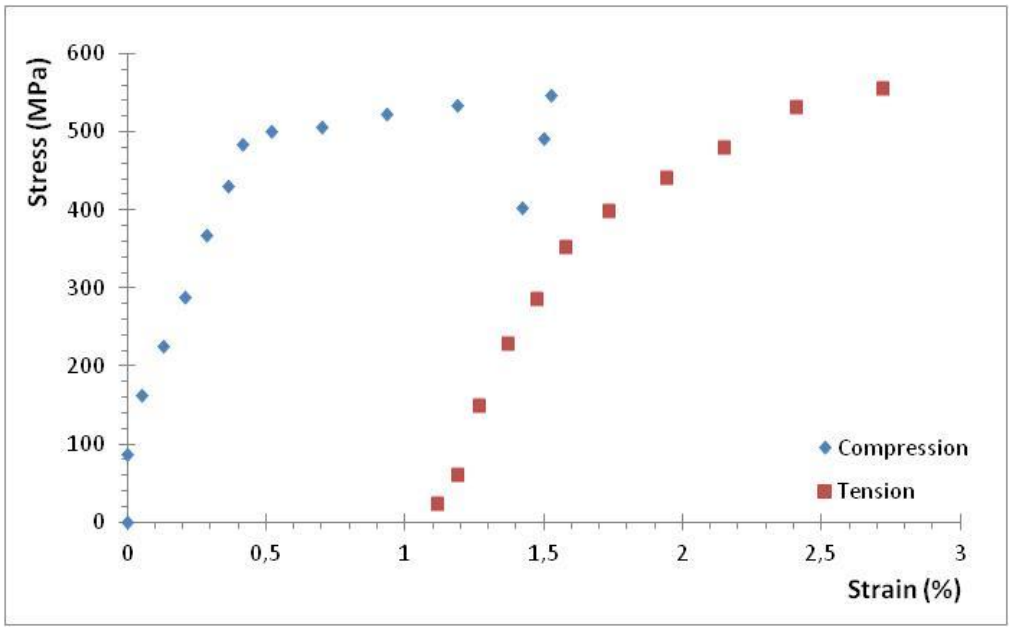

Figure 6.21 – In-situ Bauschinger test curve of the X70 alloy sample of 52.57 µm² cross-section area.

For the 30.86 µm² sample, the maximum stress value (σp) in compression was 560 MPa, the stress value at 0.2% strain in tension was 385 MPa and at 0.5% strain in tension was 465 MPa. Thus the Bauschinger parameters βσ0.2 and βσ0.5 were 0.31

and 0.17 respectively. The curve of the Bauschinger test for this sample is shown in figure 6.22.

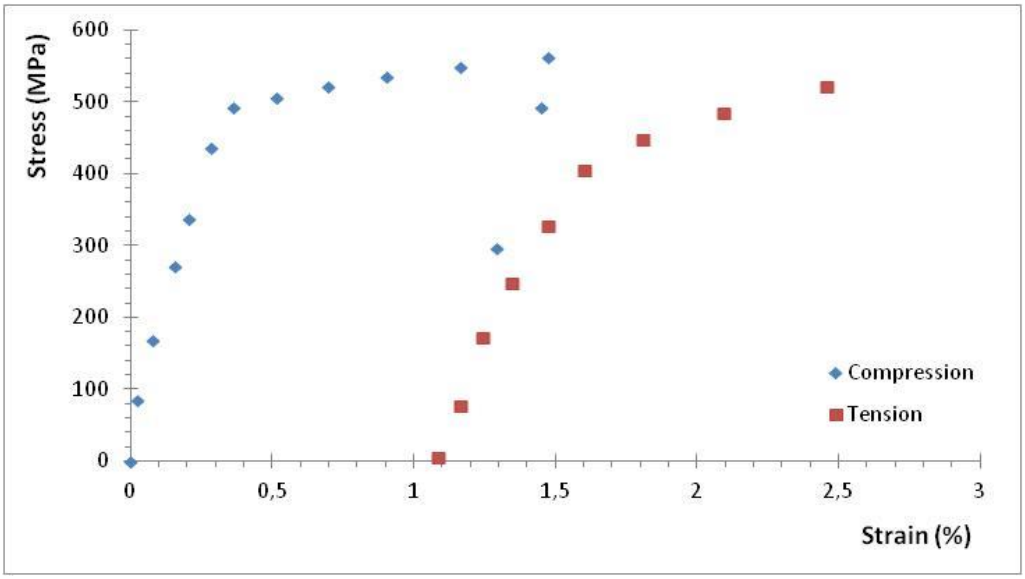

Figure 6.22 – In-situ Bauschinger test curve of the X70 alloy sample of 30.86 μm² cross-section area.

Finally, for the 16.12 μm² sample, the maximum stress value (σp) in compression was 558 MPa, the stress value at 0.2% strain in tension was 378 MPa and at 0.5% strain in tension was 460 MPa. Thus the Bauschinger parameters βσ0.2 and βσ0.5 were 0.32 and 0.18 respectively. The curve of the Bauschinger test for this sample is shown in figure 6.23.

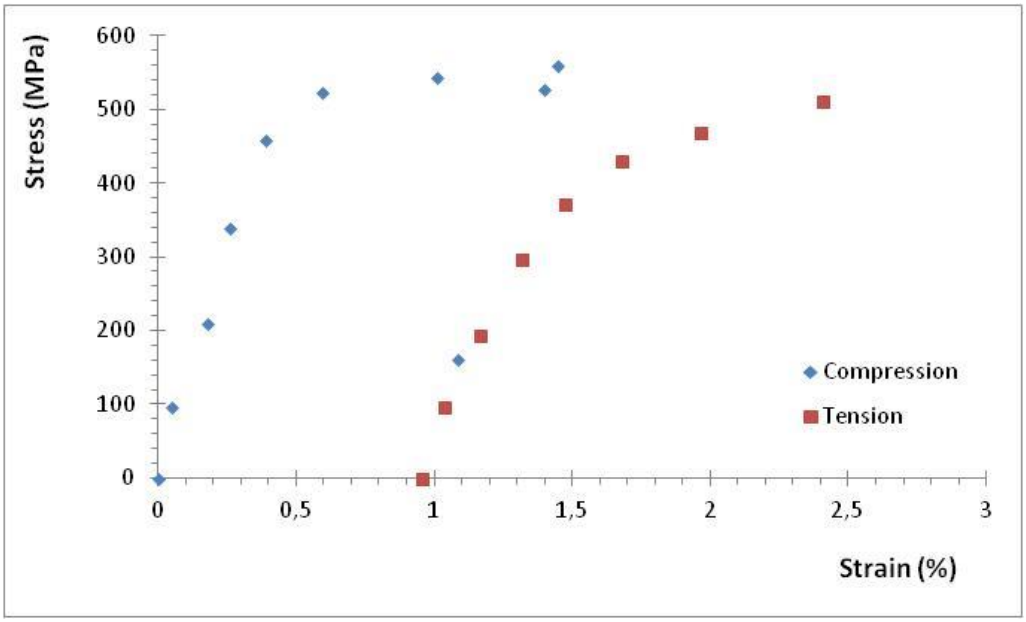

Figure 6.23 – In-situ Bauschinger test curve of the X70 alloys sample of 16.12 µm² cross-section area.

Results for the X70 alloy show that the Bauschinger parameter is the same for all the different sizes used, as well as when compared to the macro Bauschinger tested samples, as presented in table 6.2 below.

Table 6.2 – micro Bauschinger parameters for the X70 alloy.

Cross-section	σ_p (MPa)	$\sigma_{r0.2}$ (MPa)	$\beta\sigma_{0.2}$	$\sigma_{r0.5}$ (MPa)	$\beta\sigma_{0.5}$
52.57 µm²	541	365	**0.32**	448	**0.17**
30.86 µm²	560	385	**0.31**	465	**0.17**
16.12 µm²	558	378	**0.32**	460	**0.18**

6.2 X80 alloy

6.2.1 Thermodynamic simulation

Thermo-Calc simulation of the phases present at different temperatures for the X80 alloy is shown in figure 6.24, where the BCC phases (δ and α) are represented in red and brown lines and the FCC phase (γ) is represented by the green line. The Ar_3 and Ar_1 temperatures for the X80 alloy are predicted to be 815°C and 647°C respectively.

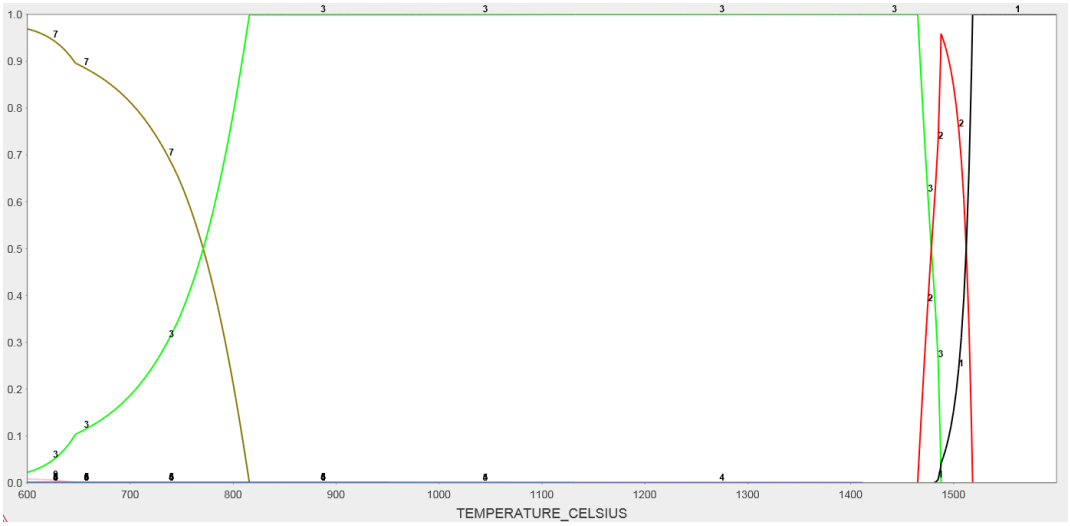

Figure 6.24 – Thermo-Calc prediction graph of phase evolution according to temperature of the X80 alloy. Brown: α; Red: δ phase; Green: γ.

Additionally, at 600°C, Thermo-Calc has shown that the volume fraction of austenite is 2.19%, cementite is 0.65% and the combined volume fraction of precipitates is very low at 0.0005.

6.2.2 Microstructure of X80 as-received

In contrast to the X70 as-received alloy, the microstructure of the X80 alloy consists predominantly of granular bainite, formed by fine irregular ferrite grains with an average grain size of 1.9 µm, discontinuously separated by small islands of retained austenite and small cementite particles. In addition, small areas of upper bainite are present, where narrow elongated ferrite grains are separated by thin laths of retained austenite. A typical SEM image of the X80 as-received alloy is shown in figure 6.25 where the dark areas are the bainitic ferrite grains and the intergranular white areas are the austenite islands/laths.

However, due to the complexity of the structure, the SEM images seem heavily textured and resemble a fracture surface and increasing the amount of white contrast. Thus identifying and quantifying the small features is therefore difficult using this technique, as shown in figure 6.26.

Similarly to the X70 as-received alloy, the as-received X80 presents the same types of precipitates, also located within grains. However, the average width of the (Nb,Ti) rich particles is 71 nm with a volume fraction of 0.0000728, whereas the average width of the Nb rich particles is 35 nm with a volume fraction of 0.0000439.

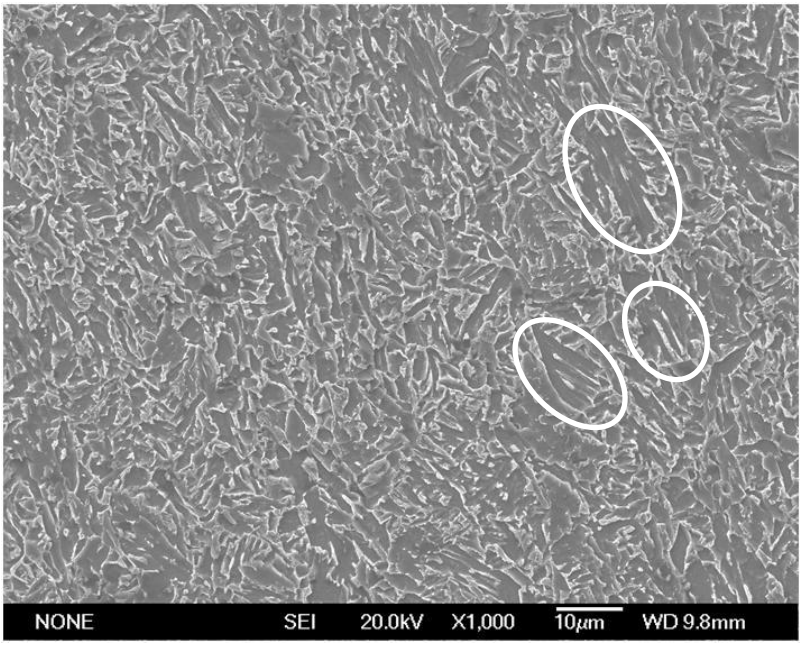

Figure 6.25 – SEM micrograph showing the general X80 microstructure. The highlighted ellipses are areas of upper bainite.

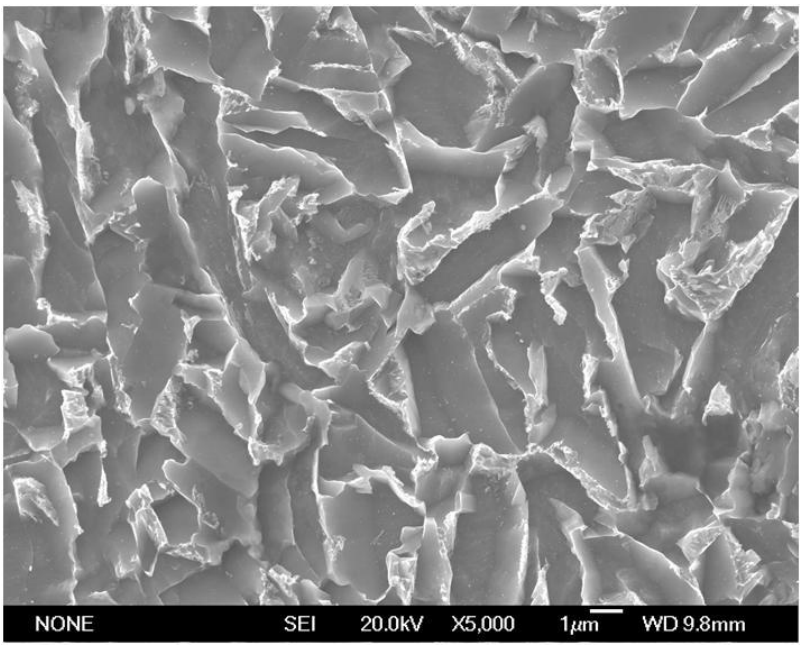

Figure 6.26 – SEM micrographs showing the textured white areas.

In contrast to SEM, which shows a large amount of white area in between grains of ferrite, the TEM analysis of the as-received X80 alloy shows less intergranular space, as shown in figure 6.27.

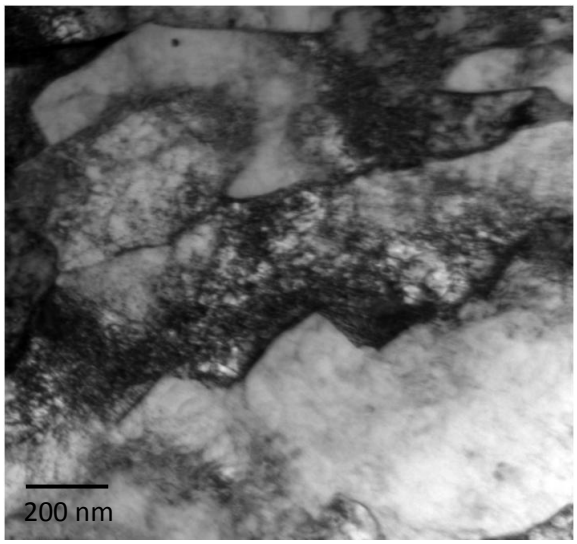

Figure 6.27 – A typical TEM micrograph of the X80 as-received alloy microstructure.

TEM analysis also shows more clearly the retained austenite islands and the cementite particles, as shown in figure 6.28, so that they can be more easily quantified. The retained austenite is present in the form of elongated islands of around 1 µm and also as very thin laths of 10 to 20 nm across, both between grains of bainitic ferrite. The total volume fraction of the retained austenite is 2.74%. The cementite particles present a pebble like shape of 45 nm average width and 0.132% volume fraction, and are located at grain boundaries alongside the retained austenite.

a)

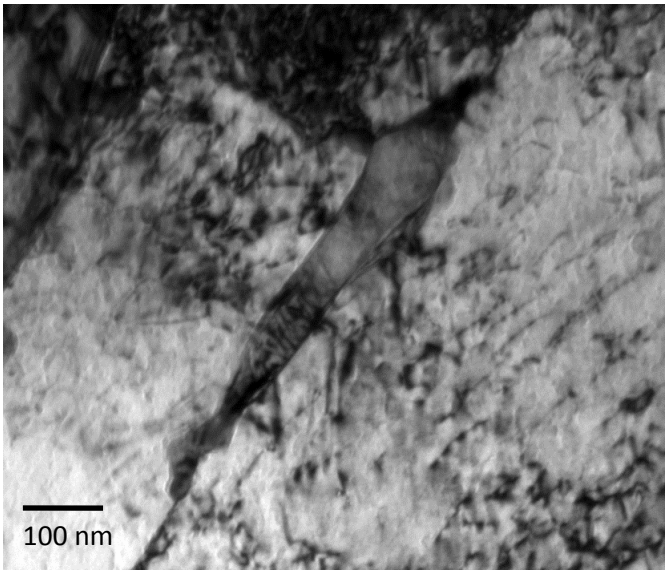

b)

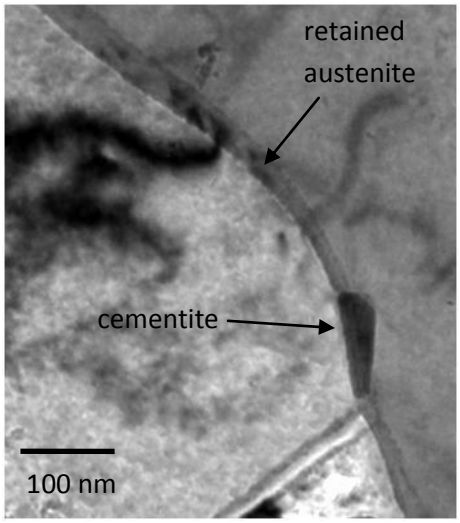

Figure 6.28 – Two TEM micrographs of the X80 as-received alloy showing a) a retained austenite island within two grains of ferrite and b) a thin layer of retained austenite and a cementite particle within ferrite grain boundaries.

Dislocations in the X80 as-received alloy present a non uniform structure, predominantly arranged in clusters as in the early stages of a cellular structure.

However, this dislocation structure is homogeneous for all types of dislocations. The average dislocation density of the X80 as-received alloy is 4.835 $x10^{14}$ m^{-2}. A typical dislocation structure is shown in figure 6.29.

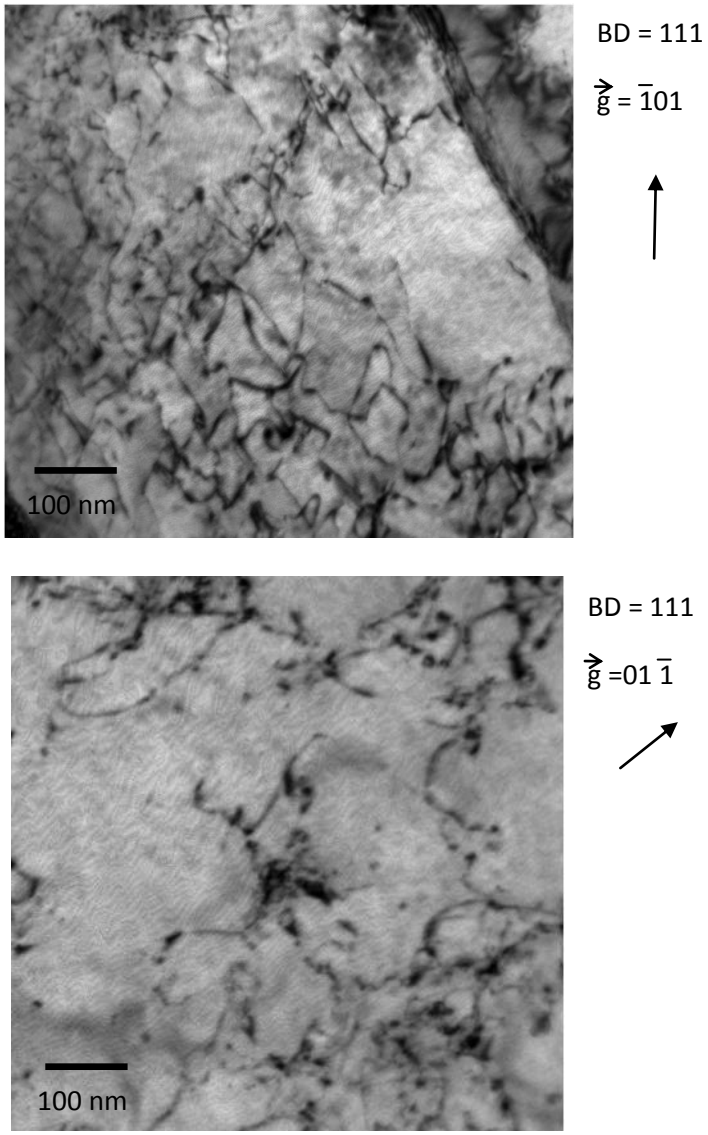

Figure 6.29 – Bright-field TEM micrographs of the X80 as-received alloy showing its typical dislocation structure.

6.2.3 Compression tests

Similarly to the X70 as-received alloy, the X80 as-received alloy was tested for compression up to 1 and 2% plastic strain in order to simulate the first step of the Bauschinger test and to offer a comparison of the effect of pre-strain on the Bauschinger parameters. Figure 6.30 shows the 2% (plastic deformation) compression curve of the X80 alloy.

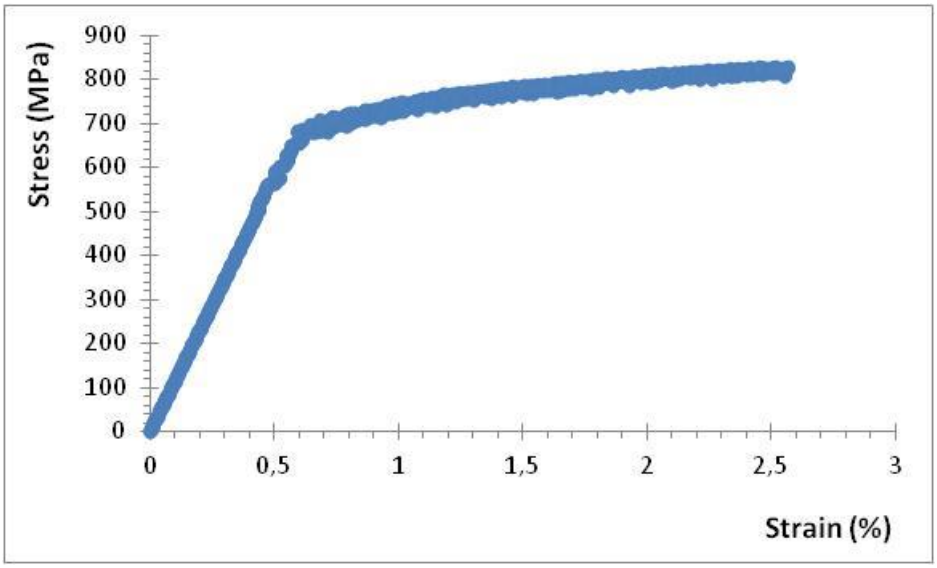

Figure 6.30 – Stress-strain curve for compression test of the X80 alloy up to 2% plastic strain.

The TEM analysis of the compressed samples showed an increase in the average dislocation density to 7.592 x10^{14} m^{-2}.

The initial dislocation clusters present in the as-received material have developed into dislocation walls and dislocation cells. Similarly to the compressed X70 samples, there

is a higher dislocation concentration within the walls and lower density within the dislocation cell and this structure is homogeneous for different types of dislocations.

The presence of the retained austenite islands in the X80 alloy has caused an increase in the stress concentration around this second phase, resulting in an increased dislocation density. Figure 6.31 shows a typical dislocation structure of the X80 alloy after 2% plastic compression.

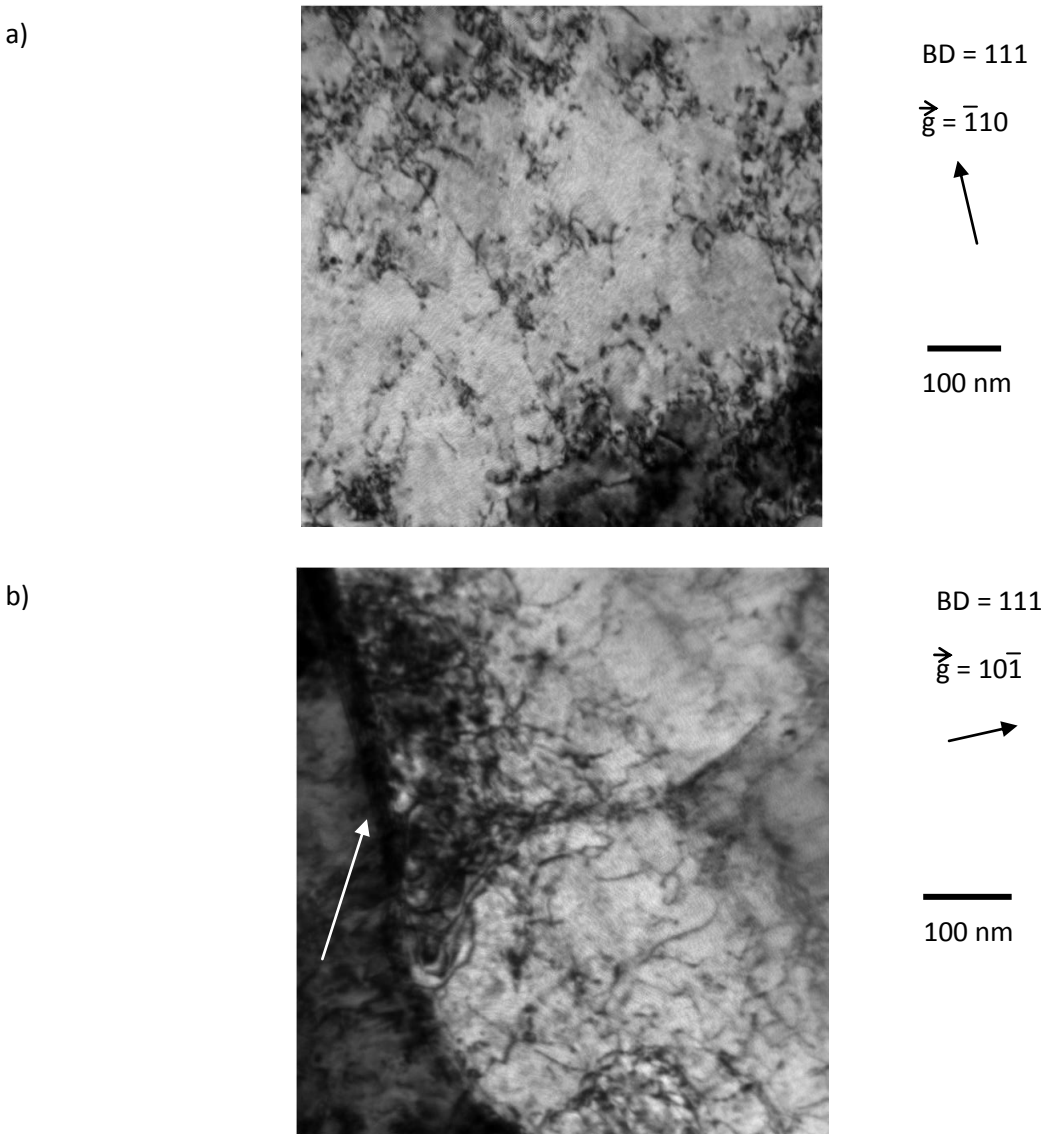

Figure 6.31 – Bright-field TEM micrographs of the X80 alloy after 2% compression showing a) the typical dislocation microstructure and b) a stress concentration area due to the presence of a retained austenite island (white arrow).

6.2.4 Macro Bauschinger tests

The stress-strain curves of the macro Bauschinger tests on the X80 alloy are shown in figure 6.32. For the 1% Bauschinger test, the value of maximum stress (σ_p) in compression was 805.5 MPa and 841.8 MPa for the 2% Bauschinger test. For 1% test the values of stress at 0.2 ($\sigma_{r0.2}$) and 0.5% ($\sigma_{r0.5}$) tension strain were 450 and 580 MPa, whereas the values of stress at 0.2 ($\sigma_{r0.2}$) and 0.5% ($\sigma_{r0.5}$) tension strain for the 2% test were 445 and 580 MPa. The Bauschinger parameters $\beta\sigma_{0.2}$ and $\beta\sigma_{0.5}$, therefore, were 0.44 and 0.28 for the 1% Bauschinger test and 0.47 and 0.31 for the 2% Bauschinger test. A summary of these results is shown in table 6.3.

a)

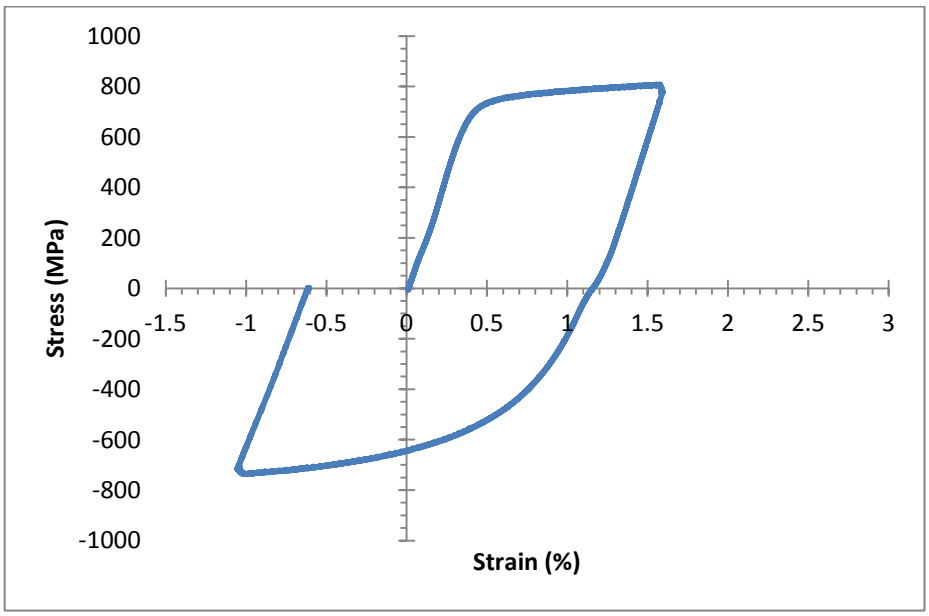

b)

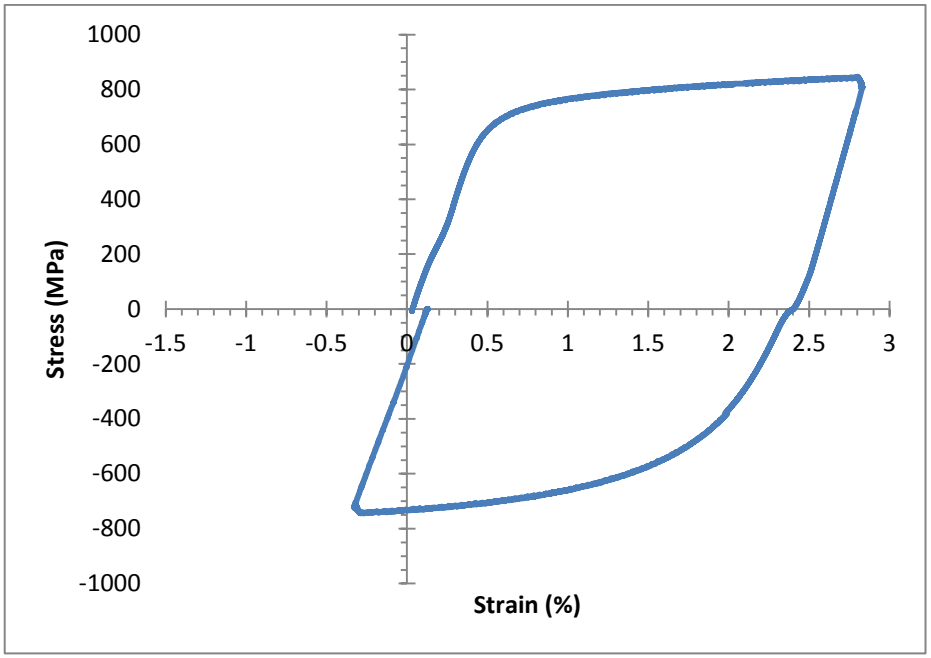

Figure 6.32 – Bauschinger test of the X80 alloy up to a) 1% and b) 2% plastic strain.

Table 6.3 – Bauschinger parameters for the X80 alloy after 1 and 2% tests.

Plastic strain	σ_p (MPa)	$\sigma_{r0.2}$ (MPa)	$\beta\sigma_{0.2}$	$\sigma_{r0.5}$ (MPa)	$\beta\sigma_{0.5}$
1%	805,5	450	**0.44**	580	**0.28**
2%	841,8	445	**0.47**	580	**0.31**

After the Bauschinger test, the dislocation analysis of the X80 alloy shows predominantly a cell structure in which most of the cells have a dislocation-free core.

The dislocation density after the Bauschinger test remained similar to that after compression at 7.269 x10^{14} m^{-2}. Figure 6.33 shows a bright-field micrograph of the X80 alloy after 2% Bauschinger test.

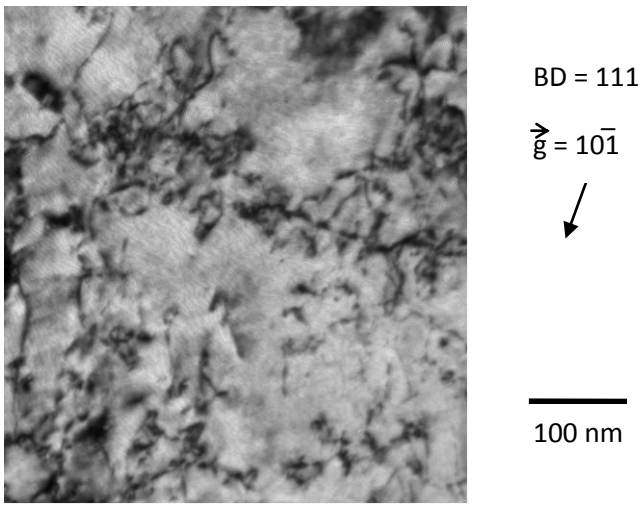

Figure 6.33 – TEM micrograph of the X80 alloy after Bauschinger test.

6.2.5 In-situ Bauschinger tests

For the Bauschinger tests on the X80 alloy, the cross-sectional areas of the samples were 56.45, 35.79 and 17.39 µm² and they were tested up to 1% pre-strain (compression) followed by 1% reverse strain (tension).

For the 56.45 µm² sample, the maximum stress value (σp) in compression was 845 MPa, the stress value at 0.2% strain in tension was 480 MPa and at 0.5% strain in tension was 600 MPa. Thus the Bauschinger parameters βσ0.2 and βσ0.5 were 0.43

and 0.28 respectively. The curve of the Bauschinger test for this sample is shown in figure 6.34.

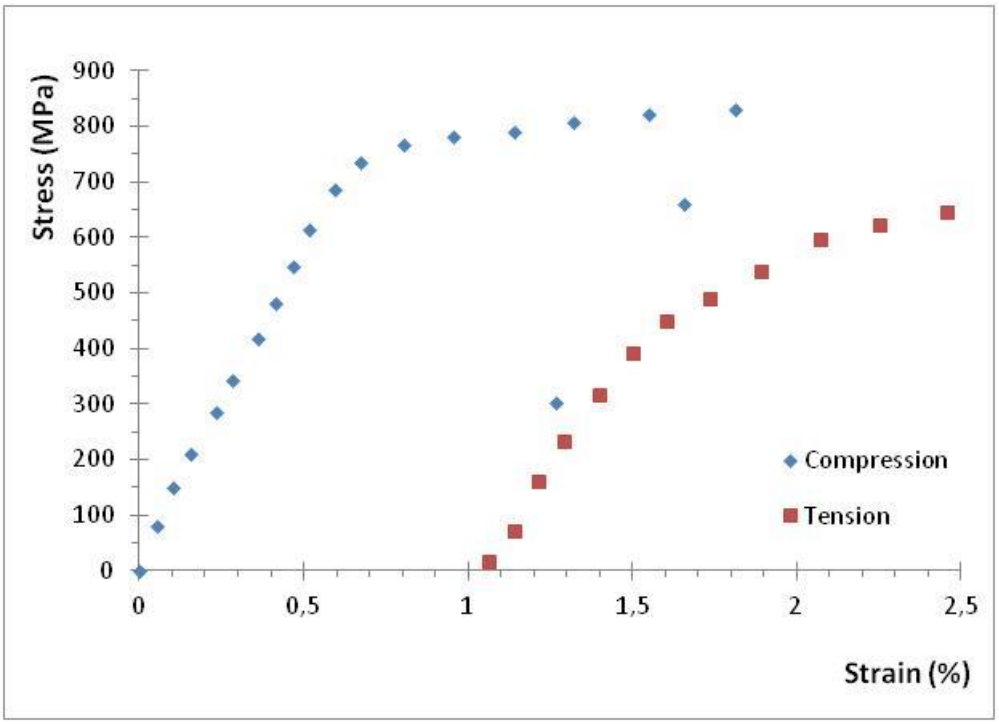

Figure 6.34 – In-situ Bauschinger test curve of the X80 alloys sample of 56.45 µm² cross-sectional area.

For the 35.79 µm² sample, the maximum stress value (σp) in compression was 843 MPa, the stress value at 0.2% strain in tension was 475 MPa and at 0.5% strain in tension was 600 MPa. Thus the Bauschinger parameters βσ0.2 and βσ0.5 were 0.44 and 0.29 respectively. The curve of the Bauschinger test for this sample is shown in figure 6.35.

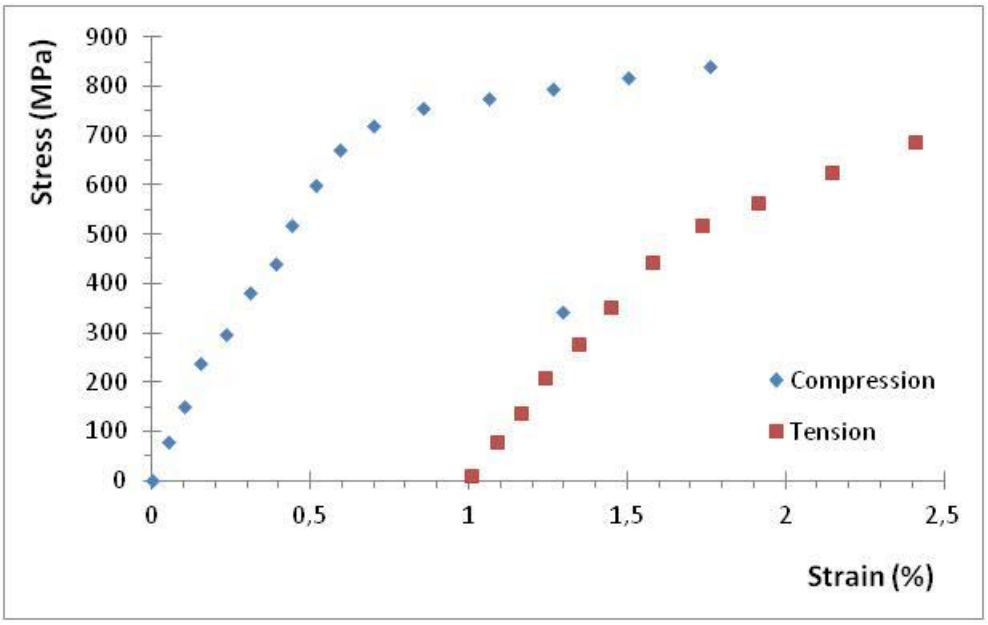

Figure 6.35 – In-situ Bauschinger test curve of the X80 alloys sample of 35.79 µm² cross-sectional area.

For the 17.39 µm² sample, the maximum stress value (σp) in compression was 810 MPa, the stress value at 0.2% strain in tension was 470 MPa and at 0.5% strain in tension was 590 MPa. Thus the Bauschinger parameters βσ0.2 and βσ0.5 were 0.42 and 0.27 respectively. The curve of the Bauschinger test for this sample is shown in figure 6.36.

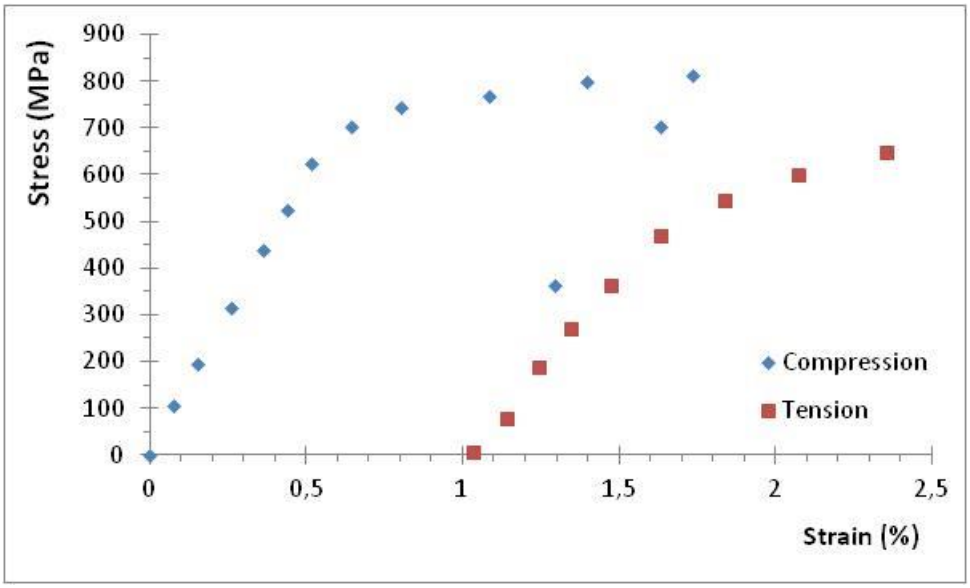

Figure 6.36 – In-situ Bauschinger test curve of the X80 alloys sample of 17.39 µm² cross-sectional area.

Results from the X80 alloy micro Bauschinger tests show that the Bauschinger parameter is similar for the different sizes used, as well as when compared to the macro Bauschinger tested samples, as with the X70 alloy, as in table 6.4 below.

Table 6.4 – micro Bauschinger parameters for the X80 alloy.

Cross-section	σ_p (MPa)	$\sigma_{r0.2}$ (MPa)	$\beta\sigma_{0.2}$	$\sigma_{r0.5}$ (MPa)	$\beta\sigma_{0.5}$
56.45 µm²	845	480	**0.43**	600	**0.28**
35.79 µm²	843	475	**0.44**	600	**0.29**
17.39 µm²	810	470	**0.42**	590	**0.27**

6.3 X100 alloy

6.3.1 Thermodynamic simulation

Similarly to the X80 alloy, Thermo-Calc simulation of the phase presence at different temperatures for the X100 alloy is shown in figure 6.37, where the BCC phases (δ and α) and the FCC phase (γ) are represented by the red and green lines, respectively. The predictions of the Ar_3 and Ar_1 temperatures for the X100 alloy are 817°C and 655°C respectively.

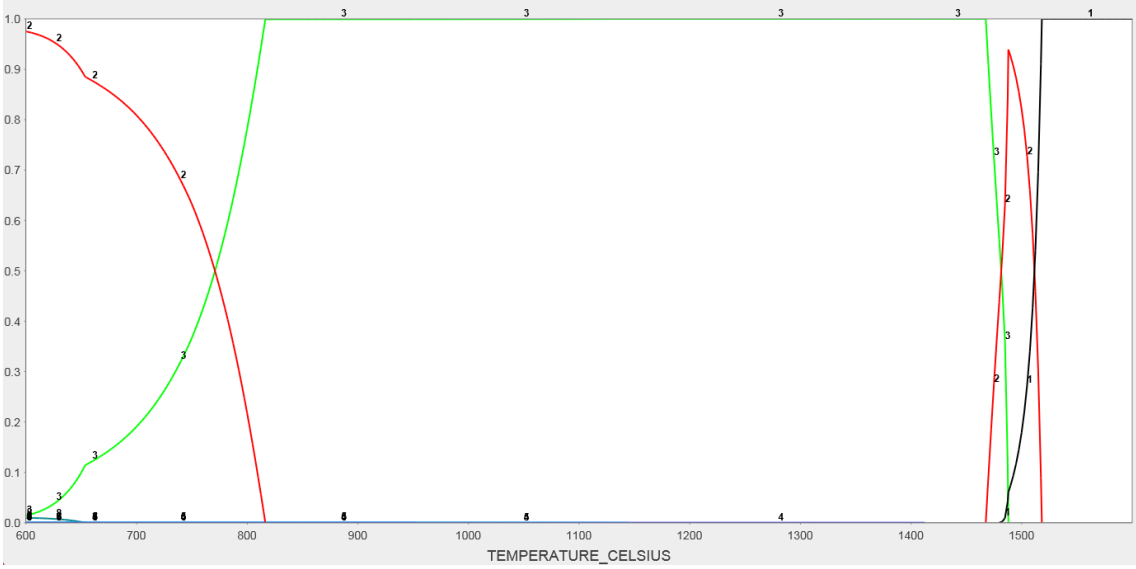

Figure 6.37 – Thermo-Calc prediction graph of phase evolution according to temperature of the X80 alloy. Red (left): α; Red (right): δ; Green: γ.

Additionally, at 600°C, Thermo-Calc has shown that the volume fraction of austenite is 1,39%, cementite is 0.81% and the combined volume fraction of precipitates is very low at 0.0006.

6.3.2 Microstructure of X100 as-received

The microstructure of the X100 as-received alloy presents the same structure as the X80 alloy, a predominantly granular bainite which consists mostly of irregular grains of ferrite with an average grain size of 2.1 µm, small retained austenite islands/laths and cementite particles on the grain boundaries. In addition, small areas of upper bainite are present, consisting of narrow elongated ferrite grains and thin laths of retained austenite around the ferrite grains. A typical SEM image of the X80 as-received microstructure is shown in figure 6.38.

The heavily textured appearance of the X80 as-received alloy is also found in the X100 as-received alloy. Therefore it is difficult to analyse quantitatively the retained austenite and cementite features using SEM. The effect is shown in figure 6.39.

The same types of precipitates for the X70 and X80 are found in the X100 as-received alloy. The (Nb,Ti) rich precipitates present an average width of 73 nm and a volume fraction of 0.0000816%, whereas the Nb rich precipitates present an average width of 32 nm and a volume fraction of 0,0000496%.

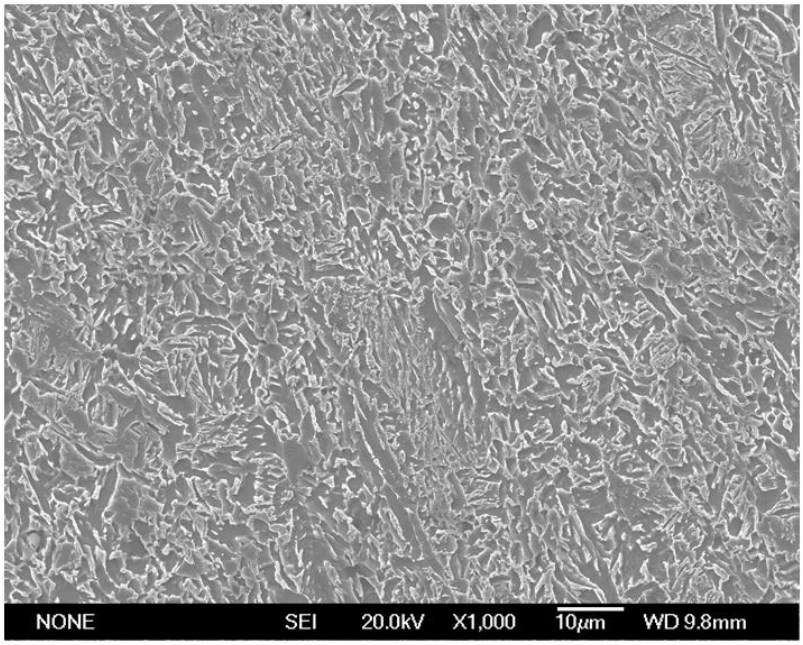

Figure 6.38 – SEM micrographs showing the general X100 microstructure.

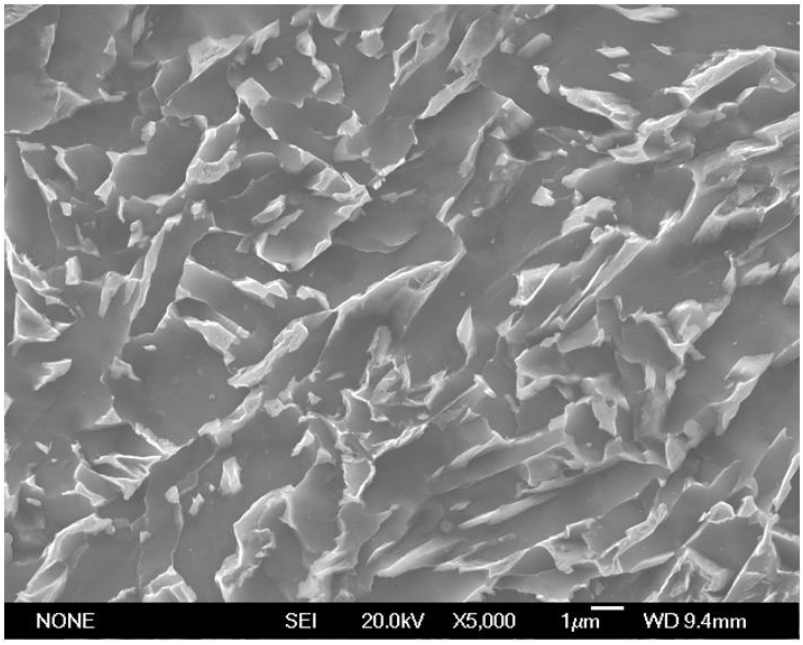

Figure 6.39 – SEM micrographs showing the heavy texture in the X100 microstructure.

A typical TEM micrograph of the X100 as-received microstructure is shown in figure 6.40. As with the X80 alloy, the TEM analysis of the Bainitic structures of the X100 alloy allows the quantification of the retained austenite and cementite particles. Almost identically to the X80, the retained austenite present in the X100 alloy forms elongated islands of around 1 µm, as well as thin laths of 10 to 20 nm, surrounded by ferrite. The total volume fraction of the retained austenite is 3.06%. Cementite particles also show a pebble like shape of 43 nm average width and 0.149% volume fraction.

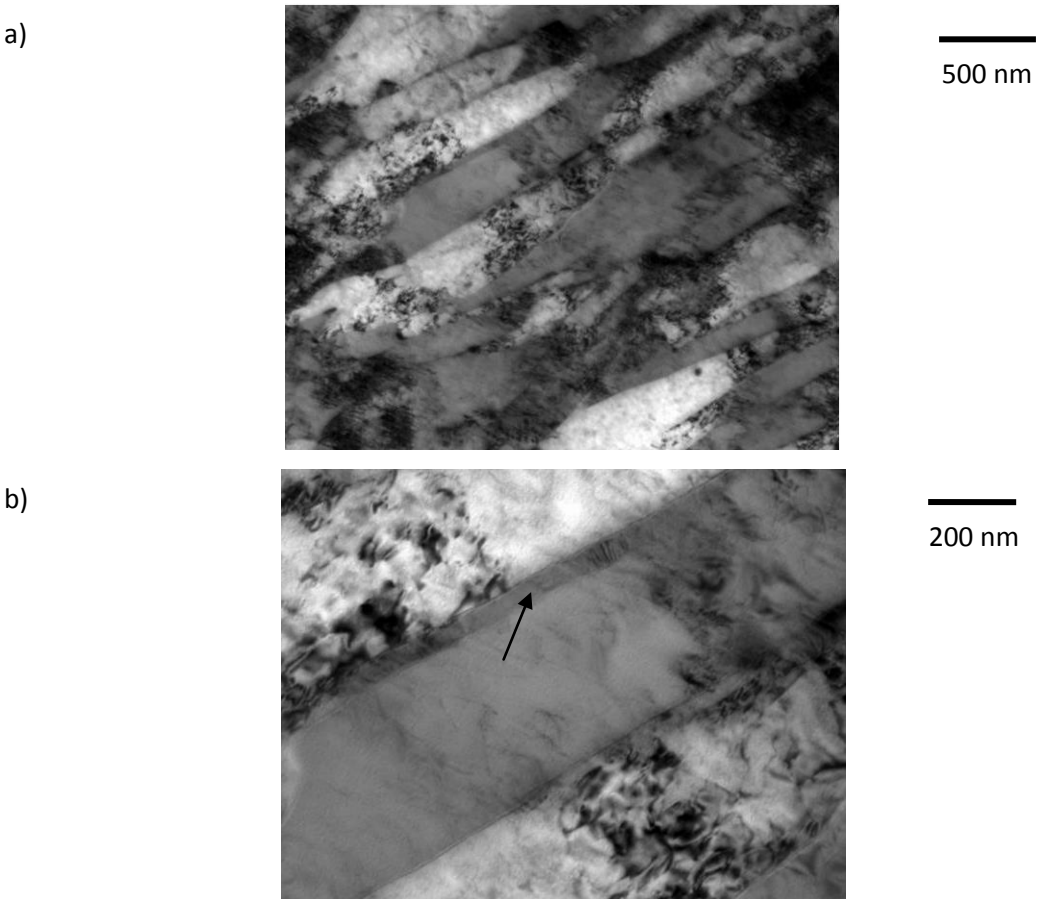

Figure 6.40 – A typical TEM micrograph of the X100 as-received alloy showing a) the fine bainitic structure and b) the thin lath of retained austenite (arrow) in between grains of ferrite.

The dislocation structure of the X100 as-received alloy is very similar to that of the X80 as-received alloy. The structure is non-uniform, predominantly arranged in clusters as in the early stages of a cellular structure. It is also homogeneous for all types of dislocations. The average dislocation density of the X100 as-received alloy is 4.629 $x10^{14}$ m^{-2}. A typical dislocation structure is shown in figure 6.41.

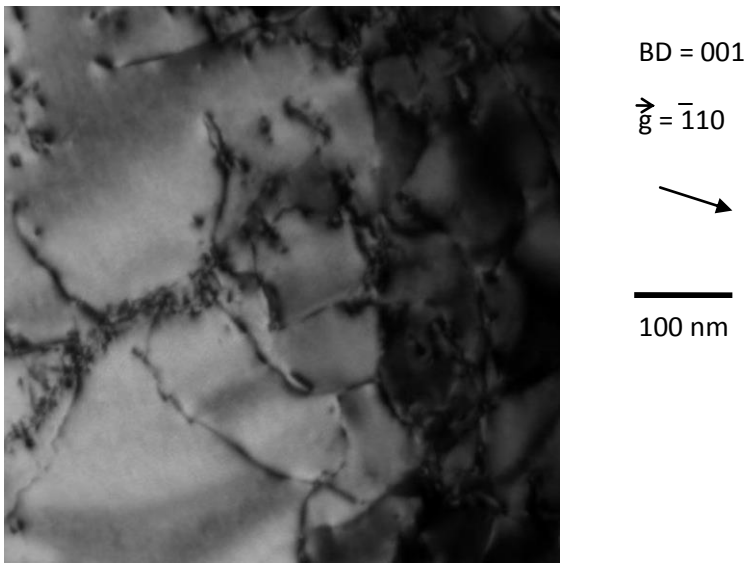

Figure 6.41 – A bright-field TEM micrographs of the X100 as-received alloy showing the typical dislocation structure arranged in clusters.

6.3.3 Compression tests

The X100 as-received alloy was tested under compression up to 1 and 2% plastic deformation in order to provide a dislocation structure similar to the ones expected during the first step of the Bauschinger effect. Figure 6.42 show a compression curve for the X100 alloy after 2% compression.

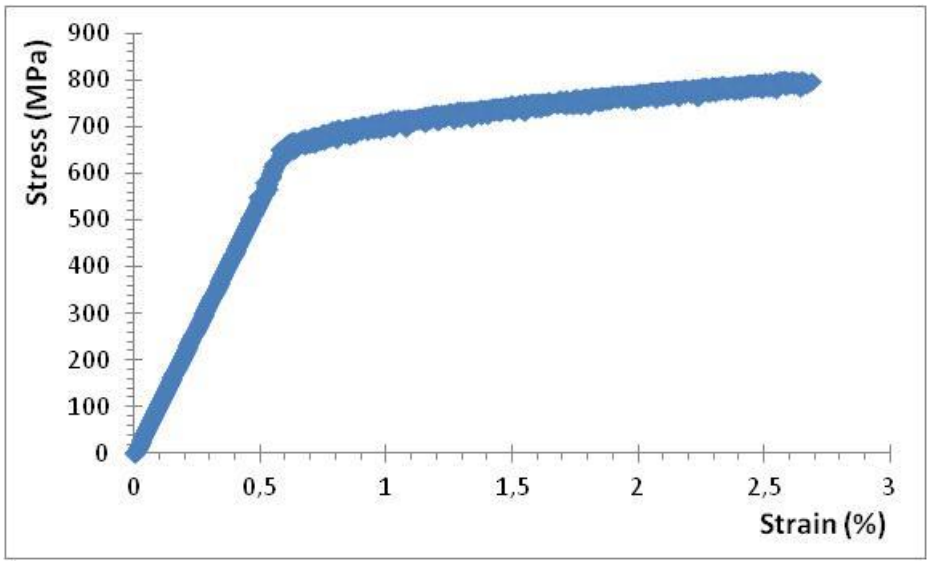

Figure 6.42 – Stress-strain curve of the compression test of the X100 alloy at 2% plastic strain.

As with the X80 alloy, the dislocation structure after compression develops from the embryonic clusters of the as-received material to the formation of dislocation walls and dislocation cells. The average dislocation density has increased from the as-received state to 7.251 $x10^{14}$ m^{-2}. This structure also remains homogeneous for different types of dislocations. A typical TEM micrograph of the dislocation structure after compression is shown in figure 6.43.

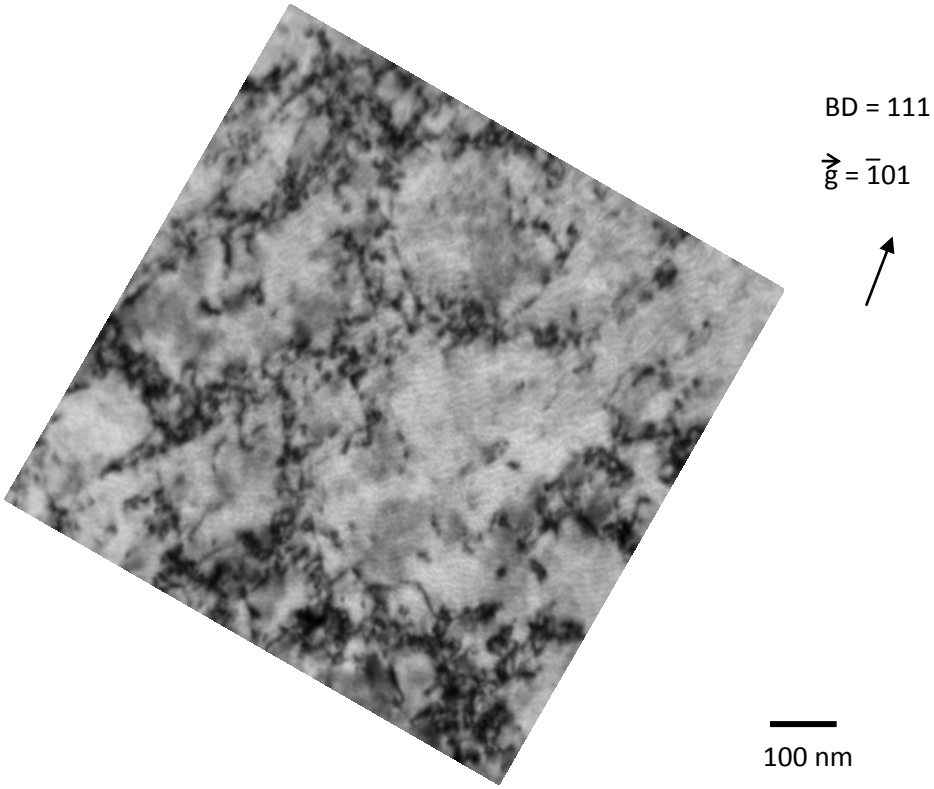

Figure 6.43 – Bright-field TEM micrograph of the X100 alloy after 2% compression.

6.3.4 Macro Bauschinger tests

The value of maximum stress (σ_p) in compression was 765 MPa for the 1% Bauschinger test, and 817 MPa for the 2% Bauschinger test. For the 1% test, the values of stress at 0.2% ($\sigma_{r0.2}$) and 0.5% ($\sigma_{r0.5}$) tension for the 1% test were 428 and 502 MPa, whereas the values of stress at 0.2 ($\sigma_{r0.2}$) and 0.5% ($\sigma_{r0.5}$) tension strain for the 2% test were 450 and 595 MPa. The Bauschinger parameters $\beta\sigma_{0.2}$ and $\beta\sigma_{0.5}$, therefore, were 0.44 and 0.27 for the 1% Bauschinger test and 0.45 and 0.28 for the 2% Bauschinger test. The

stress-strain curves of the macro Bauschinger tests carried out on the X100 alloy are shown in figure 6.44 and a summary of these results is shown in table 6.5.

a)

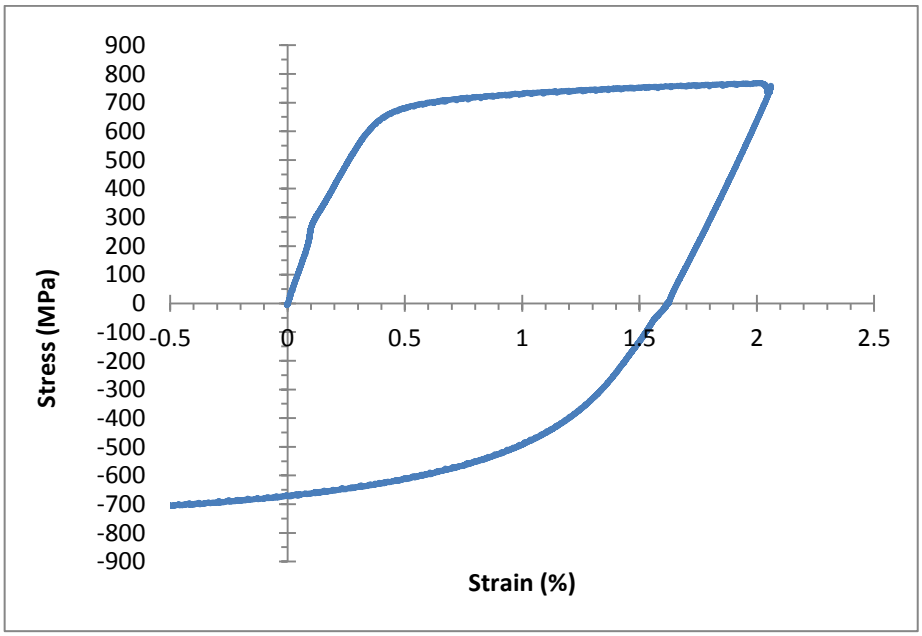

b)

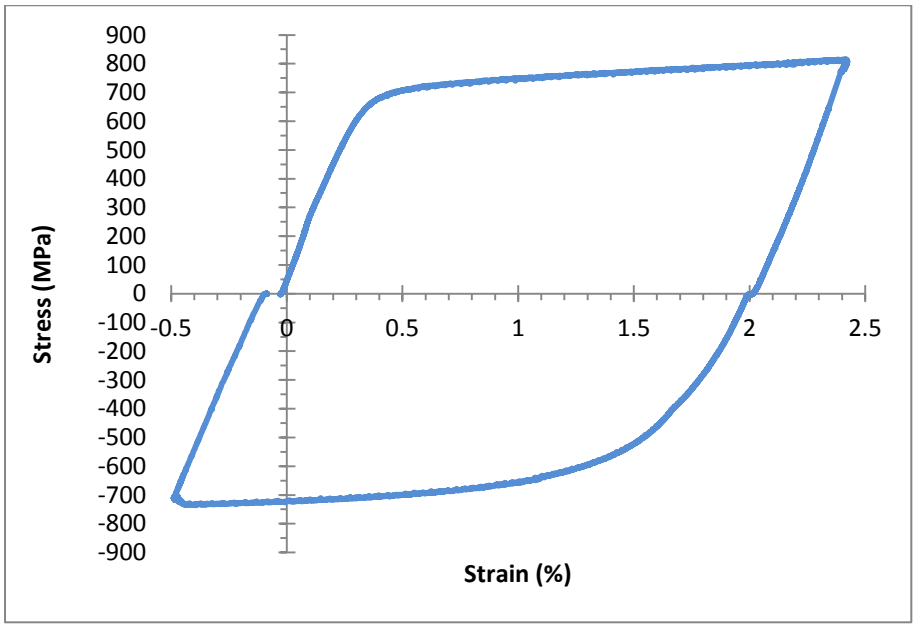

Figure 6.44 – Bauschinger test of the X100 alloy up to a) 1% and b) 2% plastic strain.

Table 6.5 – Bauschinger parameters for the X100 alloy after 1 and 2% tests.

Plastic strain	σ_p (MPa)	$\sigma_{r0.2}$ (MPa)	$\beta\sigma_{0.2}$	$\sigma_{r0.5}$ (MPa)	$\beta\sigma_{0.5}$
1%	765	428	**0.44**	555	**0.27**
2%	817	450	**0.45**	585	**0.28**

After the Bauschinger test, the dislocation structure of the X100 consists of a predominant cell structure with regions of low dislocation density near the cells cores. The dislocation density after the Bauschinger test has also remained similar to after compression at 7.094 $x10^{14}$ m^{-2}. Figure 6.45 shows a bright-field micrograph of the X80 alloy after a 2% Bauschinger test.

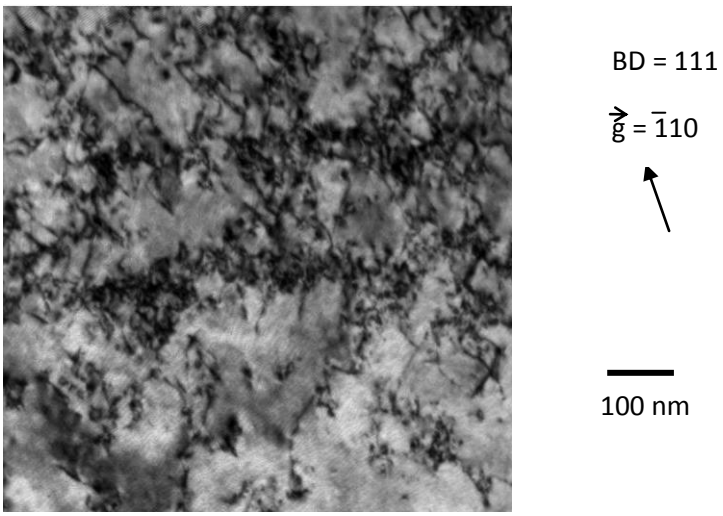

Figure 6.45 – Bright-field TEM micrograph of the X100 alloy after Bauschinger test.

6.3.5 In-situ tests

For the Bauschinger tests of the X100 alloy, the cross-section areas of the samples were 55.37, 32.55 and 17.18 µm². The Bauschinger tests were carried out up to 1% pre-strain (compression) followed by 1% reverse strain (tension).

The maximum stress value (σp) in compression for the 55.37 µm² sample was 820 MPa, the stress value at 0.2% strain in tension was 475 MPa and at 0.5% strain in tension was 600 MPa. Thus the Bauschinger parameters βσ0.2 and βσ0.5 were 0.42 and 0.27 respectively. The results of the Bauschinger test for this sample is shown in figure 6.46.

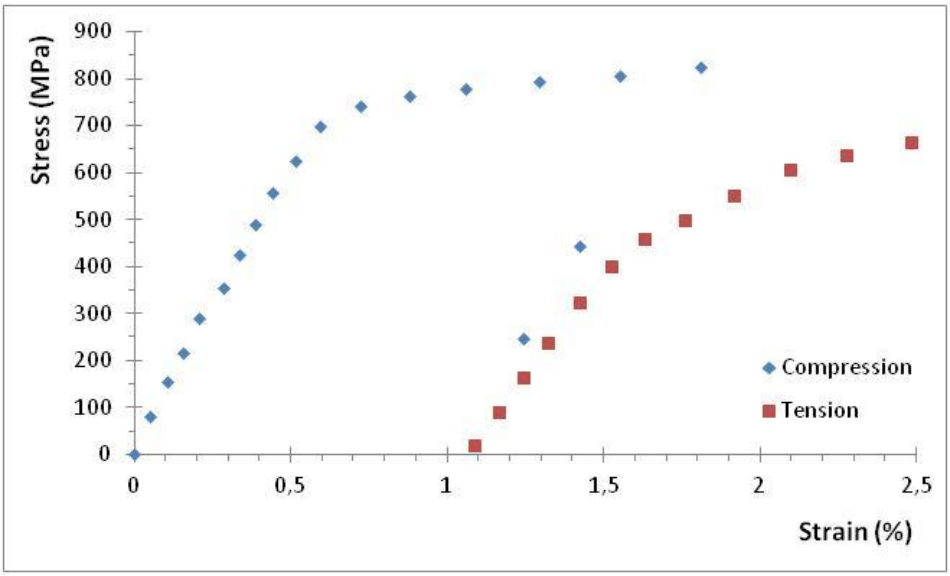

Figure 6.46 – In-situ Bauschinger test curve of the X100 alloys sample of 55.37 µm² cross-section area.

The maximum stress (σp) in compression for the 32.55 µm² sample was 830 MPa, the stress value at 0.2% strain in tension was 480 MPa and at 0.5% strain in tension was

605 MPa. Thus the Bauschinger parameters βσ0.2 and βσ0.5 were 0.42 and 0.27 respectively. The curve of the Bauschinger test for this sample is shown in figure 6.47.

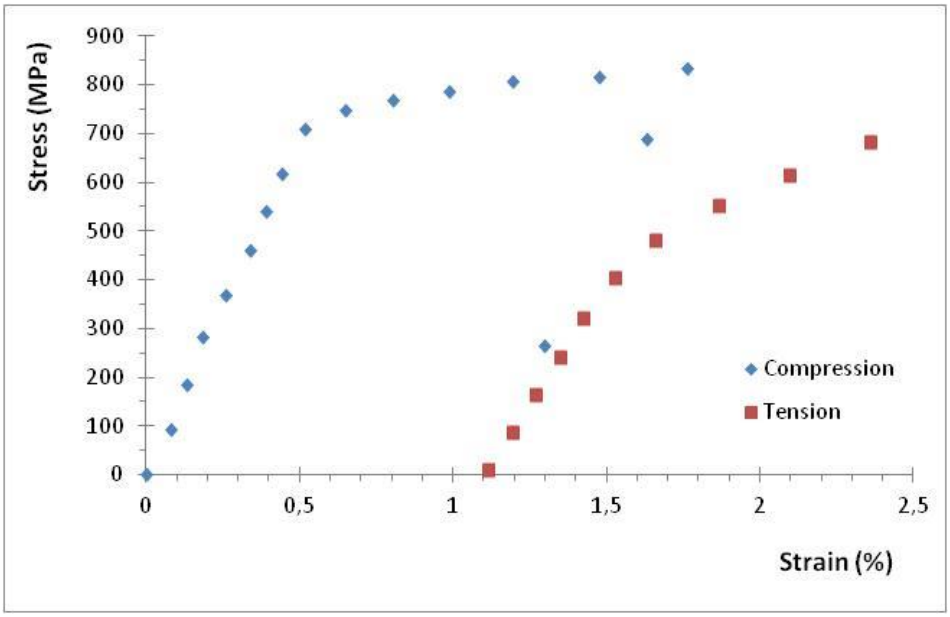

Figure 6.47 – In-situ Bauschinger test curve of the X100 alloys sample of 32.55 μm² cross-section area.

For the 17.39 μm² sample, the maximum stress value (σp) in compression was 810 MPa, the stress value at 0.2% strain in tension was 475 MPa and at 0.5% strain in tension was 605 MPa. Thus the Bauschinger parameters βσ0.2 and βσ0.5 were 0.41 and 0.25 respectively. The curve of the Bauschinger test for this sample is shown in figure 6.48.

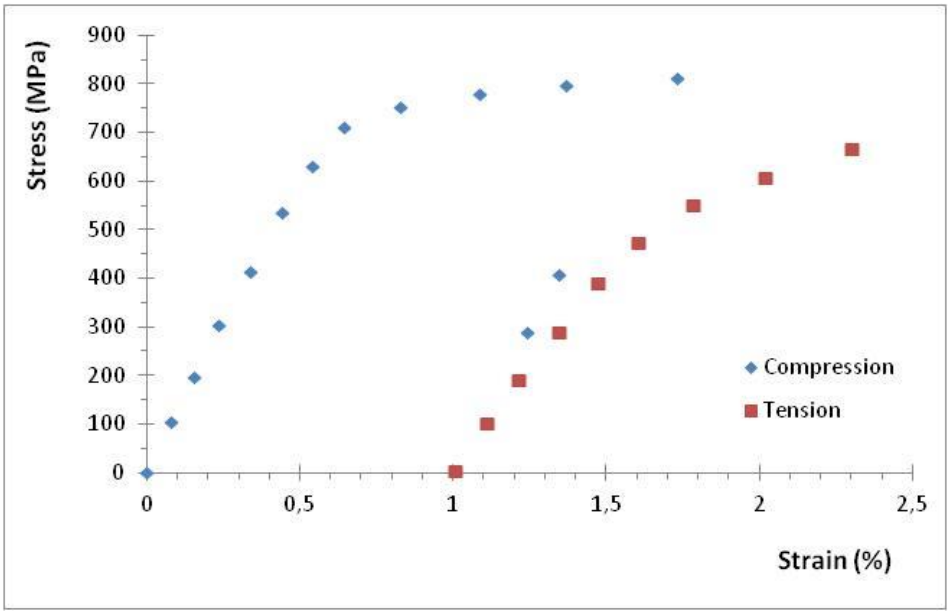

Figure 6.48 – In-situ Bauschinger test curve of the X100 alloys sample of 17.18 µm² cross-section area.

Similarly to previous results from the X70 and X80 alloys, the Bauschinger parameter is constant for the different sample sizes tested, as shown in table 6.6 below.

Table 6.6 – micro Bauschinger parameters for the X100.

Cross-section	σ_p (MPa)	$\sigma_{r0.2}$ (MPa)	$\beta\sigma_{0.2}$	$\sigma_{r0.5}$ (MPa)	$\beta\sigma_{0.5}$
55.37 µm²	820	475	**0.42**	600	**0.27**
32.55 µm²	830	480	**0.42**	605	**0.27**
17.39 µm²	810	475	**0.41**	605	**0.25**

7 DISCUSSION

7.1 Summary of results

A summary of the results is presented below in order to aid the development of the discussion.

A MEMS based device was designed for the purpose of performing micro mechanical tests and its dimensions were chosen in order to provide a wide range of samples sizes. A DRIE process was developed and the devices were manufactured from a silicon wafer. Additionally, an external actuator was designed and set up in order to provide movement to the micro mechanical test device.

A method for preparing micro samples was developed combining the preparation of TEM disc samples and milling using a focused ion beam.

Thermo-Calc predictions of Ar_3 and Ar_1 temperatures and cementite and precipitate volume fraction for the X70 alloy were 849°C, 666°C, 0.39% and 0.0010036 respectively.

For the as-received X70 alloy, the microstructure consisted mostly of polygonal grains of ferrite of an average grain size of 2.8 µm and along with a pearlitic microstructure within the grains of ferrite covering a total area fraction of 3.1%.

The precipitates found in the as-received X70 alloy were (Nb,Ti)C, squared shaped with size ranging from 50 to 170 nm, an average width of 79 nm and a volume fraction of

0.000273, and (Nb)C, of spherical morphology with size ranging from 20 to 55 nm, an average diameter of 36 nm and a volume fraction of 0.000162.

An analysis of the dislocation structure in the as-received X70 alloy showed homogeneously dispersed dislocations with little evidence of dislocation-particle interaction and an average dislocation density of 7.872×10^{-13} m^{-2}. In addition, small dislocations tangles are present.

After a compression test of 2% plastic strain, the dislocation structure developed into dislocation walls, starting to form dislocation cells and an increased dislocation density of 2.186×10^{14} m^{-2}.

The Bauschinger parameters $\beta\sigma_{0.2}$ and $\beta\sigma_{0.5}$ after a 1% Bauschinger test were 0.33 and 0.18 respectively, whereas $\beta\sigma_{0.2}$ and $\beta\sigma_{0.5}$ after a 2% Bauschinger test were 0.37 and 0.24 respectively.

The dislocation structure after 2% Bauschinger test fully developed into a dislocation cell structure where most of the cells presented a dislocation-free core. Also, the dislocation density was 2.019×10^{14} m^{-2}.

The Bauschinger tests carried out in micro-sized samples presented the following Bauschinger parameters: for the 52.57 μm^2 cross-section sample, $\beta\sigma_{0.2}$ and $\beta\sigma_{0.5}$ were 0.32 and 0.17 respectively, for the 30.86 μm^2 cross-section sample, $\beta\sigma_{0.2}$ and $\beta\sigma_{0.5}$ were 0.31 and 0.17 respectively, and for the 16.12 μm^2 cross-section sample, $\beta\sigma_{0.2}$ and $\beta\sigma_{0.5}$ were 0.32 and 0.18 respectively.

Thermo-Calc predictions of Ar_3 and Ar_1 temperatures and austenite, cementite and precipitate volume fraction for the X80 alloy were 815°C, 647°C, 2.19%, 0.65% and 0.00054185 respectively.

The microstructure of the X80 as-received alloy consisted predominantly of granular bainite and small areas of upper bainite with an average grain size of 1.9 µm. Retained austenite was intergranularly present in the form of elongated 1 µm long islands and as very thin laths of 10 to 20 nm across with a total volume fraction of 2.74%. Alongside the retained austenite, pebble shaped particles of cementite of 45 nm average width and 0.132% volume fraction were present.

Precipitation in the X80 alloys happened in the form of (Nb,Ti)C with an average width of 71 nm and 0.0000728 volume fraction and also (Nb)C with an average width of 35 nm and volume fraction of 0.0000439

Dislocations presented a non uniform structure in the X80 as-received alloy, arranged in tangles and an average dislocation density of 4.835×10^{14} m^{-2}. However, this structure was homogeneous for all types of dislocations.

After a 2% plastic strain compression test, the initial dislocation structure developed into walls and dislocation cells, with a dislocation density of 7.592×10^{14} m^{-2}.

Bauschinger tests of 1 and 2% resulted in a Bauschinger parameter $\beta\sigma_{0.2}$ of 0.44 and 0.47 respectively and a Bauschinger parameter $\beta\sigma_{0.5}$ of 0.28 and 0.31.

The dislocation microstructure fully developed into dislocation cells after the 2% Bauschinger test and a dislocation density of 7.269×10^{14} m^{-2}.

The Bauschinger test on micro-sized samples resulted in Bauschinger parameters $\beta\sigma_{0.2}$ and $\beta\sigma_{0.5}$ of 0.43 and 0.28 for the 56.45 μm² cross-section sample, $\beta\sigma_{0.2}$ and $\beta\sigma_{0.5}$ of 0.44 and 0.29 for the 35.79 μm sample and $\beta\sigma_{0.2}$ and $\beta\sigma_{0.5}$ of 0.42 and 0.27 for the 17.39 μm² sample.

Thermo-Calc predictions of Ar_3 and Ar_1 temperatures and austenite, cementite and precipitate volume fraction for the X100 alloy were 817°C, 655°C, 1.39%, 0.81% and 0.00055930 respectively.

Similarly to the X80, the microstructure of the X100 as-received alloy presented predominantly granular bainite and small areas of upper bainite with an average grain size of 2.1 μm. The volume fraction of the retained austenite was 3.06%, in the form of elongated islands as well as thin laths within grain boundaries. Cementite particles also showed a pebble like shape of 43 nm average width and 0.149% volume fraction and were also located alongside the retained austenite.

Similarly to the X80, precipitation in the X100 alloy consisted of (Nb,Ti)C with average width of 73 nm and a volume fraction of 0.0000816%, as well as (Nb)C with an average width of 32 nm and 0.0000496% volume fraction.

A non-uniform dislocation structure was present in the X100 as-received alloy, predominantly arranged in tangles and with a dislocation density of 4.629×10^{14} m^{-2}. These developed into dislocation walls and dislocation cells after a compression test of 2% plastic strain and the average dislocation density of 7.251×10^{14} m^{-2} was achieved.

In the X100 as-received alloy, the Bauschinger parameters $\beta\sigma_{0.2}$ and $\beta\sigma_{0.5}$ were 0.44 and 0.45 after a 1% Bauschinger test and 0.27 and 0.28 after a 2% Bauschinger test. The dislocation structure fully developed into dislocation cells after the 2% Bauschinger test and the dislocation density was 7.094×10^{14} m^{-2}.

Lastly, the Bauschinger tests on micro-sized samples resulted in Bauschinger parameters $\beta\sigma_{0.2}$ and $\beta\sigma_{0.5}$ of 0.42 and 0.27 for the 55.37 μm^2 sample, 0.42 and 0.27 for the 32.55 μm^2 sample and 0.41 and 0.25 for the 17.18 μm^2 sample.

Table 7.1 - Summary of the key experimental data

Specimen	X70				X80				X100			
		Micro	Micro	Micro		Micro	Micro	Micro		Micro	Micro	Micro
Grain Size	2.8 µm				1.9 µm				2.1 µm			
Predicted Second Phase	0.39 % cementite				2.19 % austenite + 0.65 % cementite				1.39 % austenite + 0.81 % cementite			
Second Phase	3.1 % pearlite				2.74 % retained austenite + 0.13% cementite				3.06 % retained austenite + 0.15 % cementite			
Predicted total precipitate vol %	0.100				0.054				0.056			
Precipitate vol % / size	(NbTi)(C,N) 0.027 / 79 nm NbC 0.016 / 36 nm				(NbTi)(C,N) 0.007 / 71 nm NbC 0.004 / 35 nm				(NbTi)(C,N) 0.008 / 73 nm NbC 0.005 / 32 nm			
Dislocation density	7.87×10^{-13} 2.19×10^{-14} after 2% strain				4.84×10^{-14} 7.59×10^{-14} after 2% strain				4.63×10^{-14} 7.25×10^{-14} after 2% strain			
Bauschinger sample cross section, µm²	15.9×10^{6}	53	31	16	15.9×10^{6}	56	36	17	15.9×10^{6}	55	33	17
Yield strength, MPa	495				699				670			
Max stress on 1% strain, MPa	520	541	560	558	806	845	843	810	765	820	830	810
Max stress on 2% strain, MPa	557				842				817			
Bauschinger Parameters on 1% pre-strain	0.33 / 0.18	0.32 / 0.17	0.31 / 0.17	0.32 / 0.18	0.44 / 0.28	0.43 / 0.28	0.44 / 0.29	0.42 / 0.27	0.44 / 0.27	0.42 / 0.27	0.42 / 0.27	0.41 / 0.25
Bauschinger Parameters on 2% pre-strain	0.37 / 0.24				0.47 / 0.31				0.45 / 0.28			

7.2 As-received microstructure

As mentioned in chapter 2, the microstructure of high strength low alloy steels can vary significantly depending on their chemical composition and the thermomechanical process applied.

When comparing the chemical composition of the three studied alloys from table 5.01, it is noticeable that the X70 has a slightly lower addition of alloying elements in general, except for niobium and titanium, whereas the X80 and X100 have very similar values for all alloying elements, with the main difference being a 13.6% increase in the amount of carbon in the X100 alloy, compared to the X80.

The 0.042 wt% of carbon in the predominantly ferritic structure of the X70 alloy is considerably lower than the 0.07 – 0.099 wt% range found in the literature [54, 55, 56, 57, 58]. Thus a lower amount of second phase and precipitate strengthening was expected. From the amount of cementite (0.39%) expected by the ThermoCalc, 2.86% of pearlite can be estimated. This value, however, may vary due to the TMCP and the addition of other alloying elements, causing a shift in the eutectoid temperature and composition, which may explain the 3.1% of pearlite measured.

In contrast, an amount of 0.65% and 0.81% of cementite was estimated by ThermoCalc from the 0.059 and 0.067 wt% of carbon in the bainitic structure of the X80 and X100 alloys respectively, whereas the measured amounts of cementite particles were 0.132% and 0.149% for these alloys. Additionally, 2.74% and 3.06% of retained austenite is present due to the high cooling rate, which reduces the amount of free carbon and, therefore, the amount of cementite and precipitates.

The volume fraction of precipitates in the alloys can be estimated by taking the density of the precipitate material and their respective wt% relative to the density of the ferrite. The atomic masses of titanium, niobium and vanadium are 47.87, 92.91 and 50.94 and their lattice parameters are 0.431, 0.446 and 0.416 nm [9] respectively. Their densities relative to the ferrite are, therefore, 1.59 (Ti), 1.14 (Nb) and 1.68 (V), which results in the estimated volume fractions shown in table 7.2.

The experimentally measured TiC and NbC combined volume fractions in the X70, X80 and X100 alloys are 0.000435, 0.0001167 and 0.0001132 respectively, whereas the estimated TiC and NbC volume fractions for each of the three alloys are 0.0009271, 0.0004956 and 0.0005117.

Table 7.2 – Estimated precipitate volume fraction according to their relative density to ferrite

Alloy	**TiC**	**NbC**	**VC**
X70	0.0002227	0.0007044	0.0000656
X80	0.0001320	0.0003636	0.0000925
X100	0.0001368	0.0003749	0.0000925

It is clear that the measured amounts of Ti and Nb carbides are lower than the estimated amount according to the chemical composition, and that the difference is more noticeable in the X80 and X100 alloys than in the X70 alloy. This may be a result of the TMCP applied to the alloys, where an accelerated cooling rate may have

lowered the precipitation rate, keeping the carbon in solid solution and favouring the formation of second phase.

In addition, vanadium precipitation was expected to occur, as predicted in table 7.2. However, precipitates of this type were not found in any of the studied alloys. As, shown in chapter 2, precipitation of vanadium carbides is the last to occur (lowest temperature when compared to Ti and Nb precipitates) and, therefore, the amount of carbon present to form this type of precipitate may have been too low or the cooling rate did not allow time for precipitation. Also, small quantities of vanadium may have precipitated within the Ti and Nb precipitates formed previously.

It is noticeable that the measured volume fraction of the retained austenite agrees reasonably well with the values predicted by the Thermo-Calc for the X70 and X80 alloys. No retained austenite is predicted by Thermo-calc for the X70 and this has been confirmed experimentally, whereas 2.19% is predicted for the X80 and this is close to the 2.74% measured experimentally. However, there is a noticeable difference between the predicted and experimental results on the retained austenite for the X100 alloy, where 1.39% is predicted noticeably lower than the 3.06% measured experimentally. The phase balance can be significantly affected by the thermomechanical processing of the alloys, which haven't been accounted for in the current Thermo-Calc predictions as the software uses the phase transformations in equilibrium, which might explain the differences observed.

The volume fraction of cementite predicted by Thermo-Calc has shown a good agreement with the measured value for the X70 alloy. In this alloy, cementite is

present in the pearlitic structure with a measured value of 0.372%, while the predicted amount of cementite is 0.39%. However, large discrepancy exists in terms of the X80 and X100 alloys, where the predicted cementite volume fraction of 0.65% (X80) and 0.81% (X100) are around five times higher than the 0.132% (X80) and 0.149% (X100) measured experimentally. This is however not a surprise, considering that the measured retained austenite values were also higher than the predicted ones as previously discussed, and therefore less carbon is expected to be available for the cementite formation.

Lastly, the volume fractions of precipitates predicted by Thermo-Calc do not agree well with the measured values for the three different alloys. The difference between measured and predicted was much larger for the X80 and X100 alloys and less so for the X70 alloy.

While the measured volume fraction of the combined precipitates for the X70 alloy is 0.0004350, the predicted value by Thermo-Calc is 2.3 times higher as 0.0010036. The difference increases to 4.6 times between the measured 0.0001167 and predicted 0.0005418 volume fraction of all precipitates for the X80 alloy and 4.3 times between the measured 0.0001312 and predicted 0.0005593 volume fraction of all precipitates for the X100 alloy.

These differences are inconsistent to the ones found on previous work on similar alloys [33, 46] where up to a 27% difference between measured and ThermoCalc predicted could be noted.

The differences between the predictions from Thermo-Calc and the experimentally measured results shown above for precipitate volume fraction may be caused by several factors: 1. significant numbers of small precipitates that have not been quantified; 2. non-equilibrium levels of precipitates being formed (i.e. the TMCP processing results in a higher level of carbon remaining in solution (e.g. retained austenite), thus decreasing the amount of cementite and precipitates present in the three alloys. This effect is more readily observed in the X80 and X100 alloys, where higher retained austenite levels are seen, than in the X70 alloy. Additionally, the difficulty in imaging these precipitates experimentally due to their fine scale may also result in the underestimation of the volume fractions experimentally.

The microstructure analysis of the X70 alloy showed a very fine ferritic structure with an average grain size of 2.8 μm. A grain size in this range is not uncommon in HSLA steels and is achieved by conditioning of the austenite structure at high temperatures due to the rolling and to the alloying additions, resulting in an increase in recrystallisation stop temperature, along with a decrease in finish rolling temperature. Consequently, initial austenitic grain size, nucleation of recrystallised grains and grain growth rates are largely decreased, thus leading to a smaller ferrite grain size. Additionally, due to the small amount of recrystallisation at lower temperatures, decreasing the finish rolling temperature may result in stored deformation, thus higher dislocation complexity and density.

7.3 Mechanical properties

The yield strength requirements for the X70, X80 and X100 alloys are 70, 80 and 100 ksi, which convert to 483, 552 and 689 MPa respectively. The experimental yield strength taken from the stress-strain curve from the mechanical tests for the X70 alloy was 495 MPa, whereas for the X80 alloy the yield strength was 699 MPa and for the X100 the yield strength was 670 MPa.

Considering the similarities between the X80 and X100 microstructures, it is unsurprising that their yield strength is similar. However, it is clear that the received X80 yield strength is much higher than the minimum 552 MPa required for its strength level and is, in fact, at an X100 strength level. On the other hand, the received X100 presented a slightly lower yield strength than the minimum required for its strength level.

The results from the microstructure experiments previously discussed can be used in estimating their contribution to the yield strength via solid solution strengthening, work hardening strengthening, precipitation strengthening and grain size strengthening, as mentioned in section 2.4. Using these methods, the predicted values for the yield strength of the received materials were 572, 707 and 687 MPa for the X70, X80 and X100 alloys respectively. The stacked columns in figure 7.01 show the contribution of each strengthening mechanisms to the yield strength of each studied alloy.

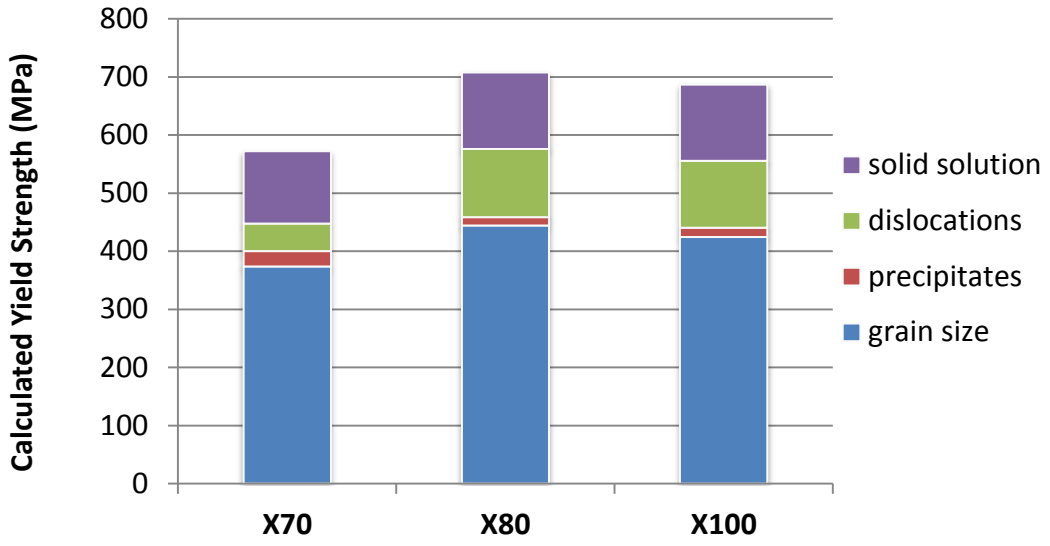

Figure 7.01 – Yield strength calculated for the strengthening mechanisms using the microstructure measurements.

The theoretical yield strength shows that the highest contribution to the yield strength comes from grain size strengthening for all three alloys, corresponding to around 60% of the yield strength of the material. However, this theoretical value does not take into account the presence of low angle grain boundaries, which is known to decrease the strengthening effect of grain boundaries and may explain the higher predicted yield strength for the X70 alloy. The same is not observed in the X80 and X100 alloys due to the bainitic structure with its thin layers of retained austenite and pebble like cementite in between the grains of ferrite.

The slightly higher amounts of Ti and Nb in the X70 alloy result in increased precipitation strengthening when compared to the X80 and X100 alloys, whereas the higher dislocation density found in the X80 and X100 alloys results in the work hardening strengthening being increased when compared to the X70 alloy.

Lastly, the strengthening contribution from the solid solution is similar between all three alloys despite the higher carbon content in the X80 and X100 alloys. Carbon is the element of most contribution to solid solution strengthening, but the amount of carbon in solution remains the same at room temperature.

7.4 Bauschinger tests

Taken from the stress-strain curves obtained from the Bauschinger tests, the Bauschinger parameters in terms of stress at 0.2% and 0.5% pre-strain were used in order to compare directly the three alloys for 1 and 2% plastic deformation.

As expected, all specimens analysed showed early plastic deformation upon reverse straining. The magnitude of the work softening, however, presented small variations depending on the strength grade and the amount of forward plastic deformation, as demonstrated in figure 7.02.

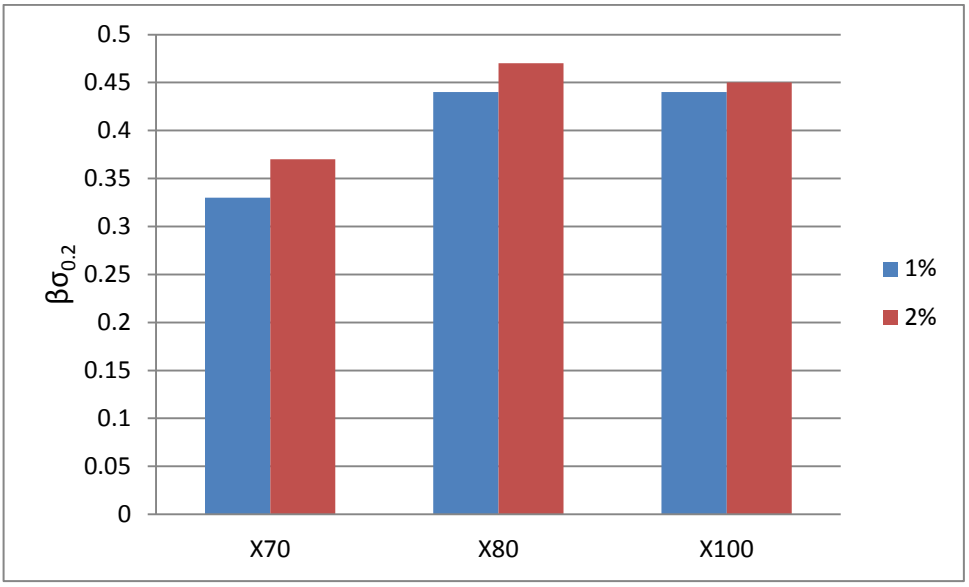

Figure7.02 – Bauschinger stress parameter βσ0.2 for the X70, X80 and X100 alloys at 1 and 2% strain.

The increase of the Bauschinger stress parameter from the X70 to the X80 alloy reflects the enhanced mechanical properties of the X80, when compared to the X70, due to the smaller grain size and higher dislocation density, which results in a higher number of interactions between the dislocations and the barriers to their movement, generating a larger back-stress. The same analysis can be applied to the increase the Bauschinger stress parameter from 1 and 2% strain in the forward direction for all three alloys.

Albeit with a lower absolute value, the same pattern was found for the work softening recovery of the three alloys, as evidenced by the Bauschinger stress parameter βσ0.5 shown in figure 7.03. After 0.5% reverse plastic deformation, the Bauschinger effect has remained higher according to the higher back-stress present.

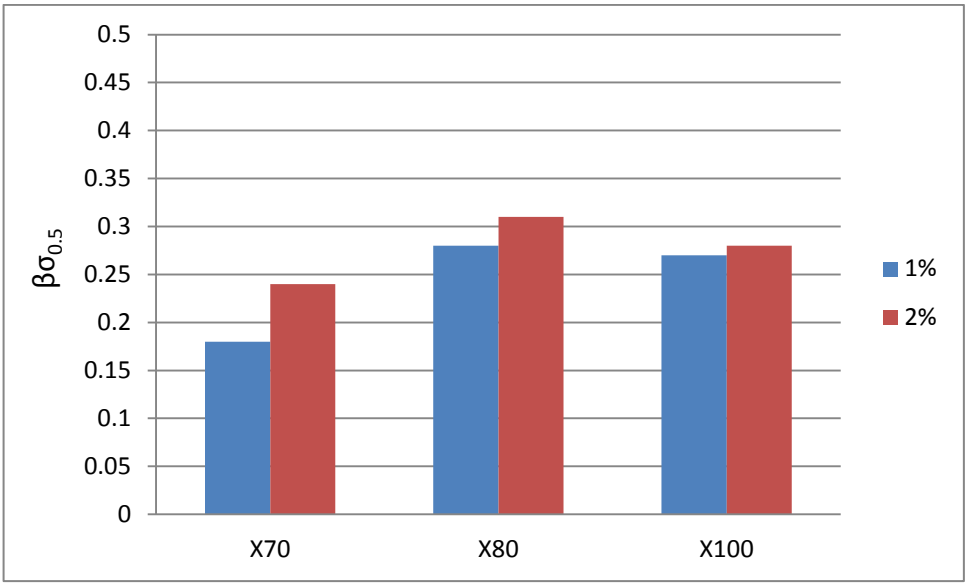

Figure7.03 – Bauschinger stress parameter βσ0.5 for the X70, X80 and X100 alloys at 1 and 2% strain.

When the 1 and 2% reverse stress-strain curves are plotted together for each of the three different alloys, it is clear that their behaviour is very similar, despite the increase in pre-strain. The Bauschinger parameter increases because the stress value σp increases due to the work hardening, but upon reverse strain, the plastic deformation follows a very similar path, independently of the amount of strain in the forward direction, as shown in figure 7.04.

a)

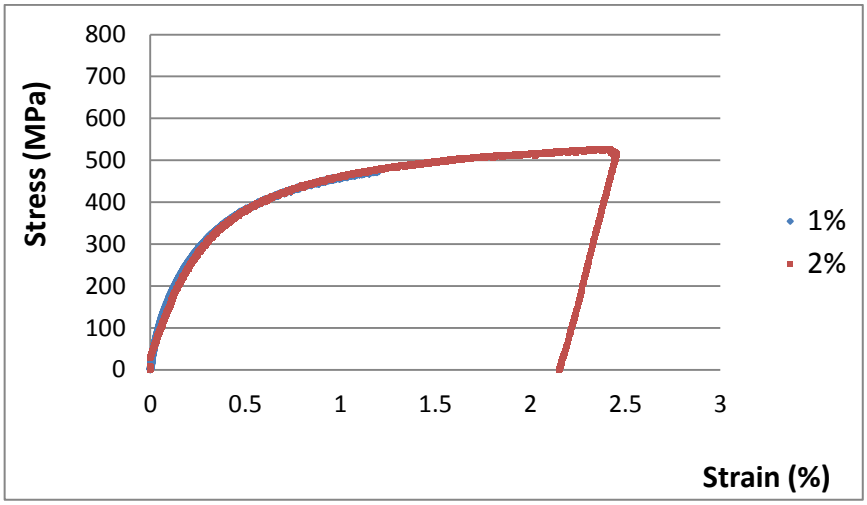

b)

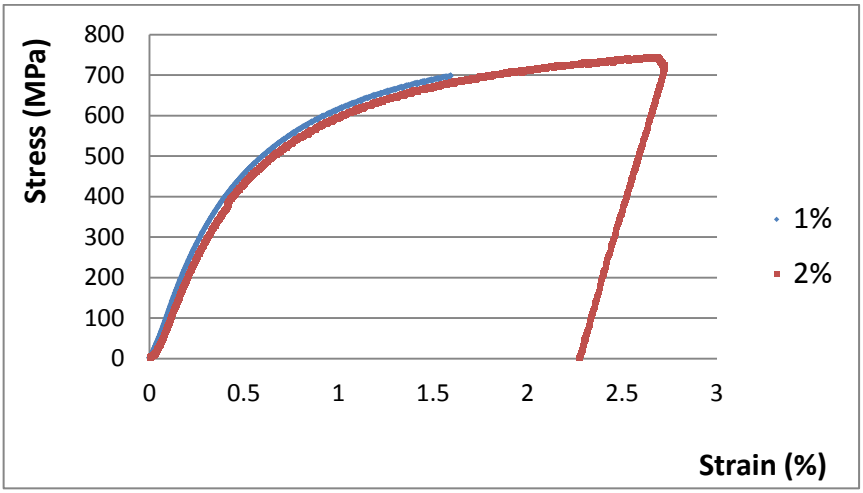

c)

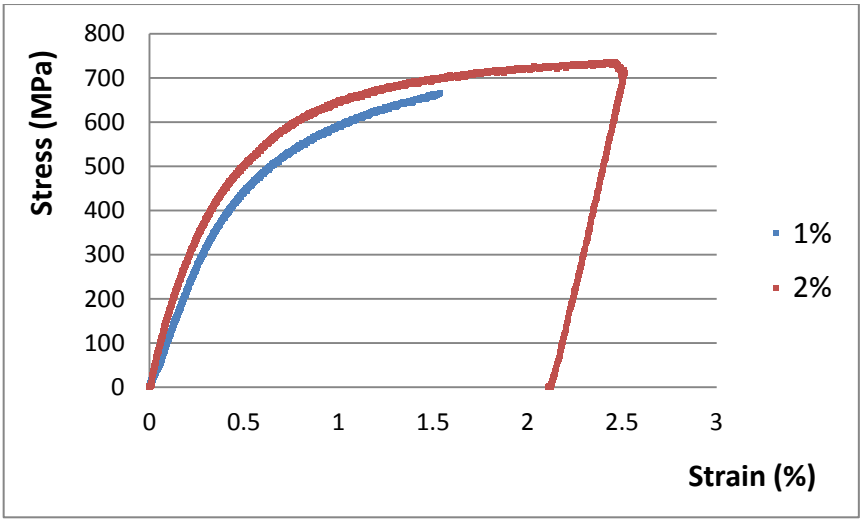

Figure 7.04 – Reverse stress-strain curves for the a) X70, b) X80 and c) X100 alloys.

This behaviour is important to notice because it indicates the balance of work hardening to work softening due to the Bauschinger effect. With an increase in pre-strain, there is an increase in dislocation density, which increases work hardening of the material in forward deformation prior to unloading. However, higher dislocation density generates more back-stress, increasing the work softening due to the Bauschinger effect. Such behaviour has also been observed in other studies [46, 59], as shown in figure 7.05.

a)

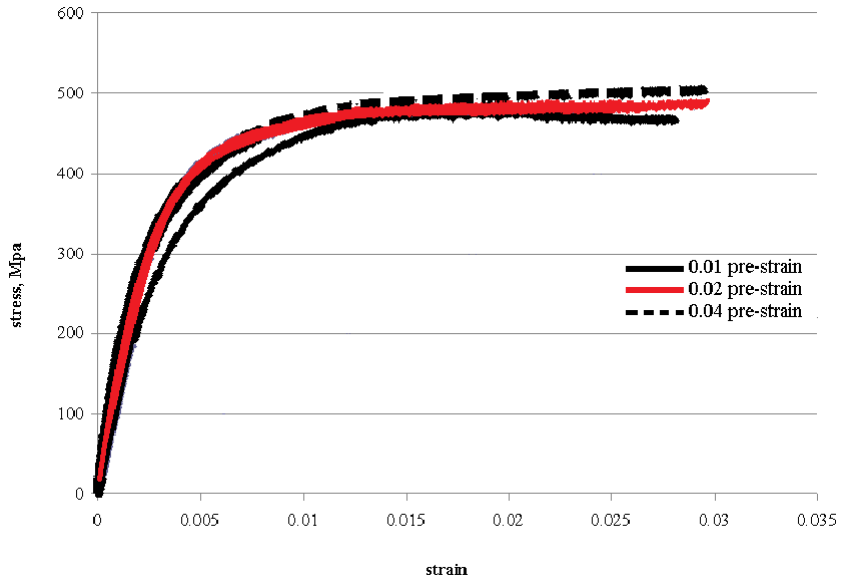

b)

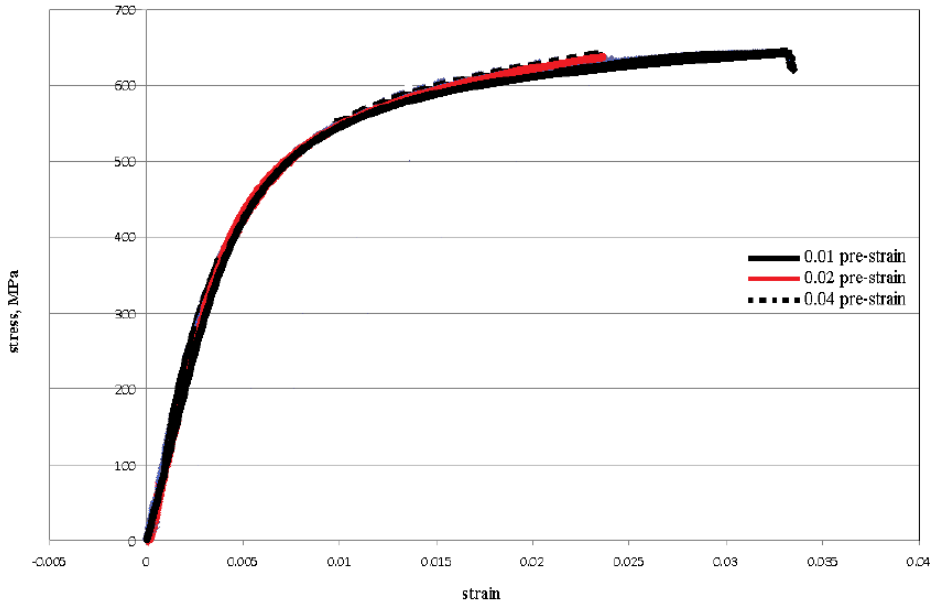

Figure 7.05 – Reverse stress strain curves for a) X65 and b) X80. [46]

Unfortunately, however, there is very little data available in order to create a comparison of microstructure and reverse stress strain curve between studies because the vast majority of Bauschinger effect studies present results for Bauschinger parameters, and do not include the reverse stress strain curves.

In spite of these findings, no differentiation between dislocation–grain boundary interaction and dislocation–dislocation interaction as the cause of the Bauschinger effect can be inferred. On the other hand, due to the very small precipitation strengthening calculated, little to no back-stress is expected from precipitate – dislocation interaction.

These results, however, agree with what is found in the literature, where it is found that generally increasing the effect of strengthening mechanisms of an alloy will result in an increase in its Bauschinger effect. Previous work where similar steel grades and straining have been used [33, 46] show comparable Bauschinger effect values and behaviour to the present study.

Decreasing the size of the specimens for the Bauschinger tests was pursued in an attempt to further understand the phenomenon and isolate the causes of the Bauschinger effect. Figure 7.06 shows the Bauschinger parameters βσ0.2 and βσ0.5 for the three different sample sizes of each alloy after a Bauschinger test of up to 1% plastic strain.

Following the same pattern as the macro Bauschinger tests, the Bauschinger parameter βσ0.2 increases from 0.31 to 0.43 from the X70 to the X80 alloy and remains around the same for the X100 alloy. Similarly, the same increment is observed for the Bauschinger parameter βσ0.5.

These Bauschinger parameter values remain unchanged when the sample cross-section is decreased from around 50 μm^2 to 15 μm^2 for all three alloys. Due to the

expected contribution of the grain boundaries to the Bauschinger effect, a decrease in the Bauschinger effect had been expected as the sample size decreased.

a)

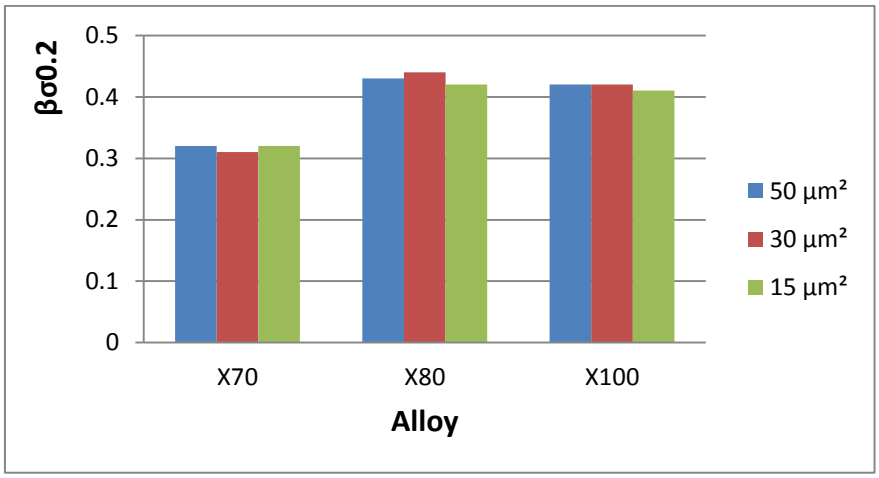

b)

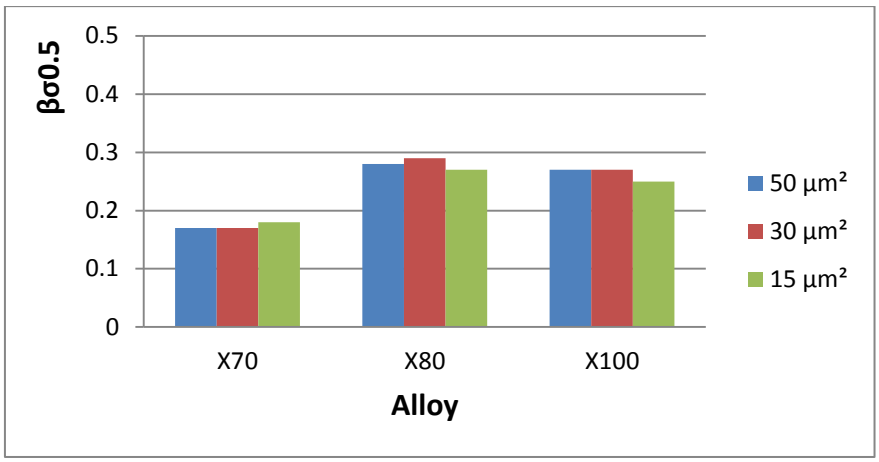

Figure 7.06 – The Bauschinger parameters a) βσ0.2 and b) βσ0.5 for small scale samples.

This behaviour may be explained by the dislocation structure present in the studied alloys. Due to the cell structure, the dislocations are trapped in the dislocation walls during the forward strain. Upon reverse strain, the last dislocations to move during the forward strain are released from the dislocation walls and require a lower stress level to do so due to the back-stress acting after release of the forward strain. The back-stress generated during the forward plastic deformation is then released progressively as the reverse strain takes place.

In order to estimate the grain boundary area contained in the small scale samples, it is assumed all grains are spherical. The number of grains contained in the gauge section of the testing sample can be estimated by dividing the total volume of the gauge section by the volume of the average grain (sphere). The grain boundary area of an average sized grain times the total number of grains contained in the gauge section gives the total grain boundary area in the gauge section. This grain boundary area derived is further divided by a factor of two to reflect the fact that a grain boundary is shared by two neighbouring grains. The grain boundary area and its ratio with the surface area are summarised in Table 7.3.

Table 7.3 – Grain boundary (GB) area (μm²) and the ratio of GB area versus the free surface area for the three alloys studied at different sample sizes.

	Sample cross section area (μm²)	50	30	15
X70	Grain boundary area (μm²)	353.36	251.43	107.50
	Ratio between GB area over Surface area	0.511	0.444	0.314
X80	Grain boundary area (μm²)	519.47	353.47	151.58
	Ratio between GB area over Surface area	0.735	0.651	0.450
X100	Grain boundary area (μm²)	471.43	335.81	140.57
	Ratio between GB area over Surface area	0.678	0.589	0.416

The calculated grain boundary to free surface area ratio shown above shows that the amount of free surface increases significantly when decreasing the sample cross section area, however, this has not translated into a change in the Bauschinger effect.

Therefore, the expected decrease in the Bauschinger effect as seen in researches on thin films has not been achieved.

These results, combined to the uniformity in the stress strain curves shown in figure 6.20 from different micro straining tests indicate that the microstructure under assessment has remained consistent throughout the micro tests for each alloy. This could indicate that the sample size has not decreased enough to cause a change in the Bauschinger effect.

Additionally, it is possible that at this scale, quantification of the Bauschinger effect of a complex microstructure could lead to misinterpretation of the results, as there could be other parameters causing an influence on what is being measured.

The contribution of grain boundaries to the plasticity and therefore the Bauschinger effect is complex and it could only be possible to study via a systematic and careful design of the experiments with well-controlled grain boundary characters and the testing conditions. This is obviously out of the scope of the current work but would be very useful for future study on this subject. Crystal plasticity modelling would also be extremely useful to complement the experimental work.

Lastly, from the micro Bauschinger test results, it is noticeable that the micro mechanical test device has performed successfully. As shown in Section 4.3, this technique has been successfully used previously, but never using samples prepared from a bulk material. This imposes difficult challenges, especially with respect to alignment of the sample to the straining device. However, the experiments performed in this project have shown that it is a feasible technique.

Further decrease of the dimensions of the microelectromechanical system in order to make it possible to test even smaller samples than the ones achieved in this project, could lead to finding results similar to the work done on thin films and possibly the point of transition where the free surface area mentioned above starts to impact the Bauschinger effect.

8 CONCLUSION AND FUTURE WORK

8.1 Conclusions

The project presented here has focused on studying the microstructure of three HSLA pipeline alloys X70, X80 and X100, as well as understanding the causes of their Bauschinger effect by performing Bauschinger tests in macro and micro sized samples. The following conclusions can be drawn from the study:

The microstructure of the X70 alloy is different from the X80 and X100. While the X80 and X100 alloys have very similar microstructures with the stronger bainitic structure containing martensite/austenite islands, thin laths of retained austenite and cementite constituents, the X70 alloy presents a predominantly ferritic structure with a small amount of pearlite within the ferritic grains.

All three alloys present a small amount of precipitates in the form of (TiNb) and Nb carbides, whilst the X70 contains slightly higher volume fraction of these precipitates compared to the X80 and X100, due to the higher amount of Ti and Nb present in the alloy. Additionally, despite the presence of V addition to the alloys, no evidence of V-containing precipitation has been found in all three alloys.

Analysis of the dislocation structure of the as-received materials has shown an expected medium to high dislocation density values for the X70 alloy with homogeneously distributed dislocations. Similarly, the X80 and X100 alloys have

slightly higher initial dislocation densities than that of the X70, as expected, due to the differences in the thermomechanically controlled processing.

The estimated strength based on the microstructural observations has corresponded well to the yield strength measured in the mechanical tests. The refinement of the microstructure is believed to be the most important fact on the yield strength of the three alloys.

Tests on macroscopic samples have shown that the Bauschinger stress parameter increases with the refinement of the microstructure and with the increasing dislocation density. Also, the Bauschinger stress parameter increases with the forward strain during the tests. Dislocation analysis after the Bauschinger tests has shown an increase in the dislocation density. The formation of dislocation walls and subsequent cell structure after forward-reverse deformation has been observed.

A micro Bauschinger test device along with a process for manufacturing micro specimens have been designed and successfully employed in the current study. The Bauschinger stress parameter derived from the stress-strain behaviour occurred during the tests on microscopic samples has similar values compared with that on macroscopic samples.

From the work carried out it is not possible to state that the grain boundaries are the dominant factor accounting for the Bauschinger effect observed in the macroscopic samples, in spite of the fact that the refined structure provides most of the strengthening.

Rather it is understood that further decreasing the scale of the micro Bauschinger tests is necessary in order to assess the roles of grain boundaries and dislocation interaction between the mobile dislocations and other barriers such as the dislocation walls and/or cell boundaries formed during forward straining which may contribute significantly to the Bauschinger effect observed.

8.2 Proposed future work

Based on the current study, the following future work plan may further the understanding on the Bauschinger effect in HSLA steels.

- Improvements to the micro Bauschinger test device may be achieved using a more complex structure, e.g. by incorporating an automated stress-strain data acquisition;
- An investigation of the Bauschinger effect on even smaller samples, decreasing the sample size down to the grain size and dislocation cell structure size, eventually achieving transparency to the TEM (i.e. around 150 nm);
- An investigation of the effect of decreasing the total plastic deformation of the Bauschinger tests on the early yielding of the materials;
- An investigation of heat treatments in order to modify the microstructure of the material in a controlled fashion so that individual microstructural features (grain size, dislocation cell, dislocation density, etc.) can be altered so that their contribution to the Bauschinger effect can be distinguished.

LIST OF REFERENCES

1. Das AK. The present and the future of line pipe steels for petroleum industry. Materials and Manufacturing Processes 2010; 25: 14-19.

2. Das AK. Steels for petroleum industries. Intl. Seminar on Energy Related Materials 2007, India.

3. Nara Y. In Proc. Steels for Line Pipe and Pipeline Fittings (London, 1981). The Metals Society/The Welding Institute 1981: 201.

4. Lauprecht W, Imgrund H, Coldren P. High-strength structural steels with a structure of low-carbon bainite subjected to thermomechanical treatment. Metal Science and Heat Treatment 1975; 17(12): 1005-1011.

5. Wang W, Shan Y, Yang K. Study of high strength pipeline steels with different microstructures. Materials Science and Engineering: A 2009; 502(1-2): 38-44.

6. Hemmingsen T, Hoydan H, Sanni P, Aagotnes NO. The influence of Electrolyte Reduction Potential on weld corrosion. Electrochim. Acta 2002; 47(27): 3949.

7. Zhang GA, Cheng YF. Micro-electrochemical characterization of corrosion of welded X70 pipeline steel in near-neutral pH solution. Corros. Sci. 2009; 51: 1714.

8. Rashid MS. High-strength, low-alloy steels. Science 1980; 208(4446): 862-869.

9. Gladman T. The physical metallurgy of microalloyed steels. Cambridge: Cambridge University Press; 1997.

10. Saikaly W, Bano X, Issartel C, Rigaut G, Charrin L, Charai A. The effects of thermomechanical processing on the precipitation in an industrial dual-phase steel microalloyed titanium. Metallurgical and Materials Transactions A, Physical Metallurgy and Materials 2001; 32(8): 1939-1947.

11. Ghosh A, Chatterjee S. Characterization of precipitates in an ultra low carbon Cu bearing high strength steel: A TEM study. Material Characterization 2005; 55(4-5): 298-306.

12. Zhu ZX, Kuzmikova L, Marimuthu M, Li HJ, Barbaro F. Role of Ti and N in line pipe steel welds. Science and Technology of Welding and Joining 2013; 18(1): 1-10.

13. Linaza MA, Romero JL, Rodriguez-Ibabe JM, Urcola JJ. Influence of the microstructure on the fracture toughness and fracture mechanisms of forging steels microalloyed with titanium with ferrite-perlite structures. Scripta Metallurgica et Materialia 1993; 29(4): 451-456.

14. Bhatnagar S, Guha B, Sinha R. Vanadium high-strength low-alloy steels for low-temperature use. Journal of Materials Science 1979; 14(7): 1631-1640.

15. Baker TN. Processes, microstructures and properties of vanadium microalloyed steels. Materials Science and Technology 2009; 25(9): 1083-1107.

16. Chen MY, Goune M, Verdier M, Brechet Y, Yang JR. Interphase precipitation in vanadium-alloyed steels: Strengthening contribution and morphological variability with austenite to ferrite transformation. Acta Materialia 2014; 64: 78-92.

17. Nohrer M, Zamberger S, Primig S, Leitner H. Atom probe study of vanadium interphase precipitates and randomly distributed vanadium precipitates in ferrite. Micron 2013; 54-55: 57-64.

18. Davenport AT, Berry FG, Honeycombe RWK. Interphase precipitation in iron alloys. Metal Science 1968; 2(1): 104-106.

19. Davenport AT, Honeycombe RWK. Precipitation of carbides at γ-α boundaries in alloy steels. Proceedings of the Royal Society of London. Series A, Mathematical and Physical Sciences 1971; 322(1549): 191-205.

20. Okamoto R, Borgenstam A, Agren J. Interphase precipitation in niobium-microalloyed steels. Acta Materialia 2010; 58(14): 4783-4790.

21. Sakuma T, Honeycombe RWK. Microstructures of isothermally transformed Fe-Nb-C alloys. Metal Science 1984; 18(9): 449-454.

22. Yen HW, Chen PY, Huang CY, Yang JR. Interphase precipitation of nanometer-sized carbides in a titanium-molybdenum-bearing low-carbon steel. Acta Materialia 2011; 59: 6264-6274.

23. Freeman S, Honeycombe RWK. Strengthening of titanium steels by carbide precipitation. Metal Science 1977; 11(2): 59-64.

24. Vervynckt S, Verbeken K, Thibaux P, Houbaert Y. Recrystalization-precipitation interaction during austenite hot deformation of a Nb microalloyed steel. Materials Science and Engineering: A 2011; 528(16-17): 5519-5528.

25. Basu R, Jain L, Maji B, Krishnan M. Dynamic recrystalization in a Ni-Ti-Fe shape memory alloy: Effects on austenite-martensite phase transformation. Journal of Alloys and Compounds 2015; 639: 94-101.

26. Michael JR, Speer JG, Hansen SS. Austenite recrystalization in Nb/V microalloyed steels. Metallurgical Transactions: A 1987; 18(3): 481-483.

27. Streisselberger A, Bauer J, Fluss P, Hillenbrand HG, Cordon P. High strength steel plates for line pipes in grades up to X100. EUROPIPE, GmbH, www.europipe.de, 2008.

28. Bauer J, Fluss P, Amoris E, Schwinn V. Microstructure and properties of thermomechanical controlled processing steels for linepipe applications. Ironmaking and Steelmaking 2005; 32(4): 325-330.

29. Bakkaloglu A. Effect of processing parameters on microstructure and properties of an Nb microalloyed steel. Material Letters 2002; 56: 200-209.

30. Prasad SN, Sarma DS. Influence of thermomechanical treatment on microstructure and mechanical properties of Nb bearing weather resistant steel. Materials Science and Engineering A 2005; 408: 53-63.

31. Smallman RE. Modern physical metallurgy and materials engineering. 6th ed. Oxford: Butterworth-Heinemann; 1999.

32. Smallman RE, Ngan AHW. Physical Metallurgy and Advanced Materials. 7th ed. Oxford: Butterworth-Heinemann; 2007.

33. Kostryzhev AG. Bauschinger effect in Nb and V microalloyed line pipe steels. Thesis for the degree of Doctor of Philosophy, School of Metallurgy and Materials, University of Birmingham, UK; 2009.

34. Bhadeshia HKDH, Honeycombe RWK. Steels: Microstructure and Properties. 3rd ed. Oxford: Butterworth-Heinemann; 2006.

35. Hume-Rothery W, Smallman RE, Haworth CW. Structure of Metals and Alloys. 5th ed. London: Institute of Metals; 1969.

36. Ramesh KT. Nanomaterials: Mechanics and Mechanisms. Baltimore: The Johns Hopkins University; 2009.

37. Irvine KJ. The development of high-strength steels. Journal of Iron and Steel Institute 1962; 200: 820-836.

38. Burns KW, Pickering FB. Deformation and fracture of ferrite-pearlite structures. Journal Of Iron and Steel Institute 1964; 202: 899-906.

39. Kyriakides S, Corona E. Mechanics of Offshore Pipelines, Vol. 1 Buckling and Collapse. Oxford: Elsevier; 2007.

40. Queyreau S, Devincre B. Bauschinger effect in precipitation-strengthened materials: A dislocation dynamics investigation. Philosophical Magazine Letters 2009; 89(7): 419-430.

41. Harrison TC, Weiner RT, Fearnehough GD. Influence of the Bauschinger effect. Journal of Iron and Steel Institute 1972; 334-336.

42. Balint DS, Deshpande VS, Needleman A, Van der Giessen E. Discrete dislocation plasticity analysis of the grain size dependence of the flow strength of polycrystals. International Journal of Plasticity 2008; 24: 2149-2172.

43. Calcagnotto M, Ponge D, Raabe D. Effect of grain refinement to 1 micron strength and toughness of dual-phase steels. Materials Science and Engineering A 2010; 527: 7832-7840.

44. Kumakura S. The Bauschinger effect in carbon steels. Bulleting of JSME 1968; 11(45): 426-434.

45. Danilov S, Metallovedenie. Effect of grain size on the Bauschinger effect, Termicheskaya Obrabotka Metallov 1964; 9: 38-41.

46. Tovee, JP. Microstructural influence of the effects of forward and reverse mechanical deformation in HSLA X65 and X80 linepipe steels. Thesis for the

degree of Doctor of Philosophy, School of Metallurgy and Materials, University of Birmingham, UK; 2014.

47. Xiang Y, Vlassak JJ. Bauschinger effect in thin metal fims. Scripta Materialia 2005; 53: 177-182.

48. Rajagopalan J, Han JH, Saif MTA. Bauschinger effect in unpassivated freestanding nanoscale metal films. Scripta Materialia 2008; 59: 734-737.

49. Xiang Y, Vlassak JJ. Bauschinger and size effects in thin-film plasticity. Acta Materialia 2006; 54: 5449-5460;

50. Rajagopalan J, Rentenberger C, Karnthaler HP, Dehm G, Saif MTA. In situ TEM study of microplasticity and Bauschinger effect in nanocrystalline metals. Acta Materialia 2010; 58: 4772-4782.

51. Muoth M, Gramm F, Asaka K, Durrer L, Helbling T, Roman C, et al. Chirality assignment to carbon nanotubes integrated in MEMS by tilted-view transmission electron microscopy. Sensors and Actuators: B 2011; 154(2): 155-159.

52. Haque MA, Saif MTA. Applications of MEMS force sensor for in situ mechanical characterization of nano-scale thin films in SEM and TEM. Sensors and Actuators: A 2002; 97: 239-245.

53. Haque MA, Saif MTA. In-situ tensile testing of nano-scale specimens in SEM and TEM. Experimental Mechanics 2002; 43(1): 123-128.

54. Sami Z, Tahar S, Mohamed H. Microstructure and charpy impact properties of ferrite-martensite dual phase API X70 linepipe steel. Materials Science and Engineering: A 2014; 598: 338-342.

55. Nastich S, Soya S, Molostov M, Vasiliev I, Dyakonova N. Effect of temperature for the start of finish rolling on coiled steel X70 microstructure and cold resistance. Metallurgist 2012; 56(7): 519-525.

56. Nastich S. Effect of bainite component morphology on the microstructure of X70 low-alloyed steel on thick plate cold resistance. Metallurgist 2012; 56(3): 196-204.

57. Shahrani AA, Yazdipour N, Dehghan-Manshadi A, Gazder AA, Cayron C, Pereloma EV. The effect of processing parameters on the dynamic recrystallisation behaviour of API-X70 pipeline steel. Materials Science and Engineering: A; 570: 70-81.

58. Masoumi M, Herculano LFG, Abreu HFG. Study of texture and microstructure evaluation of steel API 5L X70 under various thermomechanical cycles. Materials Science and Engineering: A 2015; 639: 550-558.

59. Williams D. Interaction between the Bauschinger effect and strain aging. Metallurgical Transactions: A 1980; 11(9): 1629-1631.